Absorption enhancement in thin-film silicon solar cells

THÈSE N^{O} 5973 (2013)

PRÉSENTÉE LE 19 DÉCEMBRE 2013

À LA FACULTÉ DES SCIENCES ET TECHNIQUES DE L'INGÉNIEUR

LABORATOIRE D'OPTIQUE APPLIQUÉE

PROGRAMME DOCTORAL EN PHOTONIQUE

ÉCOLE POLYTECHNIQUE FÉDÉRALE DE LAUSANNE

POUR L'OBTENTION DU GRADE DE DOCTEUR ÈS SCIENCES

PAR

Ali NAQAVI

acceptée sur proposition du jury:

Prof. O. Martin, président du jury
Prof. H. P. Herzig, Dr F.-J. Haug, directeurs de thèse
Prof. O. Isabella, rapporteur
Dr R. H. Morf, rapporteur
Prof. C. Moser, rapporteur

ÉCOLE POLYTECHNIQUE
FÉDÉRALE DE LAUSANNE

Suisse
2013

Abstract

Thin-film silicon technology is a major candidate to comply with the ever-increasing global energy demand. The small thickness of silicon allows high industrial throughput and low material usage and subsequently opens new avenues to mass-production of low-cost solar cells. This small thickness, together with the indirect bandgap of silicon and thus its relatively weak absorption of long-wavelength light, requires methods to improve absorption. This is often called light trapping.

Light absorption can be enhanced in a thin film solar cell by introducing light scattering functionalities, for example textured interfaces. Of common interest is to know: 1) how far the photocurrent and efficiency of a cell can be improved by applying these geometrical changes, 2) which geometries can satisfy the criterion of high photocurrent generation, and 3) how much the incident angle affects the two previous points. This thesis addresses the mentioned questions. Specifically, amorphous silicon (a-Si) cells are the main subject of focus in the thesis, however, the results and conclusions are applicable to other types of solar cells, and similar structures such as light-emitting diodes.

The first part of the thesis is devoted to the electromagnetic theory for thin film multilayers and the numerical methods which were used for optical simulations during the PhD work. These methods are described and compared, and some common sources of numerical error in them are identified.

To address the first and the third questions, the limits of light absorption enhancement, photocurrent generation and efficiency in thin-film solar cells are studied. As a result, we obtain the limits of absorption enhancement in thin films with periodic texture, over a wide angular and wavelength range. More specifically, first we extend the statistical temporal coupled-mode theory to the case of thin films with wavelength-scale grating couplers. Then, we use this theory to study the effect of the incident angle and the grating period on the absorption enhancement in an idealized thin film with a thickness of 200 nm and refractive index n=4. We show that absorption in a thin-film solar cell depends strongly on the grating period and angle of incidence; therefore, consideration of oblique incident of light in these cells is a necessity. We provide guidelines for the design of thin-film solar cells with periodic texture. Afterwards, we obtain the limit of absorption enhancement for different structures including a full thin-film a-Si solar cell stack for different grating geometries. We show that for thin-films, hexagonal gratings enhance absorption more significantly compared to square gratings. We identify parasitic absorption as a major bottleneck for photocurrent generation.

To deal with realistic cases, we investigate the guided modes of thin-film a-Si solar cells by

rigorous simulations (the second and the third question). First, we extract the guided modes of the cells and study them in an equivalent planar model. We show that a plasmonic mode exists for very thin buffer layers. Then, we focus on the effect of texture geometry over a broad angular range by comparing the short-circuit current density (J_{sc}) of the cells for different grating patterns. We find that based on the cell configuration, the optimal texture may be symmetric or asymmetric. We show that TM polarized light produces higher photocurrent at large incident angles regardless of the texture geometry.
In the final part of the thesis, we study two novel configurations for thin-film solar cells. First a plasmonic a-Si cell is considered which does not include a buffer layer. We demonstrate that the J_{sc} of the plasmonic cell is sensitive to the thickness of the n-doped silicon layer and we find that for an n-Si thickness of less than 10 nm, the plasmonic cell outperforms a conventional a-Si cell. Then we simulate an a-Si cell with a periodic array of ZnO nanowires inside the active layer. Our simulations indicate that assuming a periodicity of around 500 nm, the J_{sc} is highest for a nanowire diameter of about 300 nm.

Key words: Solar energy, photovoltaics, thin film, silicon, light trapping, absorption, scattering, diffraction grating, guided mode, plasmonics, nanoparticle, numerical electromagnetics, rigorous optical simulation, coupled-mode theory

Résumé

Les couches minces à base de silicium représentent une technologie photovoltaïque à fort potentiel. La faible épaisseur de silicium permet un flux de production important et une faible consommation de matière, ce qui permet une production de masse de cellules solaires à faible coût. Aux vues des épaisseurs utilisées dans cette technologie et du fait que le silicium possède une bande interdite indirecte (par conséquent une faible absorption pour les grandes longueurs d'onde), il est primordial de développer de nouvelles méthodes afin d'améliorer l'absorption lumineuse, ceci étant désigné comme le piégeage de la lumière.

L'absorption de la lumière dans une cellule solaire à couches minces peut être amplifiée en introduisant des procédés de diffusion de la lumière, par exemple la texturation de l'interface. Afin de quantifier l'efficacité de la cellule solaire, il est important d'étudier 1) le photo-courant maximum atteignable en appliquant ces modifications géométriques, 2) les géométries permettant d'atteindre les photo-courants les plus élevés et 3) l'influence de l'angle d'incidence de la lumière sur les deux points précédents. C'est à ces trois questions que nous tentons de répondre dans cette thèse. En particulier, nous nous intéressons aux cellules solaires à base de silicium amorphe (a-Si). Néanmoins, les résultats et les conclusions obtenus sont applicables à d'autres types de cellules solaires ainsi qu'à des structures similaires, telles que les diodes électroluminescentes.

La première partie de cette thèse est consacrée à l'introduction de la théorie électromagnétique des couches minces. Une description ainsi qu'une comparaison des différentes méthodes de calcul utilisées pendant cette thèse sont présentées. Certaines erreurs communes des différentes méthodes numériques sont étudiées.

Afin de répondre à la première et à la troisième question, les limites de l'amélioration de l'absorption lumineuse, de la génération de photo-courant et de l'efficacité des cellules solaires à couches minces sont étudiées. Les limites de l'amélioration de l'absorption sont obtenues sur une large gamme angulaire ainsi que sur une large gamme de longueurs d'onde pour des couches à texture périodique. La théorie des modes couplés dans le domaine temporel est adaptée afin d'étudier des couches minces ayant une périodicité de l'ordre de la longueur d'onde. Cette méthode est ensuite utilisée afin d'étudier l'effet de l'angle d'incidence et celui de la période du réseau sur l'amélioration de l'absorption dans des couches de 200 nm d'épaisseur et ayant un indice de réfraction n=4. Nous démontrons que l'absorption dépend fortement de la période du réseau ainsi que de l'angle d'incidence et, par conséquent, qu'il est nécessaire de prendre en considération l'incidence oblique dans les simulations. Puis, la limite de l'amélioration de l'absorption lumineuse est étudiée pour différentes structures, y

compris une structure complète représentant un empilement de couches formant une cellule solaire a-Si ayant différentes géométries de réseaux. On démontre que pour des couches minces, un réseau hexagonal améliore l'absorption d'une manière plus significative qu'un réseau carré. L'absorption parasite est considérée comme un obstacle majeur pour le photocourant.
Ensuite, afin de considérer des cas se rapprochant de la réalité, les modes guidés dans les cellules solaires en silicium amorphe sont étudiées par des simulations rigoureuses (deuxième et troisième question). Premièrement, les modes guidés des cellules sont déterminés et analysés dans un modèle planaire équivalent. Ensuite, la texture géométrique est étudiée sur une large gamme angulaire tout en comparant la densité de courant de court-circuit J_{sc} des cellules pour différentes structures de réseau optique. Nous constatons que selon la configuration de la cellule, la texture optimale peut être soit symétrique soit asymétrique. Nous démontrons que la lumière polarisée TM produit un photo-courant plus élevé pour des grands angles d'incidence, et ceci, quelque soit la géométrie de la texture.
Finalement, deux configurations innovantes de cellules solaires à couches minces sont proposées et étudiées. Premièrement, une cellule a-Si plasmonique ne comprenant pas de couche intermédiaire (buffer) est considérée. On démontre que la densité de courant J_{sc} est sensible à l'épaisseur de la couche de silicium dopé de type n. Pour une épaisseur de n-Si inférieure à 10 nm, la cellule plasmonique surpasse une cellule a-Si classique. Deuxièmement, une cellule a-Si avec un réseau périodique de nano-fils en ZnO à l'intérieur de la couche active est simulée. Pour une périodicité de 500 nm, on obtient la densité de courant J_{sc} la plus élevée pour un diamètre des nano-fils de 300 nm.

Mots clés : Énergie solaire, photovoltaïque, couche mince, silicium, piégeage de la lumière, absorption, diffusion, réseau de diffraction, mode guidé, plasmonique, nanoparticule, méthodes numériques pour l'électromagnétisme, simulation optique rigoureuse, théorie des modes couplés

Contents

1 Introduction

1.1 Why solar energy?

Since the early days of industrialization, providing cheap energy has been a concern to develop western economies. Previously, fossil fuels such as coal and oil have been exploited to respond this energy demand. However, industrialization in a global scale requires that the energy sources satisfy other criteria too.

Fig. 1.1 shows the total energy world consumption in the years between 1990-2010 in TWh. Unfortunately, oil, natural gas and coal are the main sources of energy nowadays [1]. Based on energy statistics provided by International Energy Agency (IEA), in 2010, coal, oil and natural gas cover up to more than 81 % of the total word energy supply. These fossil fuels can supply energy temporarily, but in long term, they cannot serve as sustainable energy sources.

First of all, emission of CO_2 by fossil fuels intensifies the greenhouse effect and therefore leads to temperature increase. In 2004, 56.6 % of the total CO_2 emission was due to fossil fuel use. Now we are at the limit of 2 °C temperature increase, which is considered by the scientists as the safe limit of global temperature increase [3]. Eleven of the twelve years from 1995 to 2006 are among the twelve warmest years in our records [4]. Consistent with this, the sea level has been rising at an average rate of 1.8 mm/year over the period from 1961 to 2003 [4] and snow and ice extent of the world has decreased accordingly [4]. These data convey that we are approaching a dangerous regime of climate change. From this perspective, satisfying the increasing energy demand by fossil fuels does not seem a long -term solution because they emit CO_2 which intensifies the greenhouse effect and accelerates the climate changes.

Second, fossil resources can be used to make by-products, which are very useful and essential to industry. In specific, oil, is required to fabricate petrochemicals, which are absolutely necessary for industrial development. It is not clear whether we will be able to replace them by synthetic materials or not; at least in the moment we do not have a replacement for them in many applications.

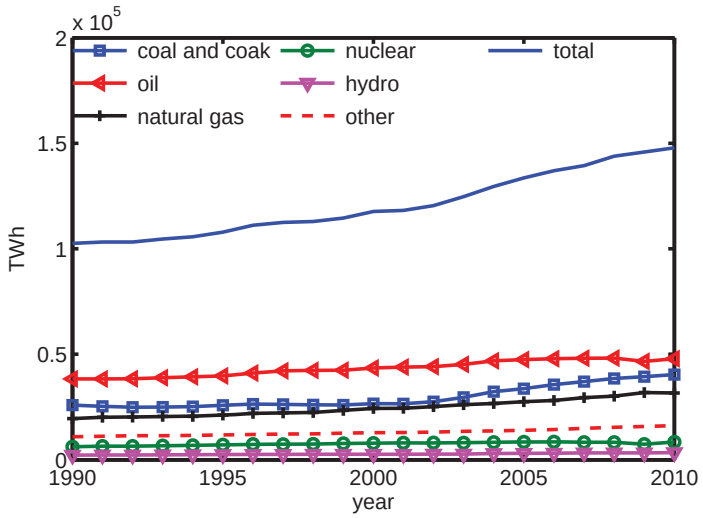

Figure 1.1: Total world energy supply 1990-2010 [1, 2].

Third, fossil fuels are not renewable. They need a long time to form, supposedly millions of years, and if we consume them at the present rate, they will not last more than a few hundreds of years even from an optimist perspective. As our supplies of fossil fuels approach their end, their prices will rise and they will not be economically available as energy sources.

The mentioned points already reveal some of the advantages of renewable energies over fossil fuels. Specifically solar energy seems a good solution to respond the ever increasing global energy demand. It can be considered as an absolutely green energy because it emits no CO_2, thus causes no climate change. Its energy comes from the sun, which practically lasts infinitely long; for a few billions of years, we are safe from going out of sun! The amount of energy that is emitted by sun on earth is larger than one usually imagines. Over one hour, this amount is about 89300 TW [5]. This means that the solar energy emitted on earth in approximately one and a half hour can cover all our annual energy needs!

Solar energy is usually transformed to either electric or thermal energy before being used. If the solar cell produces electricity, sunlight dissociates carriers of different charge and produces a voltage on the two sides of the cell, which is called the "photovoltaic effect"[1]. In the second case, sunlight is focused on a reservoir to increase its temperature. This high temperature can be then transformed into another form of energy. For example, if this reservoir includes a liquid, the increased thermal energy evaporates the liquid and the energy of the vapor can be released into mechanical form in a Carnot cycle. Usually the second approach needs huge plants to be practical but the first one can be applied to a vast variety of applications at different scales. In this thesis, we deal with solar cells which are based on the photovoltaic effect. A solar cell can be made from materials which are found abundantly on

[1]Alexandre-Edmond Becquerel (24 March 1820 – 11 May 1891), who was an expert in optics, electricity and magnetism discovered the photovoltaic effect in 1839. He is the father of Henri Becquerel who won the Nobel prize in 1903 for his works on radioactivity.

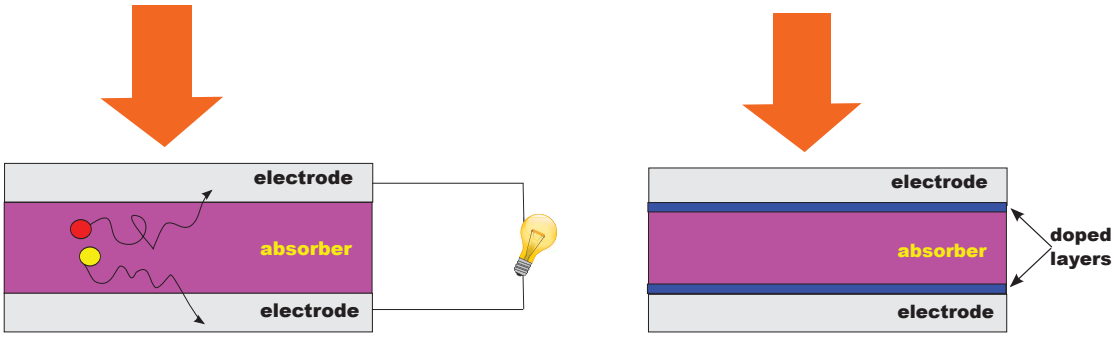

Figure 1.2: (a): Schematics of a thin-film solar cell in an electric circuit. (b): Schematics of a thin-film solar cell with doped layers.

earth and harvesting solar energy is not a waste of precious material compared to burning oil. One remarkable advantage of solar cells is that they can be fabricated at different scales; we do not necessarily need a huge power plant to generate it. Solar cells can be found as tiny as a few square centimeters installed on toys. This flexibility in size brings also the possibility of mobility; for example, the Solar Impulse plane completed recently its journey across the US on solar power alone [6]. Mobility of solar cells brings another advantage in turn. In a conventional electric power generation scheme, a remarkable amount of electricity is lost while being transmitted from plants to consumers. If the solar cell is very close to the users, effectively no power will be lost in transmission.

To be fair, we should also note some difficulties regarding solar energy harvesting. One major concern is about stability of power generation by a solar cell. Because sun light is received only during day, batteries are needed to store surplus energy in daytime and give it back at night. For this, efficient cost-effective batteries are required. Other probable concerns are about CO_2 emission and the energy spent in the solar cell fabrication process. These two have been checked recently and it has been shown that a solar cell pays its fabrication energy back at most in three years [4] and that it is by an order of magnitude less CO_2 emitting than natural gas [4]. Another potential threat of solar cells is their price. However, this should not be a basic problem because first, already in some parts of the world using solar cells instead of fossil fuels is economically justified. Second, with development of technology the price of solar cells are decreasing rapidly. Altogether none of the mentioned problems seems to be an intrinsic barrier against the development of photovoltaics now and in the near future.

1.2 Thin-film silicon solar cells

A solar cell consist of two main parts: absorber and electrodes, as depicted in Fig. 1.2a. Light absorbed in the absorber —which should be a semiconductor —dissociates electrons and holes. The separated electron and hole are presented by red and yellow circles. The role of

electrodes is to collect these optically-generated carriers to the external circuitry. To guide the carriers which are generated inside the absorber towards the electrodes, an electric field may be needed [2]. This internal electric field can be realized by a semiconductor junction, for example a p-n Si junction. However doping increases the recombination rate of carriers, leading to their inefficient collection. One possible solution is to put an intrinsic layer between the p-doped and the n-doped layers, as depicted in Fig. 1.2b. Light is absorbed in both the doped layers and the intrinsic layer. However, only the carriers generated in the intrinsic layer contribute effectively to the photocurrent of the cells. The thickness of the doped layers should be minimized to reduce recombination. On the other hand, the doped layers should have a certain thickness to provide an electric field which is strong enough to collect the generated carriers. The mentioned model of a solar cell may seem over-simplified but it can serve for most of the discussions in this thesis.

A solar cell should be cost-effective, thus, it should be made from abundant materials. Silicon (Si) appears then as an appropriate choice because it is found in vast quantities on earth. Actually it is the second most abundant material in earth crust (27.7 %). Also, Si is non-toxic and is a relatively well-known compared to many other materials. Add to all of these benefits the availability of mature existing silicon technology. A Si solar cell can be made from different forms of Si; wafer, different types of nano- and micro-crystalline, and amorphous. A silicon wafer is a monocrystal which is grown by Czochralski process and then cut into wafers. Thanks to the almost perfect crystalline structure, electronic properties of monocrystalline Si are superior to the other forms of Si, however, its fabrication process is costly. Other forms of Si allow fabrication of cells at lower prices. The price of a cell depends on the Si thickness in it. Wafer-based Si solar cells which are a few hundreds of microns thick are the most expensive Si cells. Other forms of Si cells are thinner and they are called thin-film solar cells but their efficiencies are normally lower than wafer-based Si cells. The thinnest Si solar cells are based on amorphous Si (a-Si). Si thickness in these cells is typically around 300 nm. A-Si cells are the main focus of this thesis. Based on solar cell efficiency tables (version 40)[7], the highest efficiency[3] of a-Si cells were manufactured in Oerlikon Solar Lab in Neuchâtel and is $10.1 \pm 0.3\%$ and. Very Recently, Matsui *et al.* have reported a-Si cell with an efficiency of 10.11%[8]. For crystalline and multicrystalline Si cells, the highest efficiency is $25.0 \pm 0.5\%$ and $20.4 \pm 0.5\%$ respectively. The interested reader is referred to Table. I of [7] for the latest data on the state-of-the-art solar cells of different classes.

Since the first report on the fabrication of an a-Si cell [9], opto-electronic properties of this type of solar cells has been studies extensively. Because of the high density of dangling bonds in a-Si, a cell made of a-Si is not practical. Thus even in the first a-Si cells, hydrogenated a-Si (a-Si:H) was used. It was then observed that under light illumination, the efficiency of a-Si:H cells drops and stabilizes at a lower value than its initial efficiency [10]. This drop of efficiency

[2] Here we have assumed the "drift" of free charge carriers to be the main mechanism of photo-current generation. Although this assumption seems logical for thin-film a-Si solar cells, for wafer-based solar cells "diffusion" plays the main role.

[3] Efficiency of a solar cell is defined as the percentage of incident optical energy that it converts into electricity.

is called light induced degradation or in the name of its discoverers, Staebler-Wronski effect (SWE). Although a clear understanding of the SWE effect is still missing, in a simplified model one can explain it by the high density of dangling bonds in a-Si:H. Later it was shown that a mixture of SiH_4 and H_2 can ameliorate cell stability against SWE [11].Furthermore, it is observed experimentally that thicker a-Si cells suffer more from SWE[12], thus, a-Si solar cells are designed and fabricated with a constraint of 300 nm on their Si layer thickness.

The difference in the crystalline structure of various types of Si is translated into their opto-electronic properties. For example, for microcrystalline Si (μc-Si), the band gap is at around 1.1 eV but for a-Si:H, it is approximately at 1.7 eV[4]. This in turn translates into optical absorption; a-Si:H and μc-Si absorb blue and red light better respectively. To absorb light over a broader spectral range, one can make a multijunction (tandem) Si cell, which consists of an a-Si:H cell on top and a μc-Si cell at the bottom [13].

a-Si cells —which are the main focus of this thesis —can be classified into two main categories based on their fabrication procedure. If first the p-doped Si layer is deposited, and the intrinsic (i-Si) and n-doped Si (n-Si) layers are deposited followingly, the cell is called a p-i-n cell. To fabricate a p-i-n cell, one deposits a transparent conducting oxide (TCO) on glass. Re-

(a) (b)

Figure 1.3: Thin film Si solar cells in (a): p-i-n, and (b): n-i-p configuration. In both configurations fabrication starts from the glass side.

spective deposition of p-Si, i-Si and n-Si forms the absorptive layers. Then the back-reflector covers the previous layers, which consists of either a thick TCO layer ($\approx 1\mu m$) and white paint or a thin TCO layer ($\approx 100nm$) and Ag. A p-i-n cell is shown in Fig. 1.3a. Light reaches the cell layers from the glass side. A second fabrication process can be such that one develops the back-reflector (including a TCO buffer layer) on glass and deposits n-Si, i-Si, p-Si and TCO on top of the back-reflector respectively, as demonstrated in Fig. 1.3b. In this case, glass is underneath the cell and is used as a mechanical support. It can thus be made from other

[4]Optical data of a-Si:H and μc-Si:H are compared in Appendix B

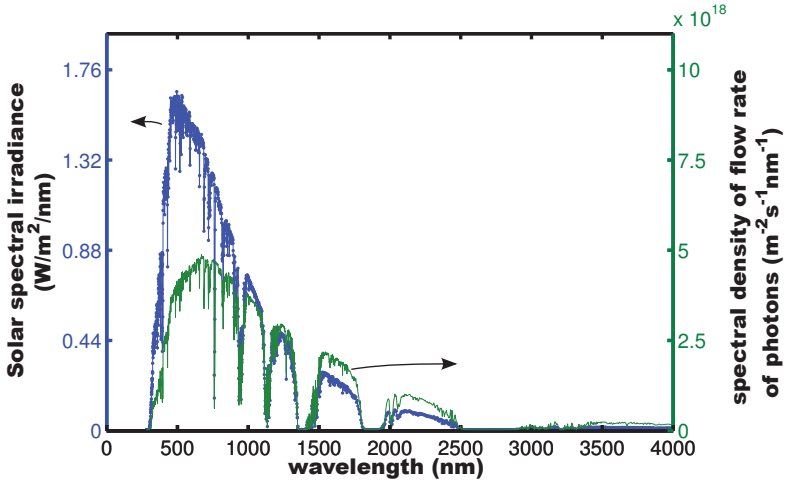

Figure 1.4: Characterisitics of solar illumination on earth (AM 1.5). [15]

materials too. The latter configuration is called the n-i-p configuration because the n-Si layer is deposited first. Note that in both n-i-p and p-i-n configurations, light reaches the p-Si layer before the n-Si layer, I mean physically the p-Si layer is always on top in an operating a-Si cell and this has nothing to do with its being p-i-n or n-i-p.

1.3 Solar illumination

Sunlight intensity is not the same for all wavelengths. Sun illuminates light very similarly to a blackbody at the temperature of at around 5700 °K.

As sunlight passes through earth atmosphere, its spectrum is deviated from its initial form because of absorption and scattering by atoms in the atmosphere. This reduces the incident light intensity from 1365 W/m^2 to 1000 W/m^2 [14]. It is therefore necessary to take into account solar spectrum data on earth to characterize the performance of a normal solar cell[5]. The effect of the atmosphere and also the angle θ that sun makes with a horizontal plane on earth[6] on the solar spectrum is characterized by a parameter called "air mass" which is defined as $AM = 1/\cos\theta$. Solar spectrum outside the atmosphere is called AM0. AM1 refers to the solar spectrum at the equator ($\theta = 0°$) where the impact of atmosphere is applied. For central Europe and North America, usually AM1.5 is used to characterize solar illumination which corresponds to an incident angle of $\theta = 48.19$ degrees. The dotted graph in Fig. 1.4 shows solar spectral intensity for AM1.5.

Let us assume that a photon enters the active layer of a solar cell, for example in the i-Si layer of an a-Si cell. Neglecting free carrier absorption and defects in the active layer, if the energy of this photon is larger than the band gap energy of the absorber, it creates an electron-hole

[5] I exclude the solar cells which are used in outer space from this discussion.
[6] Note the difference between this angle and the incidence angle on the solar cells.

pair (EHP). Here we suppose that each photon can create at most one EHP regardless of its energy.

Photocurrent is an accumulative sum of the EHPs generated by the incident photons at different wavelengths. If the photons which are absorbed in the active layer (i-Si) contribute perfectly to the photocurrent, i.e. if all of them generate EHPs and all of these EHPs are collected, and if absorption in the other layers of the cell do not contribute to the photocurrent, the short circuit current density of the cell can be expressed as

$$Jsc = q\int_{\Delta\lambda}\frac{\lambda}{hc}\Phi(\lambda)\cdot EQE(\lambda)d\lambda \tag{1.1}$$

where λ is the incident photon wavelength, h is Planck's constant, c is speed of light in air, q is electron charge, Φ is solar spectral irradiance, and EQE is the External Quantum Efficiency of the cell. EQE is defined as the ratio of spectral density of EHPs that contribute to the photocurrent to the spectral density of incident photons for each wavelength. In simple words, it shows how much of the energy of the incident light is converted into electrical energy at each wavelength. Because we assumed that all of the light which is absorbed in the i-Si layer contributes to EQE and the other layers of the cell do not contribute to it, EQE can be approximated as the percentage of incident photons which is absorbed in the i-Si layer.

Eq. 1.1 reveals that the number of carriers is not a simple integral of solar spectrum or absorbed light because the wavelength λ appears in the intergral as well. This brings a very important conclusion: more photocurrent is generated at longer wavengths for the same amount of incident light energy. Fig. 1.4 shows the spectral density of flow rate of incident photons. This quantity is obtained by dividing the spectral irradiance $\Phi(\lambda)$ by the photon energy λ/hc. Since each incident photon can produce at most one EHP independent of its exact energy value [7], the latter curve represents the actual contribution of the solar illumination to the number of generated carriers, and thus the photo-generated current. An important conclusion from the mentioned weighting of the spectrum is that the spectrum peak is shifted from its initial wavelength at around 500 nm to the wavelengths about 700 nm. A solar cell should be able to absorb light at around this peak very efficiently. Furthermore, solar illumination has remarkable amount of energy until the wavelength of approximately 2.5 μm. a-Si absorbs strongly from 300 to 600 nm but at around 700 nm it absorbs weakly. Remember also that the i-Si layer thickness in an a-Si cell is limited to around 300 nm. This introduces the main challenge of a-Si cells. It cannot absorb light where it is most effective to do so! It is thus essential to find ways to increase light absorption in an a-Si cell[8].

[7] Photon energy is anyway larger than band gap as assumed primarily.

[8] Here we discuss mainly thin-film a-Si solar cells but absorption enhancement is a general goal for (almost) all types of solar cells.

1.4 Motivation for absorption enhancement: J_{sc}, V_{oc} and FF

Silicon has an indirect electronic band gap which leads to its weak absorption of long-wavelength light. To compensate this weak absorption, the incident light should go long distances through the active layer of Si solar cells. To achieve this, one may use a thick Si layer, which is not practical in many cases. Another solution is to scatter light efficiently in the cell such that it effectively passes a longer way inside the semiconductor.

Having discussed the importance of absorption enhancement to improve J_{sc} in Eq. 1.1, we put a step further and claim that absorption enhancement improves also other important parameters of a cell such as open-circuit voltage and fill factor, although this might not be as evident as improvement in photocurrent. A solar cell's current-voltage characteristic can be described by the diode equation.

$$J = J_{sc} - J_0[e^{qV/kT} - 1] \tag{1.2}$$

where q is electron charge, k is Boltzmann's constant, V and J denote voltage and current density, J_{sc} is the short circuit current density of the cell and J_0 is the cell's saturation current density. The open circuit voltage (V_{oc}) is obtained when $J = 0$.

$$V_{oc} \approx \frac{kT}{q} \ln\left(\frac{J_{sc}}{J_0}\right) \tag{1.3}$$

Fill factor is defined as the ratio of the maximum power to the product of V_{oc} and J_{sc}.

$$FF = \frac{P_{max}}{J_{sc}V_{oc}} = \frac{(VJ)_{max}}{J_{sc}V_{oc}}. \tag{1.4}$$

Fill factor is a very important quantity because finally what matters is not only V_{oc} and J_{sc} but the values of photocurrent and voltage which result in maximal power output. This requires that fill factor is incorporated in the calculations as well. Maximum power can be obtained from Eq.1.2 by solving $\partial(JV)/\partial V = 0$ which leads to

$$J_{sc} - J_0 e^{qV_{opt}/kT}\left(1 + \frac{qV_{opt}}{kT}\right) = 0 \tag{1.5}$$

where V_{opt} represents the voltage at the point with maximal output power. Based on the latter equation V_{opt} can be increased by

1. increasing J_{sc}: which means more efficient light absorption in the cell

2. reducing J_0: which is linked to the electronics of the device.

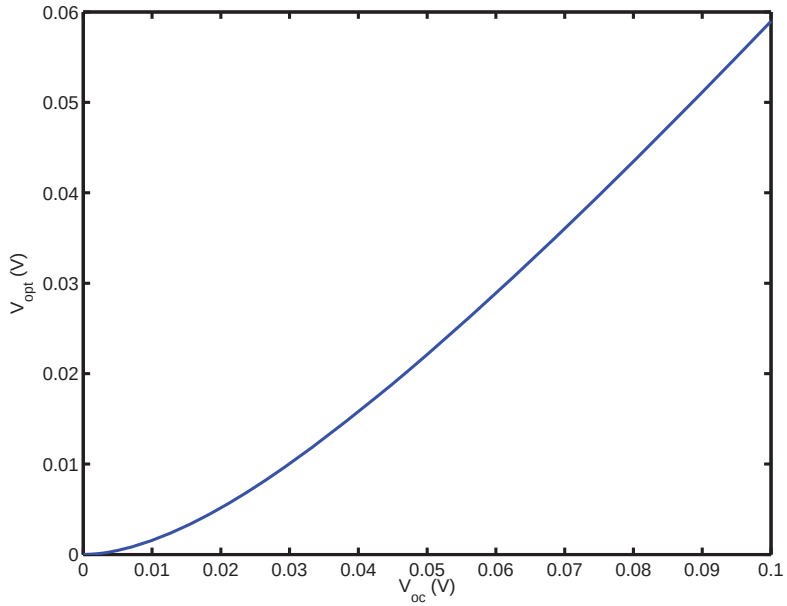

Figure 1.5: Variations of V_{opt} as a function of V_{oc}.

The saturation current density (J_0) is a basic parameter for a solar cell's operation. It gives a measure of the dissipative processes in the cell. More specifically, it is related to the amount of non-radiative recombination in the cell. Internal luminescence yield of a silicon cell is fundamentally limited by Auger recombination [16] , which is in turn proportional to the thickness of the absorber material [17]. Thus, making a solar cell thin, not only leads to less material consumption, but also reduces the unwanted dissipative processes which increase the saturation current; thus it increases the efficiency.

Comparison of Eqns. 1.3 and 1.5 results in

$$V_{opt} + \frac{kT}{q} \ln\left(1 + \frac{qV_{opt}}{kT}\right) = V_{oc} \tag{1.6}$$

which due to the slightly varying behavior of the natural logarithm can be approximated as

$$V_{opt} = V_{oc} - \frac{kT}{q} \ln\left(1 + \frac{qV_{oc}}{kT}\right). \tag{1.7}$$

Fig. 1.5 shows V_{opt} as a function of V_{oc} at the temperature of 300°K based on Eq. 1.7. Clearly, V_{opt} is a monotonic function of V_{oc}. Thanks to monotonicity of both Eq. 1.5 and Eq. 1.7, it is possible to link these two equations and conclude that an increase in J_{sc} results in an increase in V_{oc}. Therefore, the efficiency (η) of a cell, which is defined as the amount of incident optical energy that it converts to electric energy, can be improved by absorption enhancement.

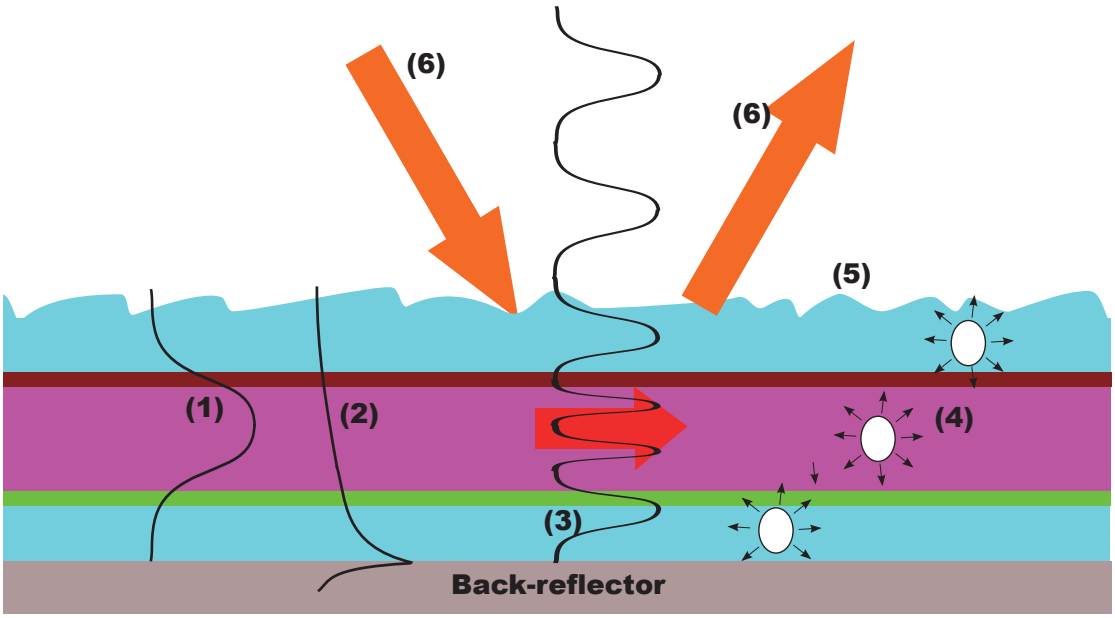

Figure 1.6: Most popular techniques for absorption enhancement. The profiles show from left to right a guided mode (which is not plasmonic) (1), a plasmonic mode (2) and a radiation mode (3). Light scattering nano-particles (4) can be put in different layer of a thin-film solar cell. The layers are textured to maximize light coupling into the cell. All of the layers are usually textured but here only the front texture (5) is shown. Light coupling from outside to the cell and from inside the cell to outside is reciprocal [18]; i.e. coupling coefficient is the same for both in- and out-coupling.

1.5 Light trapping in thin film silicon solar cells

Absorption can be enhanced in an a-Si cell by modifying its geometry. It is true that bulk properties of a-Si influence its optics dominantly at around 700 nm, however, by modifying a cell's geometry one can potentially enhance absorption in it. Light trapping is applying geometrical changes to a cell to improve light absorption in it.

As a primary goal, it is desired to reflect as little light as possible. Reflection from the cell's top surface can be minimized by choosing the front TCO such that it act as an anti-reflection coating between air and absorber. Thickness and texturing of the front TCO play a decisive role in reflection [19]. Apart from the front TCO layer, thickness of the back TCO layer can be varied to maximize light intensity inside the cell's active layer. Thickness of the doped layers is usually kept minimal because of the large recombination rate in them.

Fig. 1.6 shows some other popular approaches to enhance absorption in a thin-film solar cell. A very well-known method is to put back-reflector underneath the cell. The back-reflector reflects light after its first passage through the cell thickness and gives it a second chance to be absorbed.

A second approach to enhance absorption is related to the optical modes of the cell. An optical mode is a solution of Maxwell equations for the desired structure. In a planar multilayer

stack, two types of modes can be found: guided modes and radiation modes. Guided modes are modes which are completely isolated from the outside medium. Their being decoupled from outside the cell is evidenced by their decay in amplitude outside the cell. Contrarily, radiation modes do not vanish even at far distances from the cell and their profile oscillates up to infinity. Radiation modes can exchange energy with the ambient. Excitation of guided or radiation modes introduces peaks into the EQE of the solar cell, thus enhances absorption. While radiation modes are available for excitation in a planar device, to excite guided modes one can deviate the geometry from perfect planar to textured. Subsequently, interface texturing is a second approach to enhance light absorption in a solar cell. The interface texture can be random or periodic. To date the most promising results have been obtained by random textures . Theoretical studies, however, predict the possibility of more effective absorption with periodic textures [20].

The introduction of a metallic back-reflector underneath the cell results in a special type of guided modes, which are called plasmonic modes (or surface plasmons). Normally a guide mode is localized in the dielectric layers of a solar cell. A plasmonic mode is contrarily localized at the interface between the metal and the adjacent dielectric. This localization at the metallic interface is a characteristic of a plasmonic mode. As Fig. 1.6 shows, localization of the plasmonic mode to the metallic interface results in existence of a wave-tail inside the metallic layer. This penetration into metal results in a considerable amount of parasitic absorption for a plasmonic mode and is a bottleneck for the application of plasmonics to solar cells [21, 22, 23]. It is possible to fabricate almost perfect light absorbers over the whole optical band [24] but collecting this absorbed energy into the form of photocurrent has not been realized efficiently yet to my knowledge. The profile of plasmonic modes depends strongly on the interface texture. It is not clear how far one can localize the plasmonic mode profile in the dielectric layer, and thus get rid of parasitic losses. Furthermore, a metallo-dieletric interface can have a high density of defects, which may increase the recombination rate and reduce the photocurrent corresponding to the plasmonic mode excitation.

Embedding nano-particles inside the cell is another method to enhance light trapping. These nano-particles can be incorporated in different layers of a cell. Nano-particles in a cell can improve light absorption in different ways. First, they can scatter light and locally increase light intensity in their adjacent regions. Second, they can effectively act as a layer inside the cell and introduce a guided mode into the cell's dispersion diagram. Both metallic and dielectric nano-particles can be used to enhance absorption in the cell. However, metallic particles can absorb light depending on their size [25]. Recently, cells with metallic nano-particles have been fabricated which can excel cell's based on interface textures. These cells benefit from light scattering from nano-particles which are incorporated in the back TCO layer [26].

Dielectric nano-particles can enhance absorption in the solar cell [27, 28]. In chapter 6 I investigate incorporation of ZnO nano-particles inside the i-Si layer and I show that large nano-particles can improve absorption in the cell significantly. However, one should note

that embedding metallic or dielectric nano-particles may cause problems for a cell's operation, especially for carrier collection. The boundary between the nano-particles and the i-Si layer may have a high defect density, and therefore, result in a dramatic recombination rate. The mentioned points seem interesting to be investigated experimentally to determine the practical limits of a cell with nano-particles inside the i-Si layer.

The methods of absorption enhancement are usually tightly entangled to each other in a thin-film solar cell, especially in an a-Si cells. For example, texturing the front TCO changes reflection and coupling to guided modes simultaneously. It seems therefore not strictly correct to distinguish these effects and to try to optimize them separately because they are interwoven and once one of them changes, it affects all of the other parameters. Practically, however, it seems often inevitable to simplify the cell optimization problem and to assume that the different optical parameters are not tightly correlated, at least to some extent.

A common misleading interpretation is that in an ideal light-trapping scheme, one tries to let as many photons as possible into the cell, then should block them there to let the cell absorb them. Even if the cell is weakly absorbing, the photons will be absorbed in the cell provided that they remain trapped in it for a long-enough time. This idea may seem brilliant at first, but unfortunately its correctness is limited to the conceptual level. The physical constraint which limits the applicability of this idea is the electromagnetic reciprocity. Coupling from outside into the cell and from the cell to the external medium is reciprocal. If a photon can enter the cell easily, it can also go out easily and vice versa. It is recently shown that to enhance absorption, one should not try to trap photons inside the cell; contrarily, it is necessary to let them come into the cell and go out as freely as possible [20], which means increasing coupling. Hence, one should not be misled by the term "light trapping" and interpret it as a longer photon life time inside the cell. From this point of view, works on absorption enhancement in solar cells by using "slow light" are conceptually questionable. The interested reader is referred to [20].

As already mentioned, to increase absorption one can excite guided modes of the cell—which are a main topic of investigation in this thesis. Now two main questions arise:

1. How far can mode excitation enhance absorption in a solar cell?
2. How can we excite guided modes most effectively?

The first question has been studied since a few decades [29, 30, 31, 20] . As light absorption and efficiency of a solar cell are not independent, some other authors have been able to obtain limits for the efficiency of solar cells with similar assumptions [32, 33]. Efficiency of a solar cell is defined as the amount of optical energy that is converted into electric energy. From optical simulations, one can get an approximation of the photocurrent according to Eq. 1.1.

To respond the second question, one can primarily use a coupled-mode approach [18]. Coupled-

mode theory predicts approximately the changes of coupling strength as a function of geometry. However, when deviation from planar geometry is remarkable, the coupled-mode approximation becomes less accurate. Furthermore, near field effects are not considered in the coupled-mode solution. This obliges one to perform rigorous calculations to evaluate absorption in the solar cell accurately. In chapter 5 of the thesis, guided modes and their effect on absorption enhancement are studied in detail by considering various cell geometries.

1.5.1 Is Lambertian scattering optimal?

A Lambertian scatterer is an object which scatters light isotropically [9]. Although Lambertian scattering resembles a black-body radiation in the sense that it does not distinguish direction, and because of this sometimes in the literature it is assumed to be the ideal case or a goal to achieve [34, 35], it seems unlikely that a Lambertian scatterer can be a close-to-ideal form of scattering at least for thin-film solar cell with wavelength scale texture. In these cells, the directionality of light scattering from and in the cell can be manipulated by engineering the shape of the interfaces, thickness of the cell and using surface effects.

1.5.2 Guided modes and plasmonics

Guided modes of a solar cell do not transfer energy with the ambient unless the cell is deviated from planar geometry. [10] Recently guided modes have been used to enhance light absorption in thin-film solar cell [36, 37]. Still, optical behavior of the cells that are very thin (thinner than a few hundred nano-meters) and have wavelength-scale periodic texture, and absorption enhancement by guided-mode excitation in these cells seems interesting for research.

Using plasmonics is another approach which seems to have a potential to boost absorption in solar cells [38]. Unfortunately up to date, plasmonics has not lead to state of the art cells. More unfortunate, it is not addressed in the literature that the cells which are claimed to be using the concept of plasmonics (e.g. [39]) are not really benefiting from the existence of plasmons. Even it has been suggested that these cells are using guided modes and not surface plasmons [40]. Therefore, it seems essential to study these cells in more detail and to realize to what extent true plasmons have been used in them.

It is worth mentioning that using metals in solar cells does not necessarily mean using plasmonics. Even if near field absorption enhancement due to the presence of a metallic structure is observed, it is not necessarily an improvement due to a plasmonic mode. In chapter 6 I mention an example where absorption is improved due to near field enhancement at a metallic interface. However, the polarization which is assumed in the example does not allow the existence of plasmonic modes. Thus, every near field enhancement close to a metallic

[9] This naming is in the honor of Johann Heinrich Lambert who introduced the concept of perfect diffusion.

[10] For simplicity, we do not refer to plasmonic modes as guided modes unless specified, although they apply to the definition of guided modes.

interface should not be considered as a plasmonic resonance. This makes the claim of using plasmonics in thin-film solar cells rather weak. Often in a thin film a-Si cell a TCO layer is put between the metallic layer and the absorber. However, the existence of this TCO layer contradicts the concept of using the near field to enhance absorption. From this point of view, it seems that plasmonics has not been exploited to improve absorption in solar cells to its full potential yet.

1.6 Importance of correct optical simulation

It should have been clear by now that it is of utmost importance to perform accurate calculations for the optical simulation of thin-film solar cells. It is absolutely necessary to obtain the electromagnetic field with high accuracy such that near field effects —which can have a definitive effect on the final value of light absorption in the solar cell —can be correctly calculated. From this point of view, approximate theories such as the coupled-mode theory [41, 18] do not provide detailed information about the absorption in the cell because they do not take into account near-field effects. For optimization of a solar cell geometry from an optical perspective, reliable calculation is an essential, otherwise the calculation error may dominate the changes in the results imposed by structure modifications and give wrong results.

Different methods may be proposed for the rigorous simulation of thin-film solar cells. Numerical methods can solve Maxwell equations in time-domain such as the finite-difference time domain (FDTD) or in frequency domain such as the finite element method (FEM) in frequency domain, the rigorous coupled wave analysis (RCWA), finite difference frequency domain (FDFD) method and the multiple multipole method (MMP). Most of these methods, especially the FEM and the FDTD methods are extensively used in literature to model the optics of solar cells. However, little attention has been paid to verify the accuracy of these calculations. From this point of view, a lot of these simulations are questionable, especially when it comes to optimization.

To model solar cells with the FDTD method one should be extremely careful because there are multiple factors which make this method very vulnerable to numerical errors, which cannot always be detected easily. One important drawback of FDTD is its numerical dispersion. This means that based on the order of the FDTD algorithm which is used, the wavelengths may be shifted. Normally a higher order algorithm suffers less from numerical dispersion [42]. Another problem is the high density of grid points needed to guarantee numerical accuracy. Also FDTD simulations are time consuming. Contrarily, one can simulate a wide band of wavelengths in one FDTD run, which may seem an advantage, but the following post-processing may be time-consuming. Also, to implement dispersion, it is necessary to express material dispersion in terms of a summation of poles of predefined types, for example Lorentzian poles. This introduces an unnecessary approximation of the optical data into the simulation, and when the dispersion form is complicated, slows down the simulation be-

cause simulation time is proportional to the number of poles which are used to approximate the optical data. In FDTD, the grid size limits the time-step duration; a finer mesh means a slower simulation. This disadvantage is even more pronounced when dispersive materials are used because they may cause instabilities for the simulation and to stabilize the simulation, it may be necessary to set the time-step to smaller values than the ones allowed by the Courant stability factor [42]. Altogether, FDTD does not seem an optimal approach for simulation of solar cells.

Frequency domain methods seem more adapted to the simulation of solar cells. One important advantage of them is that they do not suffer from numerical dispersion. Also, they can use tabular optical data without any approximation and their speed does not depend on optical data. As examples of this group of simulations, one can mention recent publications which use FEM [43] or RCWA [44, 45] to simulate solar cells.

Different parameters should be considered to guarantee the accuracy of frequency domain simulations of solar cells. For full numerical methods such as the FEM, the mesh should be fine. To guarantee the accuracy of the method usually ten to twenty mesh points are necessary per wavelength [46, 47, 48, 42]. The final limit to grid size can be obtained by application of the Nyquist theorem. Furthermore, at boundaries, especially at metallic boundaries, a high mesh resolution is essential so that the method can take into account field discontinuities at these boundaries. Because these methods are often modal methods, enough modes should be used in the corresponding expansion. The latter point is more critical for asymmetric patterns. Overall it seems that for large-scale simulations, especially the cells thicker than $1\mu m$, very strong computer facility is needed to have reliable results. To the author's knowledge the numerical stability of the FEM simulations of μc-Si cells or tandem cells has not been strictly verified; nevertheless acceptable correspondence to the experiments has been obtained [49, 50].

Semi-analytical methods such as RCWA have an intrinsic advantage over full numerical methods. Their complexity does not depend on a cell's thickness. This means that RCWA simulation of μ-c Si cell or a tandem Si cell is as complex as the simulation of a thin film a-Si solar cell. However, one should take care to implement the boundary conditions correctly. Especially at metallic interfaces, a huge number of modes may be necessary to provide accurate results. A remarkable improvement in the convergence of RCWA has been achieved by implementation of the fast Fourier factorization [51]. Exponentially convergent results can be obtained by polynomial expansion of the fields [52] or adaptive spatial resolution (ASR) [53]. Polynomial expansion is harder to implement and it is not optimal for complicated textures. The problem with ASR is that with the present formulation, its implementation to more than one layer is unstable in the general case.

A common approximation which can sometimes introduce considerable error to the frequency domain calculations is the slowly varying approximation (SWA). This is discussed in section 2.5.2. Briefly, when materials are strongly dispersive at the wavelengths under investigation,

absorption should be obtained through a more complicated formula compared to the form usually used in literature [54, 43, 37, 44].

1.7 About this thesis

During this thesis I have focused on the following objectives:

- Preparation of codes to simulate thin film structure with different geometries (planar, 1D gratings and 2D gratings), and comparison of different methods for the analysis of thin-film Si solar cells.
- Studying the upper bound of absorption enhancement in thin-film a-Si solar cells, and trying to find ways for improvements.
- Studying unconventional structures which can enhance the photocurrent in a thin-film solar cell.

Chapter 2 and 3 of the thesis provide an overview of the numerical approaches that I have studied or used during the project.

Chapter 4 discusses the limits of absorption enhancement in solar cells through three different arguments. First, the limits on photocurrent enhancement are studied. In literature, thick solar cells have been extensively investigated. Also, thin films with random textures have been considered [30] Here, for the first time a thorough study of the upper bound of absorption in thin-film solar cells with wavelength-scale periodicity is performed. Then, limitation on external coupling of solar cells is studied in chapter 4. A limit is obtained for the strength of coupling to the optical modes of a solar cell. Finally, the bounds on efficiency are discussed.

Chapter 5 is devoted to the study of guided waves in thin-film a-Si solar cells. Specifically, the role of back TCO is studied in detail. Also, we assume that the back-reflector of the cell is shaped into a grating pattern and we investigate the dependence of the EQE and J_{sc} of the cell on the geometrical parameters of the back-reflector such the grating depth and symmetry of the grating pattern. These investigations are done over broad range of incidence angles and thus provide a deep insight towards the optical properties of the solar cell.

In chapter 6, we study two different approaches for absorption enhancement in thin-film solar cells: elimination of the buffer layer between the metallic back-reflectors and the Si, and incorporation of dielectric nano-particles in the cell. We show that from the optical point of view, both methods can ameliorate a-Si solar cells.

2 Electromagnetic theory for thin-film multilayers

In this chapter we briefly go over general properties of electromagnetic waves in thin films. Later in chapter 3, some techniques to calculate the fields will be mentioned.

2.1 Some definitions

Before going on, let us introduce some definitions which are commonly used during the thesis. Polarization of light is defined in different ways in the literature. Assume a planar geometry such as the one depicted in Fig. 2.1a which is illuminated by a beam of light at an angle θ. The incidence plane is defined as the plane in which both the incidence and the reflected beams occur. For plane-waves, the incidence plane can be defined as a plane spanned by the wave-vectors of the incident and the reflected beams. The transverse electric (TE) polarization is the case where the electric field is normal to the incidence plane. The transverse magnetic (TM) polarization is the case where the magnetic field is normal to the incidence plane.

Relief structures that are periodic along one direction (e.g. x) as depicted in Fig. 2.1b and variant along z direction are called one-dimensional (1D) gratings. Incidence of light on 1D gratings can lead to diffraction. Still if the wave-vector of the incident plane-wave is normal to grating grooves, two polarizations can be distinguished. In this case, the incident and reflected wave-vectors occur in one plane, which is called the incident plane. Similar to the case of planar structures, if the electric or the magnetic field is normal to the incidence plane i.e. along grating grooves, the polarization is called TE or TM.

Normal incidence is the case where the incident wave-vector is perpendicular to $x-y$ plane for both planar structures and gratings. If the incidence is not normal, it is called oblique. For 1D gratings under oblique incidence, if the incident wave-vector is perpendicular to the grating grooves, the incidence is called in-plane, otherwise it called out-of-plane. For out-of-plane incidence on 1D gratings and for incidence on two-dimensional (2D) gratings [1], the TE

[1] Two-dimensional gratings are periodic along two linear-independent directions in $x-y$ plane.

and TM polarizations cannot be distinguished.

2.2 Maxwell's equations in guided wave structures

Maxawell's equations for source free fields in a charge free medium can be expressed in time domain in the following form.

$$\nabla \times \tilde{\mathbf{E}} = -\frac{\partial \tilde{\mathbf{B}}}{\partial t} \tag{2.1}$$

$$\nabla \times \tilde{\mathbf{H}} = \frac{\partial \tilde{\mathbf{D}}}{\partial t} \tag{2.2}$$

In the harmonic regime, we can write

$$\tilde{\mathbf{E}}(t) = \mathbf{E}\exp\left(j\omega t\right) + \mathbf{E}^{*}\exp\left(-j\omega t\right) \tag{2.3}$$

where ω is the angular frequency and $j = \sqrt{-}1$. Through using permittivity ϵ and permeability μ and by applying the consitutive relations

$$\mathbf{D} = \epsilon\mathbf{E} \tag{2.4}$$

$$\mathbf{B} = \mu\mathbf{H} \tag{2.5}$$

to Maxwell's equations at single frequency, we can rewrite Maxwell's equations.

$$\nabla \times \mathbf{E} = -j\omega\mu\mathbf{H} \tag{2.6}$$

$$\nabla \times \mathbf{H} = j\omega\epsilon\mathbf{E} \tag{2.7}$$

In the absence of surface charge and surface current, the following boundary conditions apply

$$\mathbf{H}_{\parallel,1} = \mathbf{H}_{\parallel,2} \tag{2.8}$$

$$\mathbf{H}_{\perp,1} = \mathbf{H}_{\perp,2} \tag{2.9}$$

$$\mathbf{E}_{\parallel,1} = \mathbf{E}_{\parallel,2} \tag{2.10}$$

$$\mathbf{D}_{\perp,1} = \mathbf{D}_{\perp,2} \tag{2.11}$$

where the subscripts $\perp$ and $\parallel$ refer to the normal and tangential components of the specified field. Considering wave propagation in x direction, it is possible to separate the components

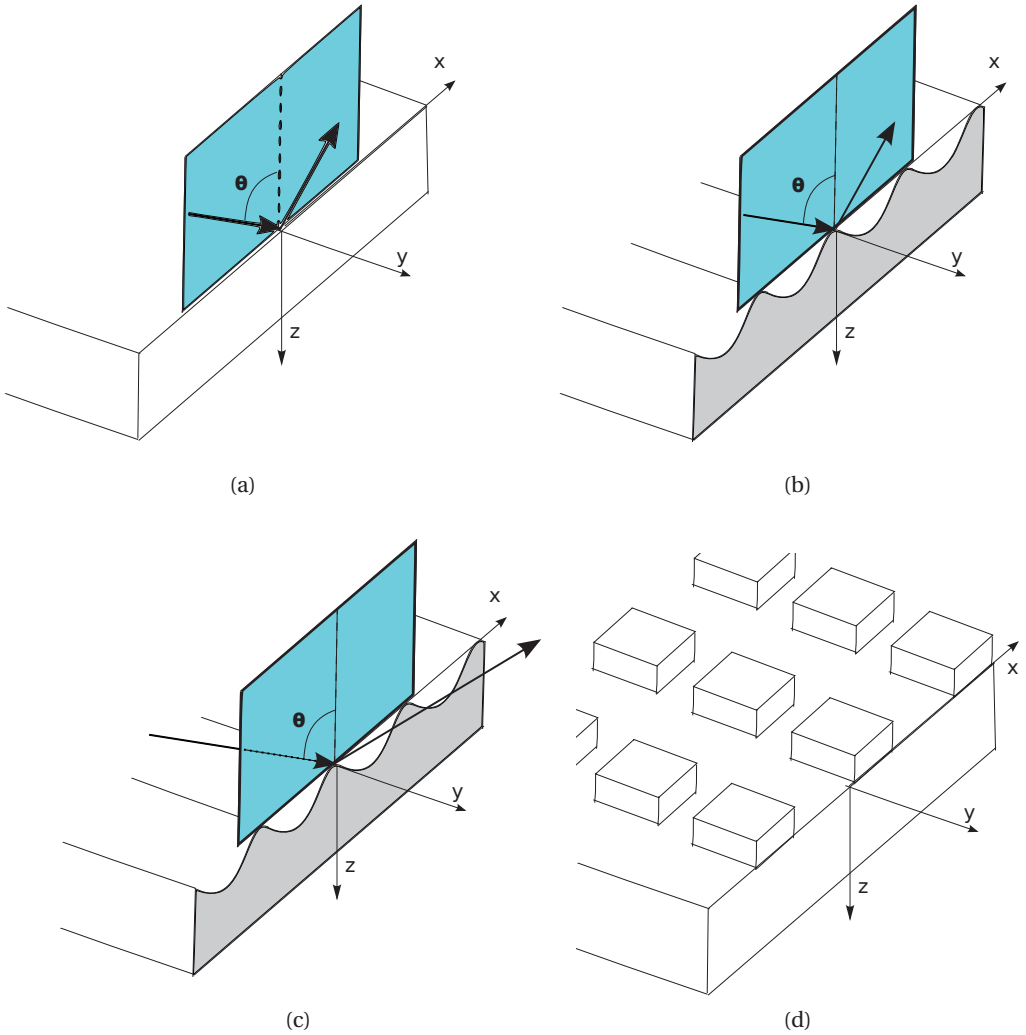

Figure 2.1: (a): Incidence plane for a planar structure, (b): In-plane incidence for a 1D grating, (c):Out-of-plane incidence for a 1D grating, (d): A 2D grating. For 1D gratings, the wave-vector of the incident and the 0-th order reflection are plotted.

of the electric and the magnetic fields in the propagation direction and transverse to it.

$$\nabla_t \times \mathbf{E}_t = -j\omega\mu\mathbf{H}_x \tag{2.12}$$

$$\nabla_t \times \mathbf{H}_t = j\omega\epsilon\mathbf{E}_x \tag{2.13}$$

$$\nabla_t \times \mathbf{E}_x + \hat{x} \times \frac{\partial \mathbf{E}_t}{\partial x} = -j\omega\mu\mathbf{H}_t \tag{2.14}$$

$$\nabla_t \times \mathbf{H}_x + \hat{x} \times \frac{\partial \mathbf{H}_t}{\partial x} = j\omega\epsilon\mathbf{E}_t \tag{2.15}$$

Here the transversedel (∇_t) is defined as

$$\nabla_t = \left(0, \frac{\partial}{\partial y}, \frac{\partial}{\partial z}\right) \tag{2.16}$$

2.3 Optical modes in planar structures

Solving source-free Maxwell's equations in multilayers results in two main non-trivial classes of solutions. The first type of solutions, which are called guided modes, are mainly confined to the multilayer and they tend to zero at infinity in both half-spaces on top and bottom of the multilayer. Because a multilayer structure can support guided modes, it is sometimes called a "guide". The other type of modes are called radiation modes and do not vanish in distances far from the multilayer. If the refractive index depends only on one direction, for example z, the modes are confined only in z direction. Assuming that the wave propagates in x direction, a mode's dependence on x can be expressed as $\exp(-j\beta x)$ where β is the mode propagation constant. A planar guide supports both transverse electric (TE) and transverse magnetic (TM) modes. A TE mode is a mode with no longitudinal electric field, i.e. $E_x = 0$. Similarly a TM mode has no longitudinal magnetic field. We treat these two polarizations separately.

2.3.1 TE polarization

In TE polarization, the magnetic field has no component in y direction, i.e. $H_y = 0$. This together with the assumption $\partial/\partial y(.) = 0$ and Eq. 2.13 means that the electric field is normal to the propagation direction, i.e. $E_x = 0$. Also Eq. 2.14 results in $E_z = 0$ which shows that power flows only in x direction. Eq. 2.14 furthermore leads to the following equation

$$\frac{\partial E_y}{\partial z} = j\omega\mu H_x \tag{2.17}$$

Thanks to the simple form of dependence of the fields on x direction, one can simplify derivation in this direction; $\partial/\partial x(.) = -j\beta(.)$. So, from Eq. 2.14, one finds that

$$\beta E_y = \omega\mu H_z \tag{2.18}$$

By combining Eqs. 2.15, 2.17, and 2.18 one concludes that

$$\frac{\partial^2}{\partial z^2} E_y = \left(\beta^2 - \epsilon k_0^2\right) E_y. \tag{2.19}$$

The last equations shows that one can solve a scalar equation to find E_y. Other field components can be obtained versus E_y. Specifically, H_z has the same phase as E_y, thus it carries power in x direction due to Poynting theorem.

2.3.2 TM polarization

In TM polarization, $H_x = H_z = E_y = 0$. Also,

$$\frac{\partial H_y}{\partial z} = -j\omega\epsilon E_x \tag{2.20}$$
$$\beta H_y = \omega\epsilon E_z \tag{2.21}$$

In this case it is possible to find a scalar equation for H_y.

$$\epsilon\frac{\partial}{\partial z}\left[\frac{1}{\epsilon}\frac{\partial}{\partial z} H_y\right] = \left(\beta^2 - \epsilon k_0^2\right) H_y. \tag{2.22}$$

2.4 Waves in textured multilayers

If the interfaces of the structure are textured, field components take a more complicated form compared to the case of planar device. Such a geometry can be a two-dimensional (2D) or three-dimensional (3D) structure. In 2D structures still two distinct polarizations can be uncoupled for in-plane incidence. By in-plane I mean that the incidence plane is normal to the geometrical invariance direction as depicted in Fig. 2.1b. For each polarization the vectorial form of Maxwell's equations is reduced to a scalar equation which is much easier to solve than its original form. In 3D strucures and out-of-plane incidence (Fig. 2.1c) wave-coupling is more complicated and cannot be separated into different polarization directions. Therefore, it is required to solve vector Maxwell's equations.

2.5 Additional notes

2.5.1 Refractive index and permittivity

In the general case, the refractive index can have a real and an imaginary part. Its imaginary part, κ, is usually called the extinction coefficient and shows loss or gain in the medium and its real part n is called the refractive index and demonstrates the wavelength in the medium; higher n means a more compressed wave and shorter wavelength. In a medium with refractive index n and an extinction coefficient κ wave propagation can be described by exponential terms of form $\exp(-j\mathbf{k}.\mathbf{r})$ where $\mathbf{k} = (n + j\kappa)k_0\hat{\mathbf{k}}$. If the medium does not amplify the wave, the extinction coefficient counts for loss. Therefore wave propagation along the propagation direction must result in decay of the field energy. This requires that the extinction coefficient κ must be negative. Thus we normally write the refractive index as $n - j\kappa$ where $n, \kappa > 0$. Permittivity can then be expressed as $\epsilon = (n - j\kappa)^2 = (n^2 - \kappa^2) - j2n\kappa$.

2.5.2 Slowly varying approximation and absorption calculation

Eq. 2.3 defines the field as a real quantity obtained by superposing two complex terms. Approximation of the electric field $\tilde{\mathbf{E}}$ with the complex-valued amplitude $\mathbf{E}$ which does not depend on t is called slowly varying approximation. For solar cell simulation and analysis, this approximation is valid. The Poynting vector is defined as the multiplication of electric and magnetic fields

$$\tilde{\mathbf{S}} = \tilde{\mathbf{E}} \times \tilde{\mathbf{H}} \tag{2.23}$$

By using the slowly varying approximation we can write

$$\begin{aligned} \tilde{\mathbf{S}} &= \left[\mathbf{E}\exp\left(j\omega t\right) + \mathbf{E}^* \exp\left(-j\omega t\right)\right] \times \left[\mathbf{H}\exp\left(j\omega t\right) + \mathbf{H}^* \exp\left(-j\omega t\right)\right] \\ &= \Re\left\{\mathbf{E}\times\mathbf{H}^*\right\} + \Re\left\{\mathbf{E}\times\mathbf{H}\exp\left(2j\omega t\right)\right\} \end{aligned} \tag{2.24}$$

The time-averaged Poynting vector can be expressed as

$$< \mathbf{S} > \;=\; \Re\left\{\mathbf{E}\times\mathbf{H}^*\right\} \tag{2.25}$$

Using a similar argument one can conclude that absorption over a volume V can be approximated by

$$A = \frac{\omega\epsilon_i}{2}\int_V \left|\mathbf{E}^2\right| d\mathbf{r} \tag{2.26}$$

We use Eq. 2.26 to calculate absorption in this work. One should however note that in Eq. 2.26 slowly varying approximation has been used and absorption expression is more complicated in the general case [55, 56].

2.5.3 External quantum efficiency

The external quantum efficiency (EQE) of a solar cell is the ratio of collected carriers to the number of incident photons. We assume that loss is mainly optical and once a photon is absorbed in the active layer of a cell, it can effectively result is a collection of a carrier. Furthermore, we assume that other layers of a cell do not contribute to the photocurrent. Using these assumptions, the EQE can be expressed as

$$EQE = (1 - R - T) \times \frac{\int_{i-Si} \epsilon_i \left|\mathbf{E}^2\right| d\mathbf{r}}{\int_{cell} \epsilon_i \left|\mathbf{E}^2\right| d\mathbf{r}} \tag{2.27}$$

The short circuit current density (J_{sc}) can be calculated from EQE by using Eq. 1.1.

3 Numerical methods for exact calculations

In this section the different computational methods which were used during the thesis are explained. First, the transfer matrix method which is used to analyze planar multilayers is discussed in section 3.1. Analysis of a cell as a planar multilayer can provide primary knowledge about light absorption in the cell, however, to take into account the effect of texturing, one needs to use more complicated approaches. In this thesis, the Rigorous Coupled Wave Analysis (RCWA) method is used to model a cell based on a multilayer with periodically textured interfaces. Section 3.2 discusses the RCWA method and different possibilities to ameliorate its convergence. The last section of this chapter discusses other possible methods to simulate thin-film solar cells and my methods for 3D calculations. Note that in this chapter we only explain the simulation procedures; the results are presented in the corresponding chapters later.

3.1 Planar multilayer

In a planar multilayer, Maxwell's equations take a simple form thanks to simplicity of geometry. Different methods can be used to analyze these flat multilayers [57, 58, 59, 60]. Here we introduce the transfer matrix method.

3.1.1 Transfer matrix method for planar multilayers

Our analysis of planar multilayers is based on the formulation mentioned in Ref. [61]. We assume the convention that the field has a time dependence of the form $\exp(j\omega t)$. Polarization definition is similar to the definitions mentioned in section 2.1. Assume that an incident beam illuminates the structure at and angle θ. The description includes two separate polarizations which are completely decoupled and lead to a scalar equation for each polarization (Eq. 2.19 or Eq. 2.22). The latter scalar equation is expressed versus a scalar field Ψ which is the electric field in TE polarization and the magnetic field in TM polarization. This scalar

field can be expressed in the i-th layer of the multilayer structure as

$$\Psi_i = A_i \exp\left[-j\kappa_i (z - z_{i-1})\right] + B_i \exp\left[+j\kappa_i (z - z_i)\right] \tag{3.1}$$

where $\kappa_i = \sqrt{\beta^2 - (n_i k_0)^2}$, n_i is the layer refractive index, and A_i and B_i are the coefficients of forward and backward waves in the i-th layer. Continuity of the tangential components of the electric and the magnetic fields helps one to link the coefficients of forward and backward waves in the following form.

$$\begin{pmatrix} A_t \\ B_t \end{pmatrix} = Q_{M-1} Q_{M-2} \cdots Q_0 \begin{pmatrix} A_i \\ B_i \end{pmatrix}, \tag{3.2}$$

$$Q = \frac{1}{2} \begin{bmatrix} \left(1 + f_i \frac{\kappa_i}{\kappa_{i+1}}\right) \exp(-\kappa_i d_i) & \left(1 - f_i \frac{\kappa_i}{\kappa_{i+1}}\right) \exp(\kappa_i d_i) \\ \left(1 - f_i \frac{\kappa_i}{\kappa_{i+1}}\right) \exp(-\kappa_i d_i) & \left(1 + f_i \frac{\kappa_i}{\kappa_{i+1}}\right) \exp(\kappa_i d_i) \end{bmatrix}. \tag{3.3}$$

where $i = 0, 1, \cdots, M-1$ and M is number of layers. The parameter f_i depends on the polarization; $f_i = 1$ for TE and $f_i = n_{i+1}^2 / n_i^2$ for TM polarization. Transmission and reflection can be obtained directly from the matrix Q as stated below.

$$R = \frac{Q_{21}}{Q_{22}}, \tag{3.4}$$

$$T = \frac{1}{Q_{22}} \tag{3.5}$$

Because Q_{22} appears in the denominator of both R and T, one can find its zeros to extract the modes of the multilayer structure [62]. However this zero finding can be challenging, thus a better alternative is to use the phase ϕ_{RPM} of $Q_{22} = |Q_{22}| \exp(j\phi_{RPM})$. This approach to exctract the modes of the multilayer is called the reflection pole method (RPM) [61]. For lossless modes and at single wavelength, ϕ_{RPM} changes its value abruptly by π for each guided mode propagation constant β. For lossy modes, the phase changes at the real part of the propagation constant, $\Re\{\beta\}$, but the phase change at this location is not exactly equal to π. This is because introduction of loss spreads the resonance and subsequently the phase shift of π over a range of propagation constants around $\Re\{\beta\}$. The half width at half maximum (HWHM) of this resonance is equal to the imaginary part of the propagation constant, $\Im\{\beta\}$. One can thus use $d\phi_{RPM}/d\beta$ as a measure to detect guided modes. Examples of mode extraction are given in chapter 5.

3.2 Two-dimensional structures: Rigorous Coupled Wave Analysis

3.2.1 One-dimensional gratings: in-plane incidence

Let us assume a “one-dimensional (1D) grating"[1] with period Λ which is illuminated “in-plane"[2] by a plane-wave at wavelength λ under an angle θ. Fig. 2.1b shows the geometry under investigation. Since the angle varies only perpendicular to the incidence plane, it is enough to consider only one parameter (θ) to define the angle.

For oblique incidence, a secondary parameter would be needed to take into account the other degree of freedom for the change of the incidence angle. This is the least difference between the case of in-plane and oblique incidence of light over 1D gratings. There are more fundamental differences also. For example, for in-plane incidence, one can distinguish two distinct polarizations; transverse electric (TE) and transverse magnetic (TM). In TE polarization, the electric field is parallel to the grating grooves (geometrical invariance direction) and in TM polarization, the magnetic field is parallel to the grating grooves. Unfortunately the definition of these two polarizations is frequently confusing because of various definitions in the literature. For TE polarization, one may find other abbreviations such as “P” or “s” polarization. Similarly, for TM, “S” or “p” are used sometime. The small letters “s” and “p” are used in Fresnel’s notation and the capital letters “S” and “P” are usually used in the context of gratings. Even the definition of TE and TM is sometimes mixed. This, however, should put no confusion in this manuscript because we defined the two polarizations. As in the case of planar structures, the time dependence of $\exp(j\omega t)$ is assumed here.

Thanks to periodicity of the cell along x direction, we can express the permittivity (which was defined in Eq. 2.4) in the form of a Fourier series.

$$\epsilon(x,z) = \sum_{i=-\infty}^{+\infty} \epsilon_i \exp\left(-j\,i K_x x\right) \tag{3.6}$$

where $K_x = 2\pi/\Lambda$. This Fourier representation has an important physical meaning. Let us consider the whole periodic structure as an optical system and the incident electromagnetic waves as the input of this system as depicted in Fig. 3.1. Output of the system can be defined by knowing its transfer function and the incidence wave spectrum. The transfer function can hold the spatial harmonics of the incident field uncoupled or it can couple them together depending on the nature of the transfer operator. It appears that the operator which acts on the incident electromagnetic field couples the field spatial harmonic and has a nature similar to a convolution. The coupling is done by using the Fourier components of the periodic structure. The transfer operator of the structure shifts the spatial harmonics of the incident field by multiples of K_x. We now explain this idea in more detail.

[1] defined in section2.1
[2] defined in section2.1

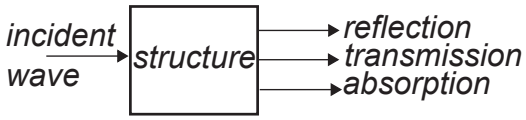

Figure 3.1: The solar cell as an optical system.

TE polarization

Let us consider the 1D grating geometry of Fig. 2.1b. The coordinates are shown on the figure to help understanding the formulation. According to the Floquet-Bloch theorem [63], the parallel field components can be expressed as

$$E_y(x,z) = \sum_{i=-\infty}^{+\infty} E_y^i \exp\left(-jk_x^i x\right) \tag{3.7}$$

$$h_x(x,z) = \sum_{i=-\infty}^{+\infty} h_x^i \exp\left(-jk_x^i x\right) \tag{3.8}$$

where h_x is the x component of the normalized magnetic field $\mathbf{h} = \mathbf{H}\sqrt{\mu_0/\epsilon_0}$ and ϵ_0 and μ_0 are permittivity and permeability of vacuum respectively. Here only parallel components of the field are considered because they are enough to solve Maxwell equations in the geometry under investigation. The x component of the wave-vector is obtained by $k_x^0 = n_0 k_0 \sin(\theta)$. Then one can find k_x^i by

$$k_x^i = k_x^0 + iK_x \tag{3.9}$$

From Maxwell's equations we have

$$\partial_z E_y(z) = jk_0 h_x(z) \tag{3.10}$$

Also, by partial derivation of the latter equation with respect to z and replacing it in Helmholtz equation

$$(\partial_x^2 + \partial_z^2) E_y(z) + \epsilon k_0^2 E_y(z) = 0 \tag{3.11}$$

we obtain

$$\partial_z h_x(z) = \left[j\epsilon k_0 - \frac{jk_x^2}{k_0} \right] E_y(z) \tag{3.12}$$

From these two equations, one can link the E_y and h_x by Maxwell equations and by Floquet expansion of the fields, it is possible to come up with a system of equations as

$$\frac{d\mathbf{U}(z)}{dz} = [\mathbf{M}]\mathbf{U}(z) \tag{3.13}$$

in which

$$\mathbf{U}(z) = \begin{bmatrix} \vdots \\ E_y^i \\ \vdots \\ h_x^i \\ \vdots \end{bmatrix} \tag{3.14}$$

In equation 3.13, $[\mathbf{M}]$ is an $2N \times 2N$ matrix (N is the number of terms in the expansion of each field component) which can be expressed as

$$[\mathbf{M}] = j \begin{bmatrix} \mathbf{0} & k_0 [\mathbf{I}_N] \\ k_0 \left([\epsilon] - \frac{k_x^2}{k_0^2} \right) & \mathbf{0} \end{bmatrix} \tag{3.15}$$

where $[\mathbf{I}_N]$ is an $N \times N$ identity matrix, $[\epsilon]$ is a Toeplitz matrix [64] including Fourier coefficients of permittivity and k_x is a diagonal matrix with diagonal elements of k_x^i. The convolution-like behavior of this optical system is already observable in the formulation. The permittivity appears as a Toeplitz matrix and not a diagonal matrix, which is the characteristic of operators which shift harmonics. Matrix $[\mathbf{M}]$ can be diagonalized and thus be written in the form $[\mathbf{M}] = [\mathbf{P}]\,[\mathbf{D}]\,[\mathbf{P}]^{-1}$ where $[\mathbf{P}]$ and $[\mathbf{D}]$ stand for the matrices of eigenvectors and eigenvalues of $[\mathbf{M}]$. It is easy to show that $\mathbf{U} = [\mathbf{P}(z_1)] \exp -(z_2 - z_1)\,[\mathbf{D}]\,[\mathbf{P}(z_2)]^{-1}$ (Ref. [65]).

In the reflection region, the field components E_y and h_x are described as

$$E_y(x,z) = \sum_{i=-\infty}^{\infty} \left[f_F^i \exp(-jk_{Fz}^i z) + b_F^i \exp(+jk_{Fz}^i z) \right] \exp(-jk_{Fz}^i z) \tag{3.16}$$

$$h_x(x,z) = \frac{-1}{k_0} \sum_{i=-\infty}^{\infty} k_{Fz}^i \left[f_F^i \exp(-jk_{Fz}^i z) - b_F^i \exp(+jk_{Fz}^i z) \right] \exp(-jk_{Fz}^i z) \tag{3.17}$$

Here $k_{Fz}^i = \sqrt{\epsilon k_0^2 - \left(k_x^i\right)^2}$, n_F is the incident medium refractive index and f_F^i and b_F^i are the coefficients of forward (incident) and backward (reflected) waves. At the top boundary of the

structure, electromagnetic boundary conditions apply which mean continuity of tangential field components, i.e. E_y and h_x. Then, one should use an appropriate propagation algorithm to obtain the forward and backward coefficients along the interfaces of each layer of the structure according to Eq. 3.13. An important point about applying the boundary conditions is that using transfer matrix formulation can cause instabilities in obtaining the expansion coefficients. The reason is that numerical noise can increase exponentially as it propagates along a layer. Thus, it is necessary to apply the boundary conditions such that this exponential growth is avoided. This can be done by forming a large sparse matrix [52] or by using a recursive method [65, 66].

After obtaining the parallel field components, h_z can be obtained by via $h_z = (k_x/k_0)E_y$.

TM polarization

TM polarization has a fundamental difference from TE; it includes field discontinuities. Since the method is based on Fourier expansion, convergence of the method for TM polarization is not as good as for TE due to the Gibbs phenomenon [51] and a higher number of orders is required to achieve convergence. A remarkable improvement in the convergence of the method was achieved by Morris and Lalanne [67] and by Li [51]. In their formulation, whenever the expression ϵE_x appeared, they used the expansion of the inverse of the $\eta = \epsilon^{-1}$ instead of ϵ, i.e. they used the Toeplitz matrix $[\eta]^{-1}$ instead of $[\epsilon]$. Another major progress was achieved by Morf when he expanded the field in each continuous part of each layer into Legendre polynomials and then applied the boundary conditions between the different parts of each layer and between the different layers [52]. This latter approach leads to the exponential convergence of the eigenvalues and eigenvectors of Helmholtz equation for each stack, which can be a significant improvement compared to the conventional RCWA. The drawback of polynomial expansion method is that its extension to two-dimensional gratings is not trivial and specially for random textures, its efficient implementation can be complicated. Another method to improve convergence in TM polarization is to change the coordinates such that resolution is increased close to the interfaces, where the field is discontinuous. This method, which is commonly called adaptive spatial resolution (ASR) solves the problem of convergence elegantly for both 1D and 2D gratings but its application is limited to only one layer unfortunately [53]. The ASR method has been applied to a low number of layers [68] but then it can become unstable. Recently the method has been stabilized [69] by application of the boundary conditions in the mapped coordinates but again the application is limited to only one layer. Later in section 3.2.4 we come back to this problem and we mention two ways to overcome this problem.

The conventional RCWA can be formulated for TM polarized light similar to the case of TE polarization. Based on Maxwell equations, $\partial_z h_x(z) = -j k_0 \eta^{-1} E_y(z)$ and Helmhotz equation $(\partial_x^2 + \partial_z^2) h_y(z) + \epsilon k_0^2 h_y(z) = 0$, the components of the field which are parallel to the grating plane can be linked to each other in the same form as Eq. 3.13 where [**U**] and [**M**] are defined

as

$$\mathbf{U}(z) = \begin{bmatrix} \vdots \\ h_y^i \\ \vdots \\ \vdots \\ E_y^i \\ \vdots \end{bmatrix} \tag{3.18}$$

$$[\mathbf{M}] = -j \begin{bmatrix} \mathbf{0} & k_0 \left[\eta\right]^{-1} \\ k_0 \left([\mathbf{I}_N] - \frac{1}{k_0^2} k_x \left[\epsilon\right]^{-1} k_x \right) & \mathbf{0} \end{bmatrix} \tag{3.19}$$

The rest of the process of obtaining the fields is similar to the procedure mentioned for TE polarization. After obtaining the parallel field components, E_z can be obtained via $E_z = \eta(k_x/k_0)h_y$ where $\eta = \epsilon^{-1}$.

Second order RCWA

The RCWA method up to here was based on a first order differential equation (Eq. 3.13). It is possible to merge the system of Eq. 3.13 into a second order system.

$$\begin{cases} \frac{d^2\mathbf{U}(z)}{dz^2} + k_0^2 \left([\epsilon] - \frac{k_x^2}{k_0^2} \right) \mathbf{U}(z) = 0 & (TE) \\ \frac{d^2\mathbf{U}(z)}{dz^2} + k_0^2 \left[\eta\right]^{-1} \left([\mathbf{I}_N] - \frac{1}{k_0^2} k_x \left[\epsilon\right]^{-1} k_x \right) \mathbf{U}(z) = 0 & (TM) \end{cases} \tag{3.20}$$

The advantage of these sets of equations is that they have half of the size of the previous first order systems. This helps in achieving faster convergence and thus higher accuracy.

Calculation of diffraction efficiency

Thanks to the modal nature of the RCWA method, it is possible to find the diffraction efficiency of individual orders very easily. Diffraction efficiency is defined as the amount of power carried by an individual order. If the system is lossless, energy conservation necessitates that the sum of the energy in the reflection and transmission is equal to the incident energy. This means that for any surface A around the structure, the following equation should

hold.

$$\int_A \vec{\mathbf{S}} . \vec{\mathbf{n}} \, dA = 0. \tag{3.21}$$

where $\vec{\mathbf{S}}$ is the Poynting vector and $\vec{\mathbf{n}}$ is the surface normal. Assume that there is a metallic back-reflector underneath the structure, therefore there is no transmission. Also consider a surface parallel to the grating plane at a certain distance on top of the structure. The electric and magnetic fields of a plane wave propagating in a homogeneous medium can be linked via the impedance of the medium, $\mathbf{H} = (1/\eta_{medium})\mathbf{k} \times \mathbf{E}$, therefore, the expression $\mathbf{E} \times \mathbf{H}^*$ simplifies to $|\mathbf{E}|^*$ or $|\mathbf{H}|^*$. Hence, based on Eq. 3.21 one can write

$$P_{in} = \sum_i \left| b_F^i \right|^2 \cos \psi_i \tag{3.22}$$

where P_{in} is the incident power, i is the order index and ψ_i is the angle between the propagation direction of the i-th order and surface normal, which is $-z$ direction in this case. The term in the summation expresses the power carried by the i-th order and it is called the diffraction efficiency of the order.

Absorption calculation

To calculate absorption, it is necessary to find the coefficients of the forward and the backward waves for each slice. It is then possible to find the field profile over each slice and thus over the whole structure. Then, absorption can be found by using the slowly varying approximation $A = \frac{\omega}{2} \epsilon_i \int |\mathbf{E}|^2 \, dV$.

3.2.2 One-dimensional gratings: conical diffraction

For conical diffraction, it is no longer possible to decouple the two polarizations. Here we go over a simple formulation for this case. Maxwell equation $\nabla \times \mathbf{E} = -\partial_t \mathbf{B}$ can be expanded in the form

$$\partial_y E_z - \partial_z E_y = -j\omega\mu H_x \tag{3.23}$$
$$\partial_z E_x - \partial_x E_z = -j\omega\mu H_y \tag{3.24}$$
$$\partial_x E_y - \partial_y E_x = -j\omega\mu H_z \tag{3.25}$$

Similarly the equation $\nabla \times \mathbf{H} = \partial_t \mathbf{D}$ can be written in the form

$$\partial_y H_z - \partial_z H_y = j\omega\epsilon E_x \tag{3.26}$$
$$\partial_z H_x - \partial_x H_z = j\omega\epsilon E_y \tag{3.27}$$
$$\partial_x H_y - \partial_y H_x = j\omega\epsilon E_z \tag{3.28}$$

Thanks to periodicity of the structure along x direction we can expand the fields into a Bloch-Floquet series. This means expanding the field using basis functions of the form $\exp(-j\alpha_n x)$. This in turn shows that derivation with respect to x can be accounted for by multiplication by $-j\alpha_n$. Similarly the z-dependence of the field can be described as $\partial_y = -jk_y$. The second Maxwell equation can be then rewritten as

$$\begin{bmatrix} \partial_z H_x - \partial_x H_z \\ \partial_x H_y - \partial_y H_x \\ \partial_y H_z - \partial_z H_y \end{bmatrix} = jk_0 \begin{bmatrix} [\eta]^{-1} & \mathbf{0} & \mathbf{0} \\ \mathbf{0} & [\epsilon] & \mathbf{0} \\ \mathbf{0} & \mathbf{0} & [\eta]^{-1} \end{bmatrix} \begin{bmatrix} E_y \\ E_z \\ E_x \end{bmatrix} \tag{3.29}$$

where $[\epsilon]$ and $[\eta]$ are Toeplitz matrices of the Fourier coefficients of ϵ and ϵ^{-1}. A similar set of equations can be formed for the other Maxwell equation which includes permeability μ. By assuming the z-dependence of the form $\exp(-j\chi z)$ one can further simplify the latter set of equations and end up in a system which includes only the y and the x field components.

$$\begin{bmatrix} E_x \\ H_x \\ H_y \\ E_y \end{bmatrix} = -\chi \begin{bmatrix} \mathbf{0} & \frac{\gamma}{k_0}[\epsilon]^{-1}\alpha & \mu - \frac{\gamma^2}{k_0}[\epsilon]^{-1} & \mathbf{0} \\ -\frac{\alpha\gamma}{k_0\mu} & \mathbf{0} & \mathbf{0} & \frac{\gamma^2}{k_0\mu} - k_0[\eta]^{-1} \\ -\frac{\alpha^2}{k_0\mu} + k_0[\eta]^{-1} & \mathbf{0} & \mathbf{0} & \frac{\alpha\gamma}{k_0\mu} \\ \mathbf{0} & \frac{1}{k_0}\alpha[\epsilon]^{-1}\alpha & -\frac{\gamma}{k_0}\alpha[\epsilon]^{-1} & \mathbf{0} \end{bmatrix} \begin{bmatrix} E_x \\ H_x \\ H_y \\ E_y \end{bmatrix} \tag{3.30}$$

Finally the electromagnetic field in the grating region can be expressed as

$$\begin{bmatrix} E_x \\ H_x \\ H_y \\ E_y \end{bmatrix} = \sum_{nq} \exp(-j\alpha_n) \begin{bmatrix} E_x^+ & E_x^- \\ H_x^+ & H_x^- \\ H_y^+ & H_y^- \\ E_y^+ & E_y^- \end{bmatrix} \begin{bmatrix} \exp\left(j\chi_q^+ z\right) & \mathbf{0} \\ \mathbf{0} & \exp\left(j\chi_q^- z\right) \end{bmatrix} \begin{bmatrix} \mathbf{u}_q \\ \mathbf{d}_q \end{bmatrix} \tag{3.31}$$

Here $\mathbf{u}_q$ and $\mathbf{d}_q$ are coefficients to be found by a stable algorithm which can be recursive such as the S-matrix algorithm [66] or non-recursive [52]. Now we briefly go over the idea of the scattering matrix algorithm.

3.2.3 S-matrix algorithm

The scattering matrix algorithm, which is often abbreviated as the S-matrix algorithm, links the forward and the backward wave amplitudes in the incident medium and at the interfaces of the p-th layer.

$$\begin{bmatrix} A^{(p+1)} \\ B^{(0)} \end{bmatrix} = S^{(p)} \begin{bmatrix} A^{(0)} \\ B^{(p+1)} \end{bmatrix} \tag{3.32}$$

where A and B are forward and backward waves respectively. In the last layer of the structure there is no backward wave, i.e. $B^{(M+1)} = \mathbf{0}$ (M is the number of layers). Also in the incident medium the forward wave $A^{(0)}$ is known. Hence, even from its definition, it is clear that the scattering matrix can provide both reflection and transmission data.

In addition to its abstract mathematical meaning, the scattering matrix does have a physical interpretation. In Fig. 3.2 the Transfer matrix and the scattering matrix are compared schematically. The solid arrows show the input waves and the dashed arrows are the output waves for each algorithm. In the transfer matrix the input data are the forward and backward waves on one side of the system (for example one layer or the whole stack of layers) and the output is the forward and the backward waves on its other side. The scattering matrix accepts the forward wave of the incident medium and the backward wave of the transmission medium and gives the backward wave of the incident medium and the forward wave of the transmission medium as the output. In this way, the scattering matrix gives a more natural way of representing an optical system with incident waves as input and reflection and transmission as the output. The result of this natural behavior is stability of the scattering matrix formulation compared to the transfer matrix formulation. The main reason is that the formulation of the transfer matrix includes growing exponentials but the scattering matrix does not contain such terms.

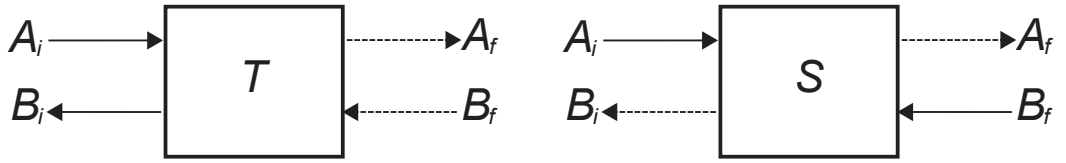

(a) (b)

Figure 3.2: Schematic demonstration of (a): transfer matrix, and (b):scattering matrix.

In Ref. [66] a method is developed to calculate the scattering matrix of the whole stack of layers recursively. The algorithim is usually called the S-matrix algorithm because it calculates the scattering matrix.

3.2.4 Adaptive spatial resolution

The RCWA method converges slowly for TM polarized illumination. The reason behind this slow convergence is discontinuity of the normal component of the electric field at the interface between two different media according to the Maxwell equation $\nabla \times \mathbf{H} = j\omega\epsilon\mathbf{E}$. Since RCWA uses Fourier expansion of the fields and the permittivity, this can be attributed to Gibbs phenomenon, which is a well-known mathematical problem. One way to resolve the problem is to express the permittivity in a new coordinate system u that is denser where the permittivity is discontinuous [3]. Here we mention the suggestion of Vallius for definition of the new coordinate system between the jump points $l-1$ and l.

$$x(u) = a_1 + a_2 u + \frac{a_3}{2\pi}\sin\left(2\pi\frac{u-u_{l-1}}{u_l-u_{l-1}}\right) \tag{3.33}$$

where x is the cartesian coordinates and the cofficients a_1, a_2 and a_3 are defined as

$$a_1 = \frac{u_l x_{l-1} - u_{l-1}x_l}{u_l - u_{l-1}} \tag{3.34}$$

$$a_2 = \frac{x_l - x_{l-1}}{u_l - u_{l-1}} \tag{3.35}$$

$$a_3 = G(u_l - u_{l-1}) - (x_l - x_{l-1}) \tag{3.36}$$

and G is a constant close to zero, for example 0.001. Fig. 3.3 shows the new coordinates assuming that the discontinuities occur at $x = 0, 0.1, 0.6$ and 0.65, and that $G = 0.001$. The thin lines show the positions of discontinuities in x.

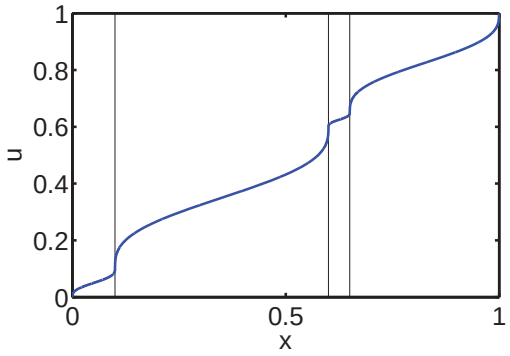

(a)

Figure 3.3: Mapping x to u for the adaptive spatial resolution. Discontinuities are assumed to occur at $x = 0, 0.1, 0.6$ and 0.65. For simplicity $u_l = x_l$

[3] We remind the reader that increasing the spatial resolution around the discontinuity is not the only method to improve convergence. Although the methods which apply the boundary conditions at the discontinuity (e.g. the finite element method or polynomial expansion method) seem more correct from a mathematic point of view, changing the spatial resolution may be considered an alternative that may be easier to program.

In TM polarization, H_y can be obtained by solving Eq. 3.20. The solution can be expressed as

$$H_y = \sum_q \left[A_q \exp(-j\chi_q z) + B_q \exp(j\chi_q z) \right] \sum_m H_{mq} \exp(-j k_{x,m} u) \tag{3.37}$$

Note that instead of using the basis functions $\exp(-j k_{x,m} x)$, we use new basis functions of the form $\exp(-j k_{x,m} u)$. It is necessary to adapt Helmhotz equation to the new coordinate. The only change to be applied is that the derivations with respect to x change to $d/dx = (du/dx) \cdot (d/du)$. By defining three auxiliary functions

$$f(u) = \frac{\partial x}{du} \tag{3.38}$$

$$a(u) = \epsilon(u) f(u) \tag{3.39}$$

$$b(u) = \frac{f(u)}{\epsilon(u)} = \eta(u) f(u) \tag{3.40}$$

we can write derivation with respect to x as $d/dx = (1/f) \cdot (d/du)$. Derivation with respect to x can be identified by the appearance of k_x in Eq. 3.20, which can be thus expressed as

$$\frac{d^2 \mathbf{U}(z)}{dz^2} + [\mathbf{b}]^{-1} \left(k_0^2 [\mathbf{f}] - k_x [\mathbf{a}]^{-1} k_x \right) \mathbf{U}(z) = 0 \tag{3.41}$$

where **f**, **a**, and **b** are Toeplitz matrices formed from the Fourier coefficients of the respective functions. To apply boundary conditions, Vallius *et al.* transform the fields back to a common basis, for example the Fourier domain of the original Cartesian coordinates. This enables them then to apply the method to a multilayer stack. This projection can be done by using a projection operator (matrix) **T** which is defined as

$$T_{pm} = \frac{1}{\Lambda} \int_0^{\Lambda} f(u) \exp\left[j \left(k_{x,p} x(u) - k_{x,p} u \right) \right] du \tag{3.42}$$

and multiplying the matrix of Fourier coefficients of any field component by it, for example $H_y^x = \mathbf{T} H_y^u$. The next step is applying boundary conditions which can be done for example using a recursive S-matrix method.

During application of the boundary conditions one can observe the instability of the adaptive spatial resolution. The reason is that during this process one needs to invert the matrix **T** which is usually ill-conditioned and its inversion introduces remarkable error into the results and consequently makes the method instable. This can be avoided for a single layer by application of the boundary conditions in u-coordinate. However, application of the method is limited for more than one layer.

3.2.5 How to use adaptive spatial resolution for stacked gratings?

Solving the eigenvalue problem is the main concern while using Fourier based methods. ASR can give eigenvalues and eigenmodes very accurately with significantly improved convergence. To use ASR for multilayers one should use a common coordinate for all of the layers. This technique is impractical when the number of layers is large and their profile is not similar. Coordinate transformation in Fourier domain before application of the boundary conditions causes instability problems because the transformation matrices become singular. One method is to consider a grid in the real space domain and first solve the eigenvalue problem using ASR, then evaluate the eigenmodes on the mesh in real space and finally apply the boundary conditions in real space using an algorithm such as S-matrix [66] or by simply solving for all boundaries in a large system [52].

3.3 Other methods and three-dimensional geometries

The finite Difference Time Domain (FDTD) method is a popular approach to solve Maxwell equations for arbitrary geometries. As its name suggests, it uses a time-marching algorithm. Contrary to many frequency-domain approaches, it does not include matrix inversion which adds to its stability. Thanks to its time domain nature, it can simulate structures over a very wide spectral range. Thanks to its simple algorithm, FDTD can provide a versatile tool for simulation of optical systems and various optical properties such as dispersion, nonlinearity, anisotropy, etc. Therefore, it may seem an appropriate tool for the simulation of solar cells [39, 70, 71]. A major advantage of FDTD is that it can find the response of a system over the whole desired band in one simulation. This can be done for example by shooting an incident temporal pulse which covers the desired frequency band into the structure. Another advantage of FDTD is that it does not need as high amount of memory as some full-numerical frequency-domain approaches such as the finite element method (FEM).

There are different criteria that are of critical importance while performing FDTD simulation of solar cells. First, numerical dispersion can modify the spectral response [72, 73, 74]. A solution to this problem is using an algorithm which considers higher orders [42]. Another way to reduce the numerical dispersion is to increase mesh resolution. For solar cells this seems to make the method very memory-hungry and also time-consuming. As a rule of thumb, to make reliable FDTD calculations, each wavelength of light should be equal to at least 10 grid points [42]. This means that for example at the wavelength of 300 nm, in a medium with refractive index of $n = 5$, maximal grid size is $300/5\times10 = 6nm$.

Another disadvantage of the FDTD method is that it takes long. The main criterion is the stability condition of the method which limits the time-step via the Courant stability condition [42]. In the 3D case, this criterion can be expressed as

$$v\Delta t \leq \frac{1}{\sqrt{(\Delta x)^2 + (\Delta y)^2 + (\Delta z)^2}} \tag{3.43}$$

In the above expression v is light speed in the medium and Δt is time-step. Δx, Δy and Δz denote the grid size along different Cartesian coordinates. Usually, $\Delta x = \Delta y = \Delta z$ and one gets

$$v\Delta t \leq \frac{1}{\sqrt{3}\Delta x} \tag{3.44}$$

Increasing resolution in each direction by a factor of N, increases the total number of grid points N^3 times and reduces the maximal step size by a factor of $1/N$. This increases memory usage by a factor of N^3 and simulation time by a factor of N^4.

Another concern about FDTD is that to simulate dispersive media, it should approximate the wavelength-dependent permittivity by a summation of poles that have a pre-defined form e.g. Lorentzian, Drude or Debye [42]. Application of this approximation has several disadvantages; first, it introduces a fitting error. Second, the method becomes slow by introducing poles. The more poles one introduces for a material, the slower the method becomes. Third, introducing dispersion can modify the stability condition of FDTD. This means that one may need smaller step-size to reach stability which slows down the already time-consuming FDTD method even more.

The finite element method (FEM) is another method used for the optical modelling of thin-film solar cells by different groups such as Zuse Institute [75], the group of M. Zeman in Delft [43, 76, 77], and the group of M. Topič in University of Ljubljana [78]. Usually the main bottleneck of the FEM is it needs a huge amount of memory. Altogether, it seems an appropriate method for the analysis of thin-film a-Si cells. However, its applicability to the μc-Si cells seems not possible with the current ordinary computational facility.

An alternative approach to the Fourier modal expansion of the fields can be modal expansion in real space. The benefit is that Gibbs phenomenon does not occur in real space and therefore the problem of poor convergence should not be encountered. Several approaches have been studied recently in this regards: Finite difference modal method [79], moment method [80] and point-matching pseudo-spectral modal method [81].

4 Optical limits for thin-film solar cells

In this chapter I[1] investigate the physical limits which are imposed by the optical properties of a solar cell on its efficiency and photocurrent. Efficiency of a solar cell is tightly entangled to its photo-generated current as already explained in section 1.4. The photocurrent is in turn a function of light absorption in the cell (Eq. 1.1). Enhancing absorption —which is also called light trapping—can thus improve the efficiency of a solar cell, and it is a main subject of study in this chapter. Specifically, I investigate the upper bound of absorption enhancement in thin film a-Si solar cells.

Section 4.1 reviews briefly different limits for absorption enhancement in thin films. Then, we consider an ideal thin film to study the angular behavior of the upper bound of absorption enhancement in section 4.2. Later, we extensively investigate this limit and its angular behavior in section 4.3 for a slab and a full solar cell stack. Absorption enhancement by guided modes is determined by both the number of guided-mode excitations and the coupling strength for each excitation. In section 4.4 we discuss two limitations on coupling strength. The first one is imposed by single pass absorption of the cell (4.4.1) and the second one is based on Planck's law of radiation (4.4.2) Then, in section 4.5 we mention some bounds for a cell's efficiency and we suggest ways to surpass them. This chapter of the thesis explains the results mentioned in three of my published papers [82, 83, 84].

4.1 Limits on photocurrent enhancement

In the literature, usually the "absorption enhancement factor", or simply the "enhancement factor" is used as a figure of merit to characterize the capability of a solar cell to absorb light. This factor is defined in the literature as

$$F = \frac{\text{maximal absorption in the absorber}}{\text{single pass absorption over the absorber thickness}} \tag{4.1}$$

[1] I have benefited from several of my publications (Refs. [82, 83, 84]) in this chapter, thus, the cooperation of all co-authors of the mentioned publications is appreciated.

Absorption enhancement is mainly required at the wavelengths where the solar cell is weakly absorbing. Weak absorption means that one can approximate the single pass absorption over the cell's thickness with the expression αd where α is the absorption coefficient of the absorber and d is its thickness.

Based on the above definition of the enhancement factor, different limits have been suggested to estimate the upper bound of absorption in a solar cell, which will be reviewed later in this section. It is important to know that all of these limits are based on a mode counting scheme explicitly or implicitly. Specifically guided modes have attracted special interest recently and they have been observed to improve a cell's photocurrent [36].

Guided modes of an optical system, for example a thin film multilayer, are solutions of Maxwell's equations in the system which ideally do not exchange energy with the outside environment. Because of this, these modes are sometimes called "trapped modes" [30]. Guided modes of a solar cell can be excited if the cell interfaces are changed from planar into textured. To excite a guided mode, both the"transverse resonance condition" and the"Bragg condition" should be satisfied.

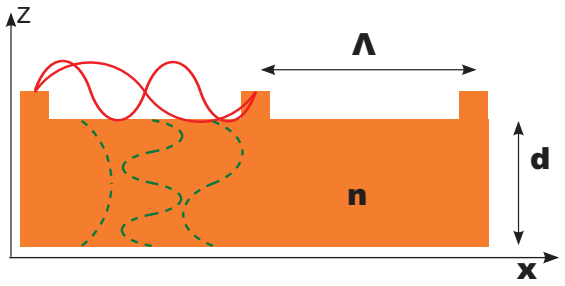

Figure 4.1: Schematics of a slab with a 1D periodic texture. The field phase variations are symbolically shown with sinusoidal patterns. The dashed and the solid curves correspond to the cases where transverse resonance condition and the Bragg condition are satisfied respectively.

Fig. 4.1 shows schematically a dielectric film textured using a 1D grating. The transverse resonance condition means that the wave makes constructive interferences along the thickness of the film. Approximately, this is equivalent to the condition that the resonances are solutions of the transcendental equation of the film; i.e. they are phase-matched to the guided modes of the film. I say approximately because modification a planar geometry deviates its modes from the dispersion of a planar device. In Fig. 4.1 the sinusoidal curves represent symbolically change of the wave phase along the longitudinal and the transverse directions. The dashed curves correspond to the cases where the phase change in one round trip along the film thickness is a multiplicand of 2π i.e. where the transverse resonance condition is satisfied.

Satisfaction of the Bragg condition couples the modes inside the multilayer stack to the continuum of radiation modes outside the device. For a 1D grating and at normal incidence this

means that

$$k_{\parallel} = 2m'\pi/\Lambda \tag{4.2}$$

where $k_{\parallel}$ is the guided-mode propagation constant m' is an integer and Λ is the grating period. The red solid curves in Fig. 4.1 demonstrate schematically when the Bragg condition is satisfied.

The two mentioned conditions imply the existence of a discrete spectrum of the distribution of the wave-vectors and the wavelengths corresponding to guided modes. In other words, the guided modes in the dispersion diagram do not form a continuum. If the guided-wave structure thickness (d) or the grating period (Λ) is much larger than the incident wavelength (λ), the guided modes get so close to each other in the dispersion diagram that they may be regarded as a continuum. The two continuum approximations of $\Lambda \gg \lambda$ (continuity in $k-$space) or $d \gg \lambda$ (continuity in k-space) have been used by different authors to find the limit of absorption enhancement in solar cells [29, 31, 30, 20].

One of the first calculations of the absorption enhancement limit dates back to 1982 when Yablonovitch *et al.* suggested the limit of $4n^2$ for the enhancement factor where n is the refractive index of the absorber. [29]. They assumed scattering full-randomization at the cell's interfaces which is equivalent to continuity in $k-$space. Apart from this, Yablonovitch *et al.* have considered two further assumptions: weak absorption of light —which is a common convention between all of the limits of absorption enhancement discussed in this thesis—and large thickness of the absorber. The first condition is logical because it is desired to increase absorption mainly when the cell does not absorb light well. The second assumption starts to be true if the cell is thicker than a few wavelengths and it means that a large number of modes are present in the absorber such that one can use the wavelength continuum approximation. To find more practical values, Deckman *et al.* extended the limit by inclusion of loss in other layers of the cell [31]. Their method to find the upper bound of absorption enhancement motivated other researchers to further extend their approach [85, 86, 87]. For thinner films, Stuart and Hall have found the limit to be smaller than $4n^2$ [30]. In their calculations, they have considered thin films which are randomly textured, thus, again they have assumed Lambertian scattering in their calculations (continuity in wavelength). The decrease of the enhancement factor in their calculations is because they included the imperfect confinement of the modes to the solar cell. This effect also exist in thick cells but it has not been considered in the corresponding calculations [29, 20].

The assumption of Lambertian light scattering is common between all of the mentioned upper bounds, at least partly. I say partly because in Ref. [85] the authors have considered Lambertian scattering after two bounces inside the film. A Lambertian scatterer is a scatterer whose scattering is uniform over the whole angular range. Fig. 4.2 shows the scattering pattern of a Lambertian scatterer in thick blue.

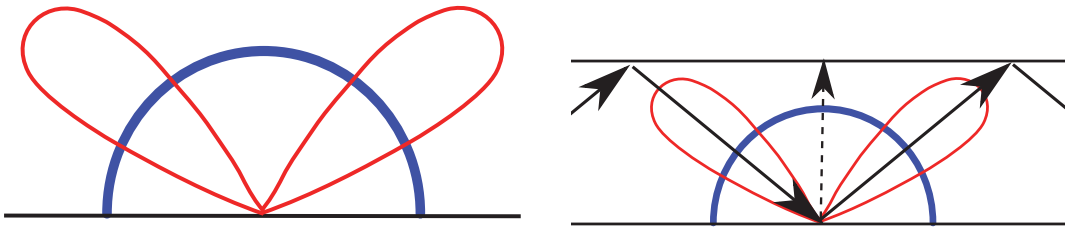

(a) (b)

Figure 4.2: (a): Radiance (see Appendix A for definition) of a Lambertian scatterer (thick blue) and a second scatterer which scatters light directionally. (b): Same as (a) including the guided modes directions of the thin film structure.

An important question is whether the assumption of Lambertian scattering is valid for real solar cells. A second question is whether the upper bound of absorption necessarily corresponds to a Lambertian scatterer. For example, does Lambertian scattering (blue thick curve in Fig. 4.2a) result in better light absorption compared to directional scattering (red thin pattern in Fig. 4.2a).

The first question seems to be not hard to respond. Based on the agreement between the experimental data and the upper limits which assume Lambertian scattering of interfaces, it appears that this assumption is not far from reality [35, 34]. The assumption of angular insensitivity of interfaces -let us call it perfect randomness- is further justified if we note the different factors that try to randomize light absorption in the cell. First, the light illumination angle is not completely fixed and the incident light does not prefer a specific polarization. Then, at each interface of the cell, direction randomization occurs. The whole travel of light inside the cell can be imagined as a sequence of up and down bounces between different interfaces. Furthermore, the cell is a very wide-band device and this reduces sensitivity of the device to a specific resonance or direction. To date, the best fabricated cells are based on random textures and because of the rich spectral response of these textures, perfect randomization assumption seems not very far from reality.

Contrarily to the first question, the second one seems to be very hard to respond, if possible at all. It is true that our state-of-the-art cells are based on random textures but this is not enough to conclude that light randomization can maximize light absorption in the cell. Planck's law of radiation guarantees that the sum of coupling strength over different angles/frequencies is fixed [88]. At least for thin films this seem to have an impact. Fig. 4.2b shows schematically guiding of a mode in a thin film. Assume that light is coupled into the film from the bottom interface which may have two different scattering patterns: Lambertian (thick) and the symmetric pattern with two lobes (thin). Light coupling into the film can happen in the form of an interference or excitation of guided modes. Interference occurs mainly as a function of film thickness. Guided-mode excitation, contrarily, happens if the lobes of radiance of the interfaces meets the direction of guided modes inside the film. This is shown in Fig.4.2b by arrows. A Lambertian scatterer does not distinguish direction. Therefore, it sends light in

the direction that it couples to the guided mode (solid arrows) similarly to other directions which do not result in effective coupling (dashed arrow). The directional scatterer, inversely, can couple light to the guided mode, if its direction matches the one of the guided mode. Otherwise, it may lose the guided-mode direction and be unable to excite it.

4.1.1 The $4n^2$ limit

Yablonovitch and Cody assumed Lambertian scattering interfaces to find this limit. They claimed that in a medium of refractive index n, intensity and absorption can be enhanced by respective factors of $2n^2$ and $4n^2$. They present two types of formulation in their paper [29] to find this limit; one approach based on statistical mechanics and a second method based on detailed balance. Here we briefly reproduce the former.

The energy density U of a black-body at temperature T can be described by Planck's formula [89]

$$U = \frac{\hbar\omega}{\exp\{\hbar\omega/kT\}-1}\frac{d\Omega k^2 dk}{(2\pi)^3} \tag{4.3}$$

where $k = n\omega/c$, ω is the angular frequency, c is speed of light, Ω is solid angle, n is the refractive index and $\hbar$ represents the reduced Planck's constant. Intensity impinging on a surface can be obtained by multiplication of U with the group velocity $v_g = d\omega/dk$

$$I = Uv_g = n^2 I_0 \tag{4.4}$$

where I_0 represents light intensity in air. Considering reflection from the back-side makes a factor of 2 for the intensity enhancement. Absorption enhancement can be obtained by integrating the light path prolongation inside the cell by Lambertian scattering. The effect of scattering angle θ of light at the interfaces appears as a $\sin\theta$ term in the corresponding integral, which after being integrated brings another factor of 2, thus results finally in the $4n^2$ factor (Eq. 9 in Ref. [29]).

Evidently in the mentioned approach no effect of incident angle is present. If the effect of the incident angle is considered, higher upper bounds can be obtained for the absorption limit [20, 82].

4.1.2 The $4\pi n^2$ and the $8\pi n^2/\sqrt{3}$ limit

Recently Yu *et al.* have shown that by using periodic patterns, it is possible to go over the $4n^2$ limit for absorption enhancement. By using grating patterns, Yu *et al.* relaxed the continuum

approximation in k-space[2]. They obtain the upper bound of absorption enhancement by using temporal coupled-mode theory. Because they consider the case where there are many modes in the structure, they call their method "the statistical coupled-mode theory". [3] Here we briefly go over their method.

Temporal evolution of a single resonance satisfies the following approximation [18, 20].

$$\frac{da}{dt} = \left(j\omega_0 - \frac{N\gamma_e + \gamma_i}{2} \right) a + j\sqrt{\gamma_e} S \tag{4.5}$$

In this equation γ_e is the external coupling rate and γ_i is the internal loss rate. N in the number of output ports and it is assumed that all the output ports have the same output characteristic. For a solar cell based on gratings, each diffraction order is equivalent to one output port, thus N is equal to the number of reflected and transmitted diffraction orders. The term with square root shows coupling to a source with an amplitude of S. The resonance angular frequency is represented by ω_0.

Here we present a brief heuristic justification of Eq. 4.5 [4]. Assume a mode with amplitude a in a resonator, which is isolated from its ambient. If the resonator is lossless, the mode will remain in it forever and its energy will be preserved. Assuming so, in the harmonic regime, the mode amplitude is expected to be of the form

$$a(t) = A_0 \exp(j\omega_0 t) \tag{4.6}$$

which is a solution of Eq. 4.5 for $\gamma_i = \gamma_e = 0$. If the resonator is not perfectly lossless, the mode amplitude will damp with at a rate equal to $\gamma_i/2$. Damping of the mode amplitude can also occur due to coupling of the mode to the external ambient. If the mode is not completely decoupled from outside, its energy can be transferred through an output port at a rate equal to $\gamma_e/2$. If there are N equivalent output ports, energy of the mode can be transferred N times faster to the outside; thus the overall external coupling rate will be equal to $N\gamma_e/2$. The overall damping rate of the wave amplitude is thus equal to $(N\gamma_e + \gamma_i)/2$ which is mentioned inside the parentheses in Eq. 4.5, and it can be considered as the imaginary part of ω_0. This is consistent with the exponential dependence of the wave amplitude a on ω_0 in Eq. 4.6 because the imaginary part of ω_0 leads to damping of the exponential function. If there is an external radiation source, due to reciprocity its radiation can couple to the mode inside the resonator in the same way that the mode energy couples out. In many cases the external source S is coupled to the resonant mode through one input port. For example in a solar cell,

[2] which was discussed in section 4.1.

[3] Coupled-mode theory has been extensively used as an approximation to solve optical problems which include resonant optical structures [90, 91, 92, 93, 94, 95]. It has been developed extensively by Haus a few decades ago [18, 41, 96]. Other authors have extended the coupled-mode theory and used it for the analysis of different structures [97, 98, 99, 100, 101, 102, 103, 104, 105, 106].

[4] For a more detailed derivation, the interested reader is referred to chapter 7 of Ref. [18].

at each moment sun illuminates the cell at a certain angle, which corresponds to the zero-th diffraction order [5]. The last term in Eq. 4.5 accounts for coupling of mode energy to this source [6].

One should note that the coupled-mode formula mentioned in Eq. 4.5 is an approximation in many respects and by no means can replace an exact solution of Maxwell's equations for solar cells. First of all it is a slowly varying approximation, which mean that when the dispersive effects become remarkable, it can get inaccurate (c.f. section 2.5.2). We will come back to this point later in section 4.2. Besides, the coupled-mode theory is a perturbation approach. This means that for small deviations from the reference geometry —which is planar in this case —it can predict many optical effects relatively accurately but as the deviation from the reference becomes strong, the method gets inaccurate. Generally, such a method is not appropriate to deal with strong interactions. For instance, if the material is highly absorbing, the coupled-mode theory becomes inaccurate. More specifically, the coupled-mode theory results in a Lorentzian resonance shape as will be shown later (Eq. 4.9), which is not always the case in practice, especially when the absorber material is strongly absorptive. Also, when several resonance are very close to each other in frequency domain, their shape can be deviated from exact Lorentzian and the final spectrum may include broadened resonances or very sharp ones. Another approximation is that near field effects may be neglected in the coupled-mode formulation. Despite the mentioned points, the coupled-mode theory is used in literature to provide an approximation of the optical limits of light absorption enhancement in solar cells [20]. Since absorption enhancement is mainly desired where the materials are weakly absorbing, the application of the coupled-mode theory seems reasonable to find the upper bounds of absorption enhancement in relevant structures.

In the harmonic regime, we can replace time derivation with $j\omega$ and rewrite Eq. 4.5 as

$$a = \frac{j\sqrt{\gamma_e}S}{\left[j\left(\omega-\omega_0\right)+\frac{(N\gamma_e+\gamma_i)}{2}\right]} \tag{4.7}$$

By using Eq. 4.7 and noting that [18, 20]

$$A = \frac{\gamma_i\,|a|^2}{|S|^2} \tag{4.8}$$

[5] We neglect the spatial incoherence of solar illuminaiton on the cell.

[6] The reader may question the appearance of γ_e inside the square root in Eq. 4.5. It is beyond the scope of this thesis to perform the corresponding calculations; however, the interested reader is strongly recommended to study chapter 7 of Ref. [18], and more specifically the part which includes Eq. (7.27). In brief, this comes from reciprocity and time reversal of electromagnetic fields and a main assumption in this calculation is that the media should be weakly absorbing. Note that the dimension of a and S is different: $|a|^2$ represents mode energy but $|S|^2$ stands for incident power.

one obtains the following expression for absorption

$$A(\omega) = \frac{\gamma_i \gamma_e}{(\omega - \omega_0)^2 + \left(\frac{\gamma_i + N\gamma_e}{2}\right)^2} \tag{4.9}$$

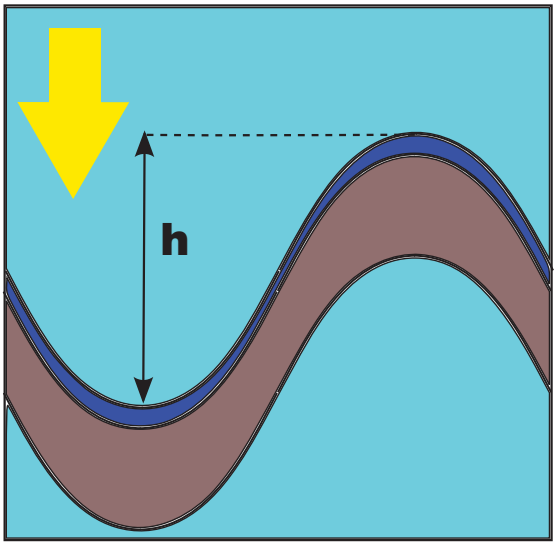

Figure 4.3: Schematics of the considered Si film (blue) on Ag back-reflector (gray). The grating depth h is varied to change coupling.

To provide a feeling of the values that the coefficients γ_e and γ_i can take, we consider a 30 nm thick Si slab on top of a 200 nm-thick silver back-reflector. The Si layer is considered very thin to avoid coexistence of multiple guided modes and thus to simplify the analysis. The materials are "idealized": their permittivity is considered $\epsilon_{Si} = 13 + 0.01i$ and $\epsilon_{Ag} = -35$. The metal is used here as a lossless back-reflector, thus the imaginary part of its permittivity is zero. The Si layer is weakly absorbing to resemble an a-Si layer in the low-absorption long-wavelength regime. Since the structure is planar, the guided modes are not excited, because $\gamma_e = 0$. However, perturbing the planar geometry results in coupling the external radiation to guided modes of the device. Our aim is to have an estimate of the values that γ_e and γ_i take. For this purpose, we assume that the back-reflector is deviated from planar into a sinusoidal pattern with the period of 500 nm. We change the grating peak to valley depth h and we find γ_e and γ_i for a certain guided-mode excitation for each h. The grating is shown in Fig. 4.3. TE polarization is considered for the simulations of this part which means that the the electric field is parallel to the grating grooves.

Fig. 4.4 shows the increase of absorption in the Si layer, compared to the planar case, for the grating depths (h) of 5, 10, 20, 50 and 100 nm in the wavelength range from 535 to 560 nm. For very small h, mode excitation is not strong and the Lorentzian peak takes very small values. As the grating becomes deeper, the resonance becomes wider, which is a result of

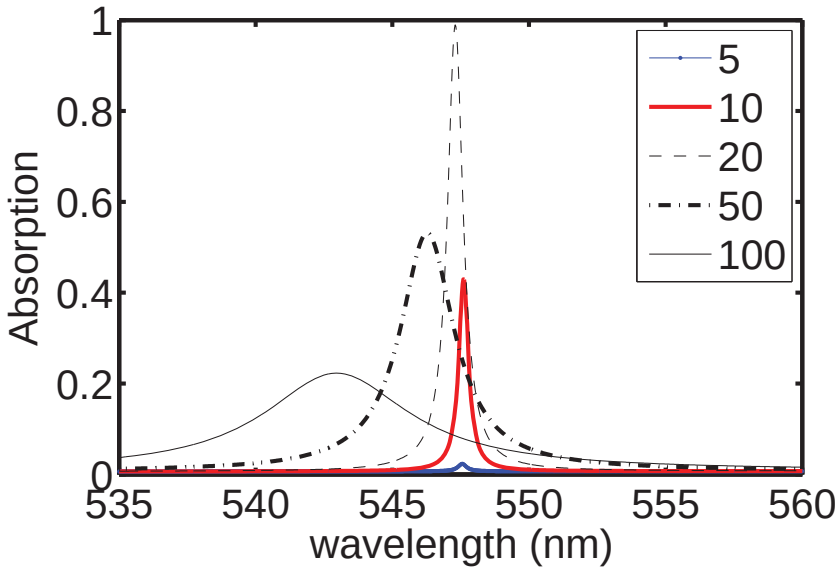

Figure 4.4: Spectrum of the increase of absorption (compared to the planar case) for the sinusoidal grating for different grating depths.

Table 4.1: external coupling rate (γ_e) and internal loss rate (γ_i)

h (nm)	γ_e ($\times 10^{13}$ rad/s)	γ_i ($\times 10^{13}$ rad/s)
2	0.0010	0.2381
5	0.0002	0.2399
10	0.0325	0.2376
20	0.1874	0.2435
50	1.2818	0.2354
100	3.8911	0.2356

increase in the external coupling rate γ_e. However, the resonance amplitude does not change monotonically versus h. For small grating depth, increasing the grating amplitude increases the resonance amplitude up to the depth of around 20 nm. Further increase of h leads to reduction of the resonance amplitude.

To obtain the values of the coefficients γ_e and γ_i for each h, we consider the difference of absorption in each case from the absorption of planar geometry. This gives the effect of guided-mode excitation independent of the influence of interference. Then, we fit a Lorentzian curve of the form suggested by Eq. 4.9 (for $N = 1$) to the corresponding guided-mode resonance absorption curve. Table 4.1 and Fig. 4.5 show the obtained coefficients (γ_e and γ_i) for different grating depths (h). The internal loss rate γ_i is almost fixed, independent of the grating depth, but the external coupling rate is monotonically increasing as the grating depth increases [7]. For small grating depth, the effect of internal loss is more pronounced than the external cou-

[7] This monotonicity may be violated for strong coupling. [107].

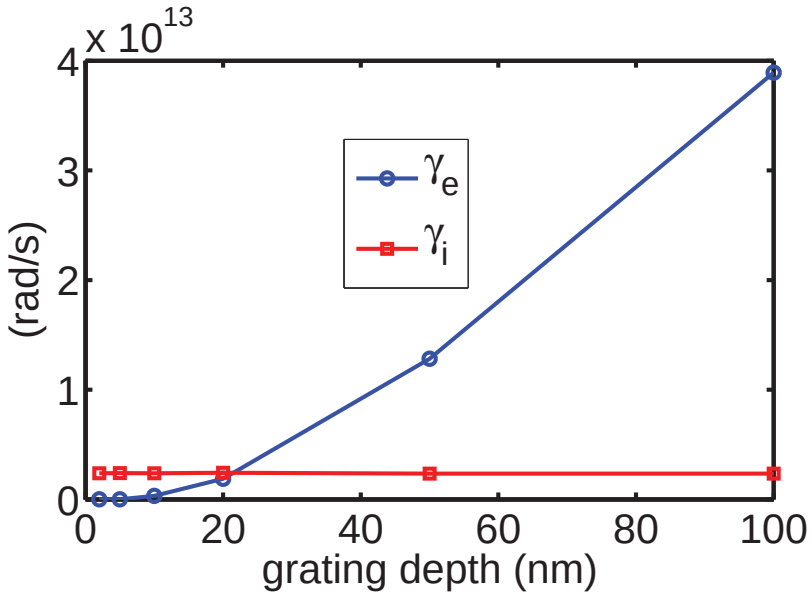

Figure 4.5: The coefficients γ_e and γ_i as a function of the grating depth.

pling ($\gamma_i > \gamma_e$) but for large grating depth, the contrary is true ($\gamma_e > \gamma_i$). There is a point where γ_e and γ_i equate. In this example, this occurs at around a grating depth of 20 nm. As Fig. 4.4 shows, the grating depth of around 20 nm results in a resonance which can absorb light completely at around its peak. The condition $\gamma_e = \gamma_i$ is called the "critical coupling" condition [18]. A single Lorentzian resonance reaches unity at its peak only when the critical coupling condition applies. Thus, for narrowband applications, to attain maximal absorption it is necessary that $\gamma_e = \gamma_i$. For wideband application, as in the case of solar cells, critical coupling does not lead to maximal absorption because it is not only the peak of the Lorentzian that matters and one should look at the average absorption provided by the Lorentzian over a wide wavelength range. In this case, the "over-coupling" condition should result in maximal coupling, which means $\gamma_e > \gamma_i$ [20].

To continue the discussion, we come back to Eq. 4.9. Different conclusions can be made based on this equation.

1. Absorption depends on both external coupling rate (γ_e) and internal loss rate (γ_i). This means that if absorption is very small, as in the light-trapping regime of thin-film solar cells, the resonance peak value in the absorption spectrum will not be very high, which is in agreement with experimental observations and simulation results.

2. Due to symmetry of Eq. 4.9, it is expected that large external coupling can have the same impact as large absorption (internal loss rate).

3. Absorption is larger if there is only one output port ($N = 1$) because N appears only in the denominator of Eq. 4.9. This justifies putting a back-reflector at the bottom of solar cells and working with sub-wavelength gratings.

Since the application is wide-band, we assume that the resonance is mostly contained within the wavelength range of interest. Then, the contribution of a single resonance peak on the absorption can be calculated by integrating from $-\infty$ to ∞ instead of the range of interest. The maximal value that the corresponding integral can take is equal to

$$\sigma_{max} = \int_{-\infty}^{\infty} A(\omega) d\omega \Big|_{max} = \frac{2\pi\gamma_i}{N} \tag{4.10}$$

To obtain this equation it is assumed that $\gamma_i \ll \gamma_e$. If there are M identical resonances, the average absorption over a angular frequency range of $\Delta\omega$ can be obtained by multiplication of σ_{max} by M an dividing the result by $\Delta\omega$.

$$\sigma_{max} = \frac{2\pi M\gamma_i}{\Delta\omega N} \tag{4.11}$$

Having established an equation for the general form of absorption, the role of periodic structures can be now incorporated into the model. Let us assume that the texture is a grating pattern with square geometry with a period of L in both periodicity directions. If the cell thickness is d, the density of resonances at an angular frequency ω_0 can be approximated as

$$M(\omega) = \frac{8\pi n^3\omega^2}{c^3}\left(\frac{d}{2\pi}\right)\left(\frac{1}{S_{uc}}\right)\Delta\omega \tag{4.12}$$

where S_{uc} is the surface area of a unit cell in the reciprocal lattice and is equal to $(\frac{2\pi}{L})^2$ and $\frac{\sqrt{3}}{2}(\frac{2\pi}{L})^2$ for square and hexagonal geometries respectively. Finally, one finds the absorption enhancement factor by dividing the average absorption σ_{max} from Eq. 4.11 to the single-pass absorption (αd) [8]

$$F = \frac{2\pi\gamma_i M}{\alpha d\Delta\omega N} \tag{4.13}$$

Fig. 4.6a and Fig. 4.6b show the square and the hexagonal geometries respectively, both in real space. The distance between each two closest points is Λ. Fig. 4.6c and Fig. 4.6d show the two geometries in reciprocal space. The dots denote conditions where the diffraction occurs, i.e. where Bragg condition is satisfied. The circle shows schematically the condition of propagation in air, i.e. $\left|k_{\parallel}\right| \leq k_0$. The number of diffraction orders (N) is equal to the number of dots within the circle, and it is equal to one until the frequency gets so large that the first order diffraction orders appear. For the square lattice, more dots occur within the circle for

[8] As already mentioned, for a weakly absorbing film, single-pass absorption can be approximated as αd where α is the absorption coefficient of the film and d is its thickness.

the same radius, which means that the reciprocal lattice is denser for square geometry compared to the hexagonal geometry. This is also observed in Fig. 4.6e which shows the number of orders as a function of the normalized period (Λ/λ where λ is the wavelength)[9] for both geometries. For the hexagonal geometry the jumps in number of orders are less but more pronounced compared to the square lattice. However, overall the square geometry supports more diffraction orders, especially at larger normalized periods.

Based on Eqs. 4.11 and 4.13 both the absorption and the enhancement factor are proportional to M/N, hence, for maximal absorption, there should be as many resonances and as few diffraction orders as possible. As the normalized period increases, N increases but the number of resonance (M) increases as well (Eq.4.12). Absorption enhancement is thus a trade-off between the number of resonances and the number of diffraction orders.

Fig. 4.6f shows the values of the enhancement factor based on the assumption of bulk approximation $\gamma_i = \alpha c/n$ [20]. The horizontal axis is the normalized period. The horizontal line shows the $4n^2$ limit which is obtained under the condition of Lambertian scattering of light by the interfaces. Because of the discrete nature of the diffraction phenomena, it is observed that the peak of the enhancement factor F occurs for $\Lambda/\lambda = 1$ for square geometry. This primarily means that for a fixed period Λ, absorption is enhanced most efficiently for wavelengths slightly larger than Λ. However, for wavelengths just below Λ, the enhancement factor drops to values smaller than $4n^2$. Because usually the absorber material is known, and thus the wavelength range of interest for absorption enhancement is specified, we can define a wavelength λ as the target and try to provide design criteria for Λ. Based on the following intuition, the highest average absorption can be obtained under the condition that the period is taken slightly smaller than the wavelengths of interest. This means that for example for a-Si, the period should be at most equal to 600 nm where absorption enhancement becomes important. Shorter wavelengths do not correspond to the assumptions of these calculations because absorption coefficient is large enough to absorb light efficiently. Similar conclusions can be made for hexagonal geometry.

To summarize, at very small periods, no diffraction phenomena are observed. For square geometry, the first order diffraction occurs at $\Lambda_{peak} = \lambda$. The onset of the corresponding graph, i.e. the part between the normalized period of zero up to the normalized period of around one, in Fig. 4.6f can be expressed in the following form

$$F = 4\pi n^2 \left(\frac{\Lambda}{\lambda}\right)^2 \tag{4.14}$$

which passes the $4n^2$ limit at $\Lambda_{start} = \frac{\lambda}{\sqrt{\pi}} \approx 0.56\lambda$. Absorption enhancement is predicted to be most efficient in the range of normalized periods between Λ_{start} and Λ_{peak}. For hexagonal geometry, $\Lambda_{peak} = \frac{2}{\sqrt{3}}\lambda$ and F has the following form at the start, before the appearance

[9] The quantity that we refer to as the “normalized period” is also called the “normalized frequency" in the context of periodic structures.

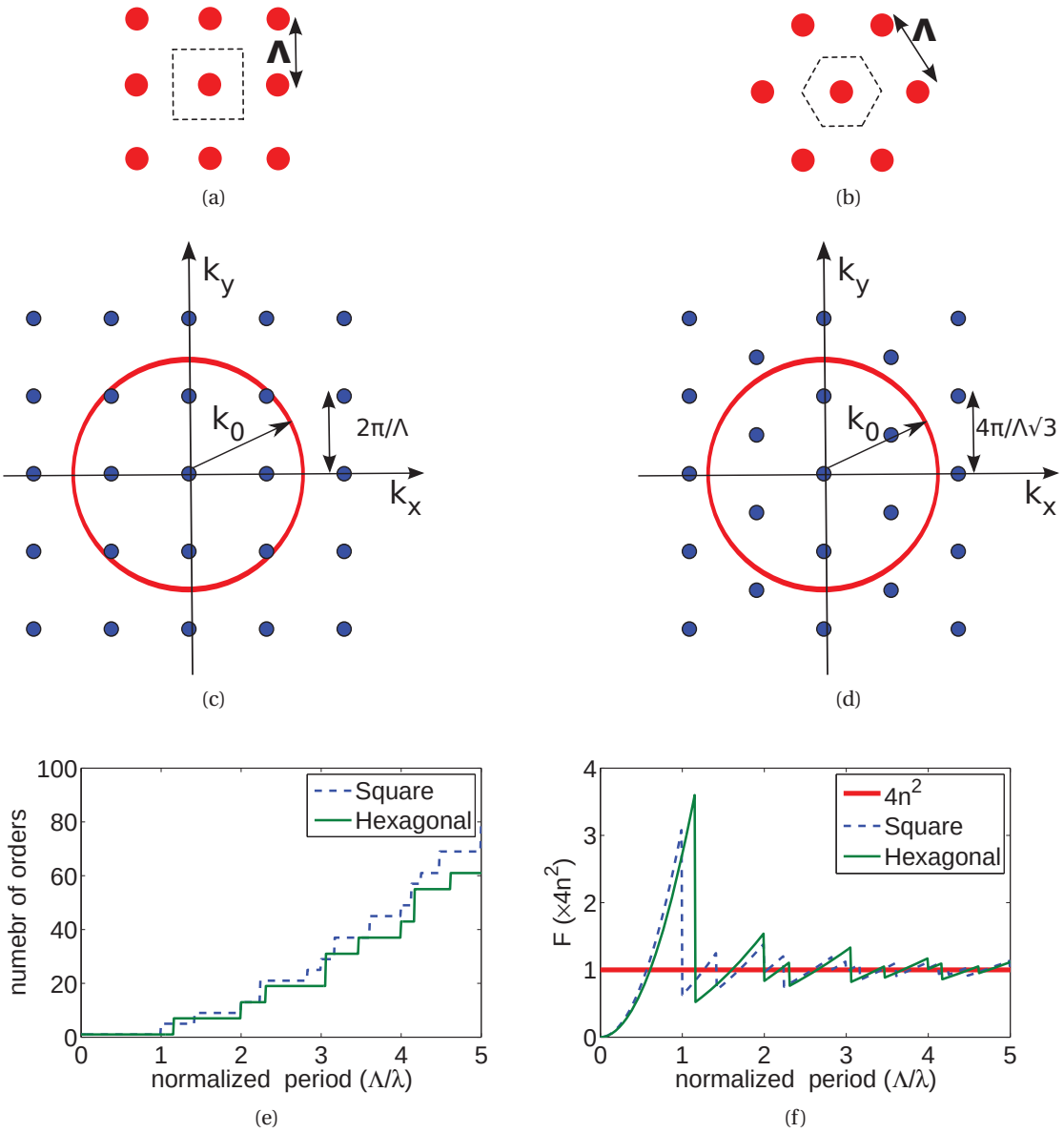

Figure 4.6: (a): Schematic of the square lattice is real space. (b): Schematic of the hexagonal (triangular) lattice is real space. In (a) and (b) the unit cell is represented as dashed. (c): Reciprocal space of square lattice. (d): Reciprocal space of hexagonal lattice. In (c) and (d) the circle corresponds to the wave-vector in free space. The reflection orders are associated with the dots. (e): Number of diffraction orders for a 2D grating with a square or hexagonal geometry as a function of normalized period. (f): Absorption enhancement factor for a 2D grating with a square or hexagonal geometry as a function of normalized period. The horizontal line shows the $4n^2$ limit.

of first-order diffraction:

$$F = \frac{\sqrt{3}}{2} 4\pi n^2 \left(\frac{\Lambda}{\lambda}\right)^2 \tag{4.15}$$

The $4n^2$ limit is surpassed in the wavelength range with between Λ_{peak} and Λ_{start}. This shows that hexagonal geometry supports enhancement values above $4n^2$ for a broader range of Λ:

$$\frac{\Lambda_{peak} - \Lambda_{start}}{\lambda} = \begin{cases} 0.44 & \text{(square)} \\ 0.54 & \text{(hexagonal)} \end{cases} \tag{4.16}$$

Furthermore, the peak value of F is equal to $8\pi n^2/\sqrt{3}$ and $4\pi n^2$ for hexagonal and square geometry respectively, which reveals that hexagonal geometry should enhance absorption more significantly. Actually, the best fabricated solar cells which use gratings as the light-coupling mechanism are based on hexagonal gratings [86, 108] .

4.2 Light trapping in solar cells at the extreme coupling limit

In this section, we[10] focus on the enhancement provided by the guided modes in thin-film solar cells with a wavelength-scale periodic coupler. By using temporal coupled-mode theory [18, 20], we study the angular dependence of the limit of light absorption enhancement. Our model is different from calculations of Yu *et al.* for thin films [20] because we simultaneously consider both the thin film and the wavelength-scale grating texture. Furthermore, our model can handle multiple modes in the thin film as well as a single mode in contrast to the model of Yu *et al.* for thin films. In this part we extend the model to wide wavelength ranges and oblique illumination. Furthermore, we consider the modal structure of the thin film absorber to weight the guided modes based on their impact on the absorption. For the sake of simplicity and without losing generality, we apply our model to a dielectric slab with refractive index $n = 4$ and thickness $d = 200$ nm embedded in air. The conclusions are not limited to the structure under investigation and can be observed for similar geometries, even for a complete solar cell stack. The refractive index and the thickness are similar to the one of a thin film a-Si solar cell. We show that the enhancement factor depends on how much the energy of the guided mode is confined to the thin film absorber. Wave confinement to the cell is characterized with the "energy overlap", which is defined here as the fraction of the electromagnetic energy of the mode which is spread over the active layer. We also demonstrate that for a high index absorber, for example silicon, almost all of the mode energy is inside the film. So, one may neglect the impact of the energy overlap. However, we do not

[10] This part of the thesis is based on my recent publication, Ref. [82]. By using "we", I include all of the co-authors of the mentioned paper.

use this simplification in our calculations here.

This section is organized as follows. First, in subsection 4.2.1, we explain the temporal coupled-mode theory which is the basis of our calculations in this part. In subsection 4.2.4 we calculate the limit of absorption enhancement at normal incidence for a thin-film solar cell based on a 1D grating. Then we extend the calculations to oblique incidence in subsection 4.2.5. The effect of wave confinement to the cell is discussed mainly in sections 4.2.2 and 4.2.3.

4.2.1 Overview of temporal coupled mode theory

We have already mentioned the basic coupled-mode formulation in section 4.1.2. Here we explain application of the formulation to thin film structures with wavelength-scale periodic texture. In Eq. 4.13, it is worth to investigate the relation between α and γ_i. If we assume that the optical wave observes the solar cell as a bulk material, the bulk approximation

$$\alpha = n\gamma_i / c \tag{4.17}$$

can be used [20] where c is speed of light in air. However, Eq. 4.17 is not correct for thin films [30] because γ_i is the loss rate of the "whole structure" whereas α describes the absorption coefficient only for the "bulk" of the absorber. In other words, γ_i is affected by the modal dispersion of the multilayer stack. One can find the "effective absorption coefficient" α_{wg} of the complete structure such that it can be expressed versus γ_i similar to Eq. 4.17. Evolution of the amplitude a of a guided-mode resonance can be described in the temporal or the spatial domain

$$\frac{da}{dt} = \left(j\omega - \frac{\gamma}{2}\right) a + \cdots \tag{4.18}$$

$$\frac{da}{dx} = \left(jk_{\parallel} - \frac{\alpha'}{2}\right) a + \cdots \tag{4.19}$$

Here γ and α' represent photon loss rate and damping factor, z is the propagation direction along the waveguide. The source terms are not shown in Eq. 4.19. Both α' and γ include internal loss and external coupling effects. If there is no external coupling, $\alpha' = \alpha_{wg}$ and $\gamma = \gamma_i$. It is then possible to conclude from Eq. 4.19 that

$$\frac{dx}{dt} = v_p = \frac{\omega}{k_{\parallel}} = \frac{\gamma_i}{\alpha_{wg}} = \frac{c}{n_{wg}} \tag{4.20}$$

where v_p is the phase velocity and n_{wg} is the "effective refractive index" of the waveguide.

The loss rate γ_i is linked to α_{wg} via

$$\alpha_{wg} = n_{wg}\gamma_i / c \tag{4.21}$$

Eq. 4.21 is not strictly correct because it considers the phase index $n_p = k_\parallel / k_0$ (k_0 is wave vector of light in air) as the effective refractive index of the film. Actually the group index $n_g = \partial k_\parallel / \partial k_0$ gives a better approximation of the effective refractive index. This can be explained by considering a guided mode traveling inside the slab over an infinitesimal distance dx. The wave energy undergoes a decay of $e^{-\alpha dx}$ in space domain . The equivalent decay in time domain is equal to $e^{-\gamma_i dt}$, where dt is the time which the wave takes to travel the distance dx. Since energy is guided in the waveguide at a speed equal to the group velocity v_g, time and space elements can be related via $dt = dx/v_g$. The paradox of the latter conclusion and Eq. 4.20 can be explained by noting that Eq. 4.20 is a slowly varying approximation of the resonant mode evolution, so, it only considers the phase variations. We still need to find the relation between α and α_{wg} in order to obtain the link between α and γ_i by using Eq. 4.21.

4.2.2 The effective absorption coefficient

Here I show that the ratio α_{wg}/α is equal to the energy overlap η .

Proof. Assume that a mode travels inside a film as depicted in Fig. 4.7. The wave loses energy with the effective absorption coefficient α_{wg} as it is guided along the film. If the whole space is filled with the absorber, this absorption coefficient will be equal to α. In a film with finite thickness, energy will be distributed over both the device and the outer space with the energy overlap η. The wave energy after passing a length dx is

$$E(dz) = E(0)e^{-\alpha_{wg}dx} = E(0)[\eta e^{-\alpha dx} + (1-\eta)] \tag{4.22}$$

Taylor expansion of Eq. 4.22 leads to $\alpha_{wg}/\alpha = \eta$. □

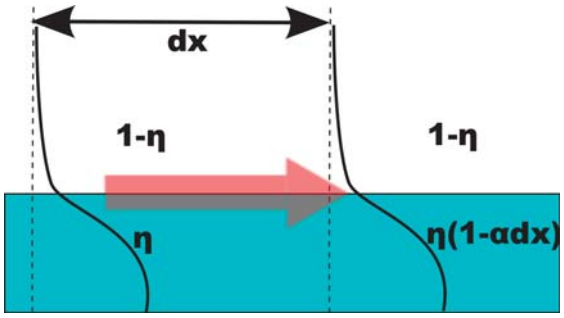

Figure 4.7: Schematic of a mode traveling inside an absorbing film with absorption coefficient of α. The mode energy has an overlap of η with the film.

So, we can write Eq. 4.13 as

$$F = \frac{2\pi c}{n_{wg} d \Delta\omega} \frac{M}{N} \eta \tag{4.23}$$

Here we see apparently the effect of wave spread outside the film. If η is small, the wave is spread over regions other than the absorber, thus the enhancement factor is reduced. We explain now that for high index films, almost the whole energy of the mode is inside the film. However, we consider the impact of energy overlap in our calculations.

4.2.3 The energy overlap

For a slab of thickness d at normal incidence, the electric field profile of even and odd modes can be easily obtained [107].

$$E_e = \begin{cases} \frac{\cos(k_z z)}{cos(k_z \frac{d}{2})} & (|z| \leq \frac{d}{2}) \\ \exp(-\alpha(|z| - \frac{d}{2})) & (|z| > \frac{d}{2}) \end{cases} \tag{4.24}$$

$$E_o = \begin{cases} \frac{\sin(k_z z)}{\sin(k_z \frac{d}{2})} & (|z| \leq \frac{d}{2}) \\ \exp(-\alpha(z - \frac{d}{2})) & (z > \frac{d}{2}) \\ -\exp(\alpha(z - \frac{d}{2})) & (z < -\frac{d}{2}) \end{cases} \tag{4.25}$$

where z refers to the direction normal to the interfaces and E_o and E_e refer to electric field of the odd and the even modes respectively. The energy overlap can be obtained via the electric field profiles.

$$\eta = \frac{n^2 \int |E_{slab}|^2 \, dz}{n^2 \int |E_{slab}|^2 \, dz + \int |E_{air}|^2 \, dz} \tag{4.26}$$

At non-perpendicular incidence, TE and TM polarizations must be distinguished. As in the case of normal incidence, the guided modes can be classified into odd and even in each polarization.

In TE polarization, the electric field is parallel to the slab boundary and the electric field of the modes can be expressed with Eq.s 4.24 and 4.25. Therefore, the energy overlap η can be obtained similarly to the case of normal incidence. Figs. 4.8a and 4.8b show the energy overlap versus phase index n_p and photon energy E for the slab (d = 200 nm , n = 4) under oblique incidence. Since η is the same as for normal incidence, Figs. 4.8a and 4.8b can also be used for normal illumination of light. The energy overlap is very close to unity almost everywhere except near the light line of air (n_p = 1). The guided modes corresponding to each case are shown in Fig. 4.8 with red curves with circle markers. In a narrow spectral

range, there is an even TE mode partly in the low η region close to the light line of air. As this mode approaches the light line of air, its group index decreases gradually, therefore, Eq. 4.23 predicts that the mode should provide high enhancement factors. However, this advantage is compromised by the small η which means extension of the wave tail outside the guide and subsequently, reduction of F.

In TM polarization, the magnetic field has a form similar to the electric field in TE polarization but the electric field has two components which can be derived from the magnetic field by using Maxwell equations.

$$E_x = \frac{-j}{\omega\epsilon}\frac{\partial}{\partial z}H_y \tag{4.27}$$

$$E_z = \frac{j}{\omega\epsilon}\frac{\partial}{\partial x}H_y \tag{4.28}$$

By applying Eq.s 4.27 and 4.28 and using the form of the magnetic field which is already described in Eq.s 4.24 and 4.25, the electric field profiles in TM polarization can be obtained. To calculate the intensity profile, both components of the electric field must be considered.

$$I = |E_x|^2 + |E_z|^2 \tag{4.29}$$

After some algebraic manipulation the following intensity profiles can be obtained for the TM polarized modes.

$$I_e = \begin{cases} \frac{\mu_0}{\epsilon_0 n^2}\frac{k_z^2\sin^2(k_z z)+\beta^2\cos^2(k_z z)}{k_0^2\cos^2(k_z\frac{d}{2})} & (|z|\le\frac{d}{2}) \\ \frac{\mu_0}{\epsilon_0}\exp(-2\alpha(|z|-\frac{d}{2})) & (|z|>\frac{d}{2}) \end{cases} \tag{4.30}$$

$$I_o = \begin{cases} \frac{\mu_0}{\epsilon_0 n^2}\frac{k_z^2\cos^2(k_z z)+\beta^2\sin^2(k_z z)}{k_0^2\sin^2(k_z\frac{d}{2})} & (|z|\le\frac{d}{2}) \\ \frac{\mu_0}{\epsilon_0}\exp(-2\alpha(|z|-\frac{d}{2})) & (|z|>\frac{d}{2}) \end{cases} \tag{4.31}$$

where I_o and I_e refer to intensity of the odd modes and even modes respectively. The energy overlap can be obtained via the intensity profiles by applying Eq. 4.26.

Figs. 4.8c and 4.8d show the energy overlap for the slab (d = 200 nm, n = 4) under TM polarized illumination. As in the previous cases, the energy overlap is almost unity everywhere except near the light line of the air (n_p = 1). Fig. 4.8c shows an even TM mode which occurs only very close to the light line of air. Since η is very small in this region, this mode cannot result in very huge absorption enhancement although its group index is small.

Altogether, the incident angle does not have a dramatic effect on the energy overlap for high index cells. Hence, one can almost always approximate $\eta \approx 1$ by considering a margin around

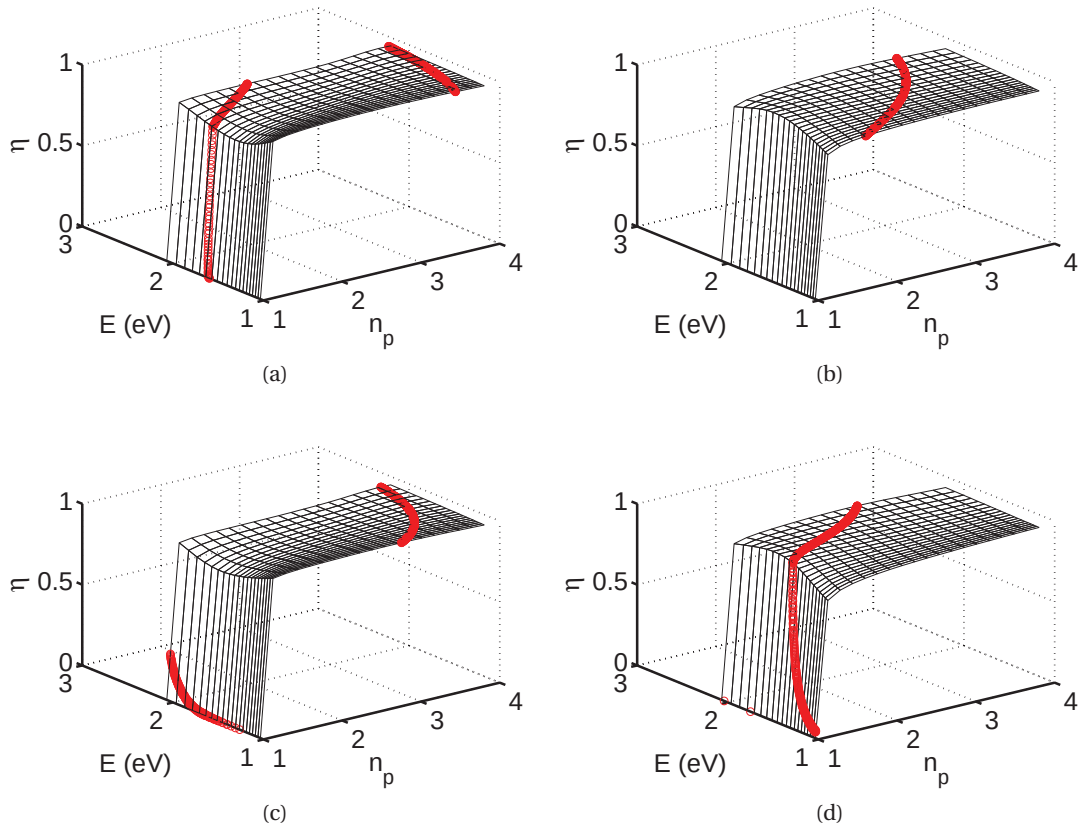

Figure 4.8: The energy overlap as a function of photon energy (eV) and phase index for (a) even modes under TE polarized light, (b) odd modes under TE polarized light (c) even modes under TM polarized light (d) odd modes under TM polarized light. The energy range corresponds to the wavelengths between 600 and 1200nm. The red dotted curves represent the guided modes corresponding to each case.

the light line of air and due to section 4.2.2, $\alpha_{wg} \approx \alpha$.

Note that the diagrams of Fig. 4.8 are plotted for a continuum of energy and phase index values but dispersion of the film produces a discrete spectrum. So, on the surfaces in Fig. 4.8 , only the n_p and E values corresponding to the guided modes i.e. the red dotted curves should be considered.

Having explained the expressions for energy overlap, we can now return to the calculation of the enhancement factor. In Eq. 4.23, the parameters M, N and n_{wg} and η need to be calculated. In the previous section we explained how N is obtained. The number of guided-mode resonances, M, is calculated by considering the number of intersections of the film dispersion diagram and the lines $k_{\parallel} = 2\pi m'/\Lambda$ which correspond to Bragg condition in the interval $[\omega, \omega + \Delta\omega]$. Fig. 4.9 demonstrates the dispersion diagram of a slab with refractive index of $n = 4$ and thickness $d = 200nm$ under TE-polarized illumination. By TE we mean where the electric field is normal to the incidence plane. Treatment of TM polarization is

similar. Despite the simplicity of this structure, the results can be generalized to more complex structures e.g. complete solar cells consisting of several layers. We assume a 1D grating texture for the slab with period Λ = 500 nm. The energy interval of interest is equivalent to wavelengths from 600 to 1200 nm because a-Si cells need light trapping mainly in the range from 600 to 800 nm and the different types of crystalline silicon cells e.g. micro-crystalline, mono-crystalline, etc. can be enhanced by light trapping mainly in the range from 800 to 1200nm. Different diffraction orders m=1,2,3 for normal incidence correspond to the vertical lines. The allowed excitations within the wavelength range of interest are marked with circles.

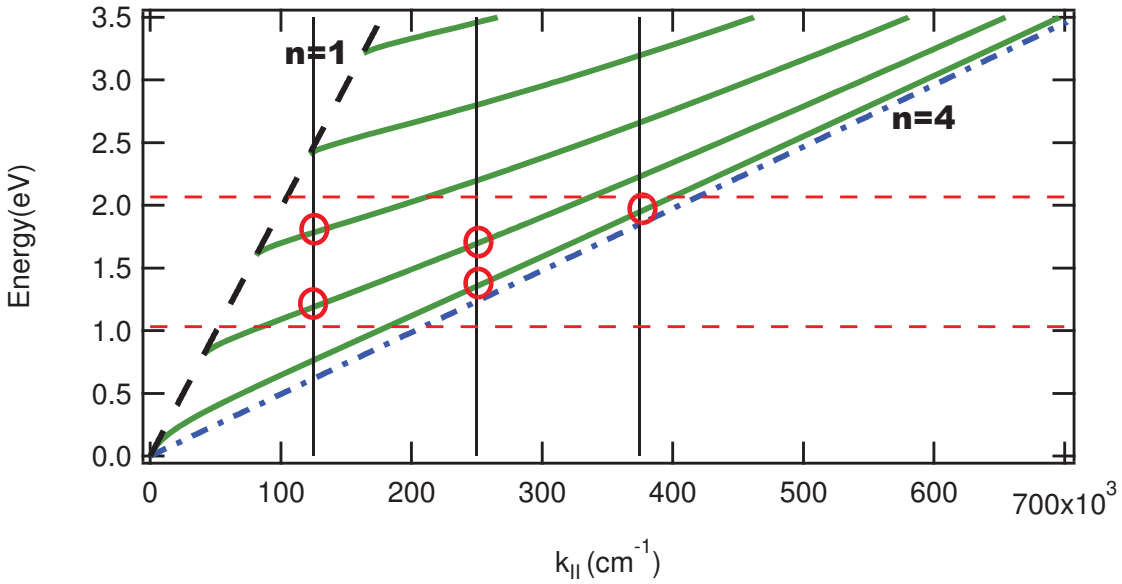

Figure 4.9: Dispersion of a film with refractive index n=4 and thickness d=200 nm in TE polarization. The guided modes (green curves) occur between the light line of air (dashed black) and dielectric (dotted dashed blue). The periodic texture excites the guided modes where they satisfy Bragg condition (vertical lines). The dashed horizontal lines correspond to 600 and 1200 nm. Resonances are illustrated by the red circles.

Based on Eq. 4.23, using the phase index instead of the group index can result in overestimation of the enhancement factor F because the phase index is smaller than the group index. However, if the definition of the group index is ambiguous, for example for very broad resonances, the phase index can be used as an approximation.

The presence of n_{wg} instead of n in the denominator is a major difference between Eq. 4.23 and the calculations of Ref. [20] for thick solar cells. Of course in Ref. [20] the case of a thin-film solar cell has been investigated too, in which modal properties have been considered, however, there are at least two main differences between their method and our approach. First, they use a continuum model to count the resonances supported by the grating texture (Eq. (11) in [20]). This can be a good approximation for large periods or random textures, but when dealing with wavelength-scale gratings the resonances might be well distinguished and one should use a discrete model. Second, their model for thin films is appropriate to treat a single mode film since they count the resonances in the two dimensional k_{xy} space but our

model can treat multiple modes since we count the resonances in the three dimensional k_{xyz} space.

In summary, by using group index for the effective waveguide index, and by application of the corresponding energy overlaps, we weight the absorption due to a resonance based on the resonance position in the dispersion diagram. In this way, we take into account the modal properties of the thin film structure.

4.2.4 Limit of absorption enhancement under normal incidence

Fig. 4.10 shows the enhancement factor of the slab ($n = 4$, $d = 200$ nm) versus the normalized period ($\Lambda_n = \Lambda/\lambda$) for two wavelength ranges from 600 to 800 nm and from 800 to 1200 nm. For each of these spectral ranges, we calculate the enhancement factor for a 1D grating through the following procedure:

1. We calculate the enhancement factor F for a certain grating period (Λ) for the spectral ranges over tiny wavelength subintervals to consider the dispersion diagram point by point.

2. Then, we average F over the considered spectral range. The value Λ_n is obtained by dividing the period to the central wavelength of the considered wavelength range.

3. Up to here, the method gives us one point in the graphs of Fig. 4.10. To complete the graph we change the period and repeat this procedure.

Fig. 4.10 shows that the enhancement factors that we obtain are smaller than the values suggested by Yu *et al.* for thick layers regardless of polarization and wavelength range. The reason is that in our calculations the absorber bulk refractive index is replaced by the group index. This conclusion can be extended to 2D gratings as well. The difference from the 1D case is the more complicated counting procedure. Note that the wavelength intervals used in our simulations are wide. For small spectral ranges, the enhancement factor can be higher.

An important observation is that by changing the period of the grating (Λ), the enhancement factor oscillates [20]. These fluctuations are due to the discrete changes of the number of reflected orders as the wavelength changes. There is a balance between two different phenomena:

1. on one hand increasing the normalized period leads to appearance of more diffraction orders (N) and hence, reduction of F via Eq. 4.23.

2. On the other hand, increasing the normalized period increases the number of excited modes (M) which in turn, increases F.

However, there are more resonances compared to the number of reflection orders. Thus, M is more similar to a continuum compared to N. Therefore, two types of fluctuations can be observed in the enhancement factors plotted in Fig. 4.10: one with high repetition frequency and the other one with lower repetition frequency. The first one corresponds to changes in M and the second one is related to N. For thick structures, M can be approximated with a continuum and only the discontinuities pertaining to N (low frequency) are observed.

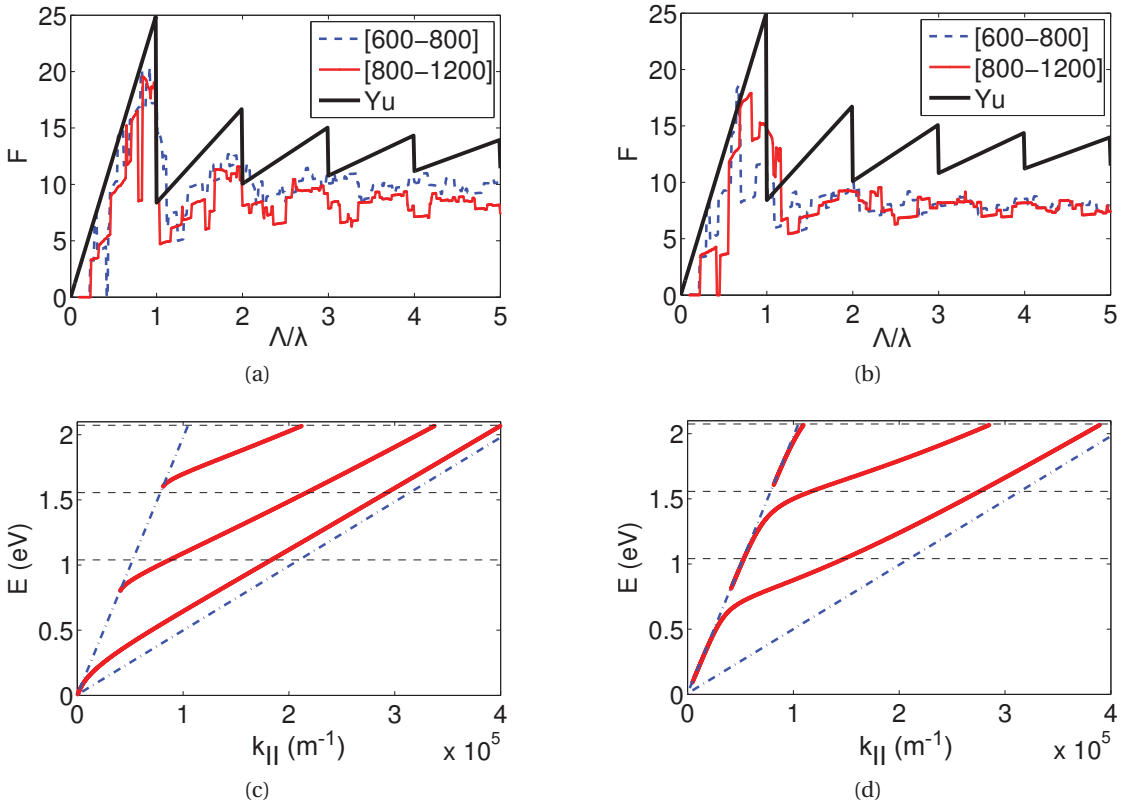

Figure 4.10: (a) The enhancement factor introduced by 1D gratings in TE polarization versus the normalized period for the slab (d=200 nm, n=4). Dashed: Wavelength range from 600 to 800 nm. Solid with markers: Wavelength range from 800 to 1200 nm. Bold solid: Yu's model (thick absorber), (b) Same as (a) but for TM polarization, (c) Dispersion diagram of the slab for TE polarization, (d) same as (c) for TM polarization. The horizontal dashed lines in (c) and (d) correspond to the wavelengths 600, 800 and 1200 nm.

Fig. 4.10c shows the dispersion plot of the slab in TE polarization. The borders of the spectral ranges from 600 to 800 nm and from 800 to 1200 nm are shown by horizontal lines. In the high energy range ([600-800] nm) there are three guided modes but at low energy range ([800-1200] nm), there are only two modes. This is the reason why in Fig. 4.10a TE polarized light can result in higher enhancement factor in the high energy range compared to the low energy range.

Fig. 4.10d shows the dispersion plot of the slab in TM polarization. In TM polarization the highest order mode is very close to the light line of air, which means that it is spread a long distance outside the slab over air. It is shown in section 4.2.3 that a major part of the energy of this mode occurs outside the slab. There are thus two TM modes in both energy ranges. This can explain why in TM polarization, there is not much significant difference between the enhancement factors for the two energy ranges as shown in Fig. 4.10b.

One may expect huge enhancement factor close to the light line of air due to Eq. 4.23 because both group index and phase index take their lowest values there. This happens for example for the second TM mode in Fig. 4.10d. However, this lower effective index is compromised by the low confinement of the mode to the guide in some cases as the third TM mode in the example. Nevertheless, it should be possible to find a region of optimized conditions in the dispersion diagram.

4.2.5 Absorption limit under oblique illumination

In this section the absorption enhancement limit provided by the guided-mode excitation is calculated at arbitrary angles. We consider in-plane incidence over the slab ($n = 4$, $d = 200nm$) as depicted schematically in Fig. 4.11a, to simplify the study. As earlier, we consider a 1D texture; 2D case can be treated accordingly.

The incident angle θ modifies the enhancement factor by changing Bragg condition

$$k'_{\parallel,m} = k_{\parallel,m} + k_0 \sin\theta \tag{4.32}$$

where $k'_{\parallel,m}$ and $k_{\parallel,m}$ show the parallel component of the wave-vector of the m-th diffraction order at normal and oblique incidence respectively and k_0 is the wave-vector of the light in air.

Change of the incident angle modifies the Bragg condition and consequently varies the resonance conditions for guided modes. Fig. 4.11b shows the variation of the resonant energy (equivalently the resonant frequency) corresponding to positive and negative orders introduced by changing the incident angle. The vertical and tilted dashed lines correspond to the Bragg conditions under normal and oblique illumination both for $\Lambda = 500$ nm. For simplicity, only one mode of the film and two orders ($m = \pm 1$) are demonstrated between the light lines of the air and the dielectric $n = 4$. By starting from normal incidence, as the incident angle θ is increased, the positive order goes farther from the origin ($k_\parallel = 0$) but the negative order gets closer to it. In Fig. 4.11b the dashed lines correspond to $\theta = 20°$. Because both positive and negative orders undergo the same wave-vector shift, their corresponding resonant energies are not the same any more. This asymmetry in satisfying the resonance condition is a natural result of the breaking symmetry provoked by changing the incident angle.

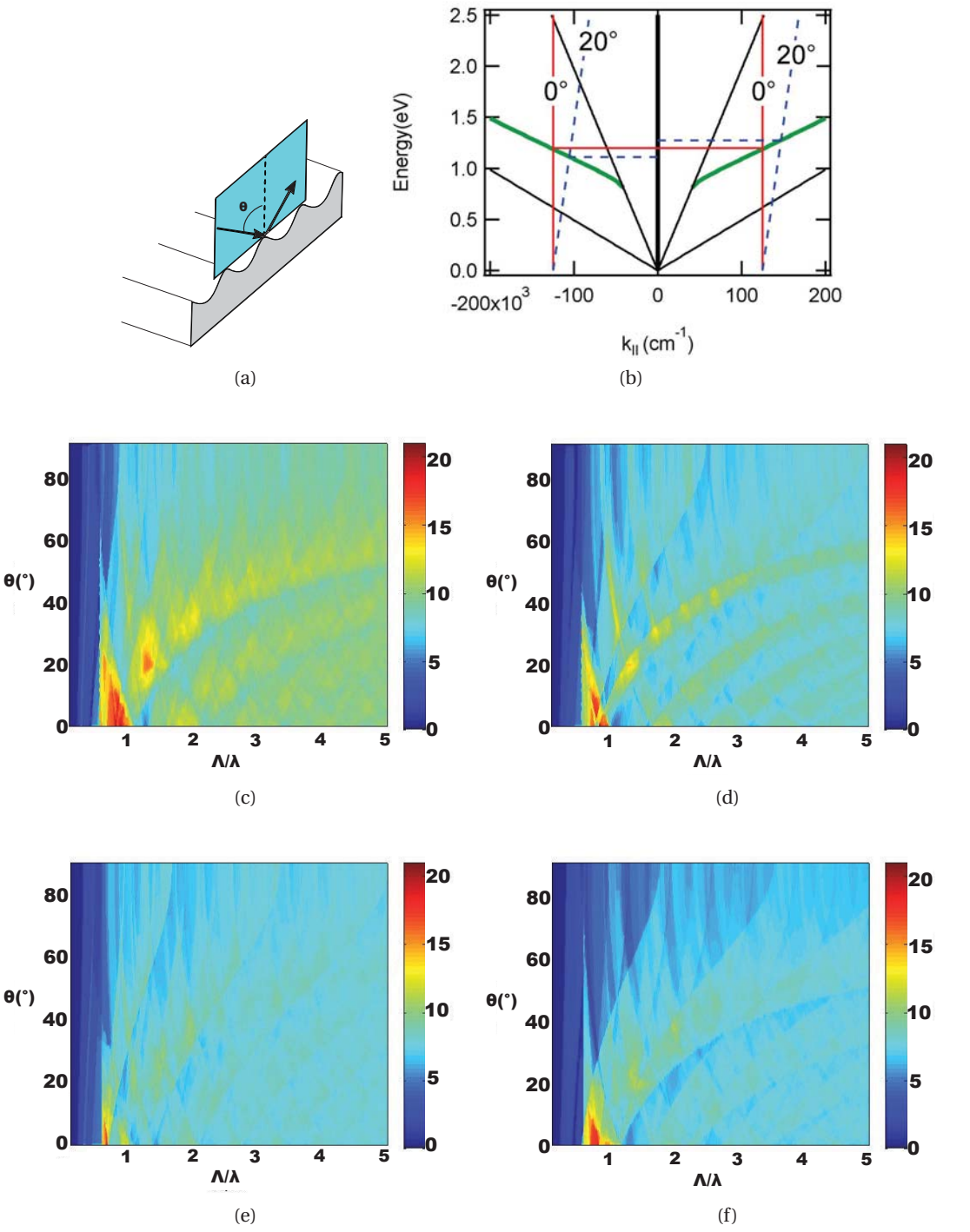

Figure 4.11: (a) Schematic view of the grating under in-plane oblique incidence. (b) shift of the resonant energy of the positive and negative orders due to the change of the incident angle from 0° to 20°. (c) Angular dependence of the F under TE polarized illumination over the wavelength range [600-800] nm. (d) same as "c" for TM polarized illumination. (e) same as "c" for the wavelength range [800-1200] nm. (f) same as "e" for TM polarized illumination.

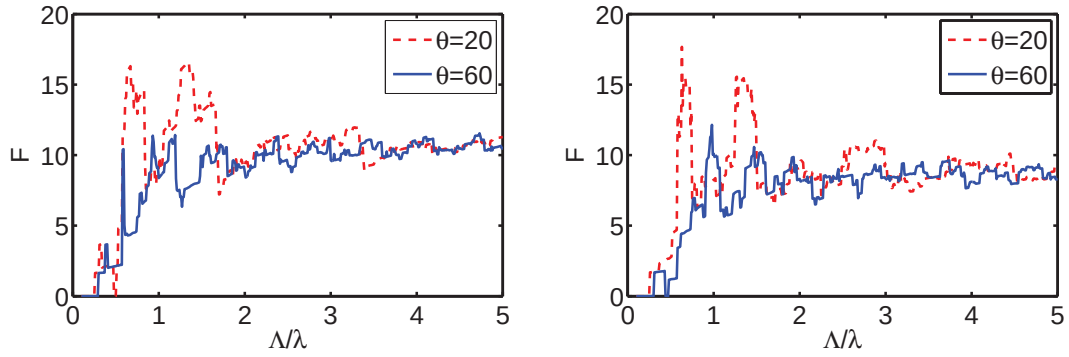

Figure 4.12: (a) F under TE polarized illumination over the wavelength range [600-800] nm for the incident angles of 20° and 60°. (b) same as "a" but for TM polarization.

Fig. 4.11c and Fig. 4.11d show the angular behavior of the enhancement factor of the slab ($n = 4$, $d = 200$ nm) for TE and TM polarized light over the wavelength range from 600 to 800 nm. Equivalently, Fig. 4.11e and Fig. 4.11f show similar results for the interval from 800 to 1200 nm. Although the impact of energy overlap is negligible except very close to the line of the air (section 4.2.3) we consider it in our calculations. At normal incidence, the enhancement factor follows the same sawtooth trend as observed in Fig. 4.10 . As the incident angle is increased, the peaks of the enhancement factor move in an ordered way in both polarization directions.

Peaks of the enhancement factor F move in the period-angle plane on two series of curves with positive and negative slope, which are associated with the positive and negative diffraction orders. Increasing the incidence angle results in higher resonant energy for positive orders as demonstrated in Figure Fig. 4.11b. Thus, for a fixed grating period, the normalized period (Λ/λ) becomes larger too. Therefore, the positive and negative slopes in 4.11 correspond to the appearance of the positive and negative diffraction orders respectively. Relatively high enhancement factors can be obtained at oblique incidence. This is a direct result of the asymmetric shift of the resonant energies of the positive and negative orders under oblique illumination.

Fig. 4.12 shows the enhancement factor for the discussed 1D grating for only two incident angles of 20° and 60° and in the wavelength interval from 600 to 800nm. The smaller incident angle permits larger enhancement factor at close-to-period wavelengths ($\Lambda_n = \Lambda/\lambda = 1$). For smaller wavelengths, there is no significant difference between the two angles. This is a general conclusion and agrees with the intuition that at the limit of large period, the grating should resemble a Lambertian scatterer [20].

It is worth mentioning that because solar illumination occurs at a limited range of incidence angles, it is possible to keep the condition of normal incidence at least to some extent. Based

on the wavelength range which affects the performance of the cell, periods can be found which can enhance light absorption more significantly. Also one should note that in all the calculations in this section and also in the prior research [20, 29, 30], coupling strength is assumed to be so large that its actual value does not affect the calculations. Also, other loss mechanisms such as parasitic absorption, imperfect collection of photo-generated carriers and reflection from the top interface of the cell would lead to a decrease in photocurrent.

4.3 Angular behavior of the absorption limit in thin film silicon solar cells

Light absorption in solar cells is a function of incident angle, regardless of the type of texturing. Unfortunately, most of solar cell literature deals with the case of normal incidence of light and ignores the impact of incidence angle. Recently, Yu *et al.* proposed a model to determine the light absorption enhancement limit for an arbitrary incidence angle [20]. In their model, Yu *et al.* considered an absorber film that is thick enough to envelop discrete modes by a continuum model. However, recent work on thin film devices with periodically textured interfaces showed that discrete waveguide modes can be distinguished, and that the excitation of these modes varies significantly with the angle of incidence [36]. In this section, we[11] investigate the upper limit of absorption enhancement in a thin film silicon solar cell based on a gratings pattern. We also take into account the angular dependence of this limit to find out how much and in which manner the absorption enhancement changes as a function of incident angle. The cell thickness is considered only a few hundreds of nanometers to simulate the case of a a-Si:H solar cell, which is normally in the range of 80 to 300 nanometers thick. Thicker cells degrade quickly when exposed to solar illumination due to Staebler-Wronkey effect [10] and thinner cells suffer from formation of shunts in fabrication.

Angular behavior of light absorption in thin film devices mainly depends on interference and resonant excitation of guided modes. Resonances are discussed here by taking into account the following properties; first, the field profile of a guided mode supported by a thin dielectric film can extend over a considerable distance out of the actual guiding medium. Second, the interface texture serves to couple energy from the incident light into a given mode. Similar to the previous section, we assume that the periodic texture is a slight deviation of the device interfaces from a planar structure. In other words, we treat the interface texture in terms of periodic perturbations. This assumption allows application of band-folding to the dispersion relation of the corresponding flat interface model.

A major assumption in most of the calculations of upper limit of absorption enhancement is that the amount of energy which is absorbed in the cell is completely absorbed in the active layer and is fully converted to photocurrent. Besides, it is commonly assumed that the wave is completely inside the structure. Furthermore, efficiency of coupling to a specific mode is assumed to be so large that it does not affect calculation of absorption upper bound (perfect

[11] Here “we” refers to all of the authors of Ref. [83].

coupling). In practice, there is always some parasitic loss which prevents the generated photons to be fully converted into photocurrent. Also, never the energy is fully bound to the solar cell. Besides, coupling efficiency can vary a lot for different modes.

We start our analysis in section 4.3.1 by obtaining the angular dependence of the enhancement factor for a slab geometry. Grating coupling is taken into account similar to section 4.2 by considering the Bragg condition. However, along the slab thickness, we use the closed-waveguide approximation as previously considered by Yu *et al.* for thick films [20]. We refer to this model as the "ideal model". As already mentioned, this approximation is not valid for thin-film solar cell. Hence, in section 4.3.2 we replace the closed-waveguide assumption by considering the dispersion diagram of a dielectric slab waveguide for the transverse resonance condition. We call this model as the "real model". We compare these two models in section 4.3.2. In section 4.3.5, we extend the analysis to a complete thin film silicon solar cell. Also we provide a general discussion on the effect of the incident light polarization, In section 4.3.6 the analysis is extended to the case of 2D gratings. For our analysis, we need a procedure to extract the modes of the planar structure and to count the corresponding resonances. This procedure is explained in section 4.3.3. In section 4.3.4, we describe how to calculate the enhancement factor over a wide wavelength range while considering the open waveguide condition. To find more practical values for absorption enhancement, the loss due to parasitic absorption over the supporting layers of the stack should be subtracted from the absorbed power to provide only absorption over the active layer. This modification is applied in Section 4.3.7. Note that this modification in the definition of the enhancement factor does not introduce a fundamental constraint on absorption enhancement, however, it provides a more applied approximation. Finally, in Section 4.3.8, we highlight some practical considerations. For example, we obtain an approximation of the maximal photocurrent enhancement provided by a 1D grating pattern.

4.3.1 Closed waveguide approximation: Idealized model

We calculate the enhancement factor for two slab thicknesses of 200 and 355 nm. The thickness of 355 nm is equal to the thickness of complete solar cell which will be discussed later. For simplicity, we use the same values of 1D and 2D limit throughout this section which are calculated for $n = 4$ via Eq. 4.13 by assuming the bulk approximation $\gamma_i = c\alpha/n$. We consider the physical slab thickness as the variable d in Eq. 4.13, thus, we neglect wave penetration outside the slab. As previously stated, we call this model the "idealized model". Later in section 4.3.2 we will consider wave penetration outside the solar cell; we will call the corresponding model the "real model". The three horizontal lines in Fig. 4.13 show the wide-band limits $\pi n = 12.57$ and $4n^2 = 64$ which correspond to 1D grating and for 2D textures respectively, and the narrow-band 1D limit of $2\pi n = 25.13$. The enhancement factor in Fig. 4.13 is larger for thinner slabs because of stronger single pass absorption over the thick slabs. The enhancement factor peaks at around normal incidence but still it is below the 2D wide-band limit. The enhancement factor is more sensitive to changes in refractive index for the thin

slab. This can be because for the thick slab, the single pass absorption will be large and modification of the refractive index will not change it dramatically. The enhancement factor approaches the πn line at large incident angles for the thin slab. For the thick slab, it surpasses this limit for almost normal incidence.

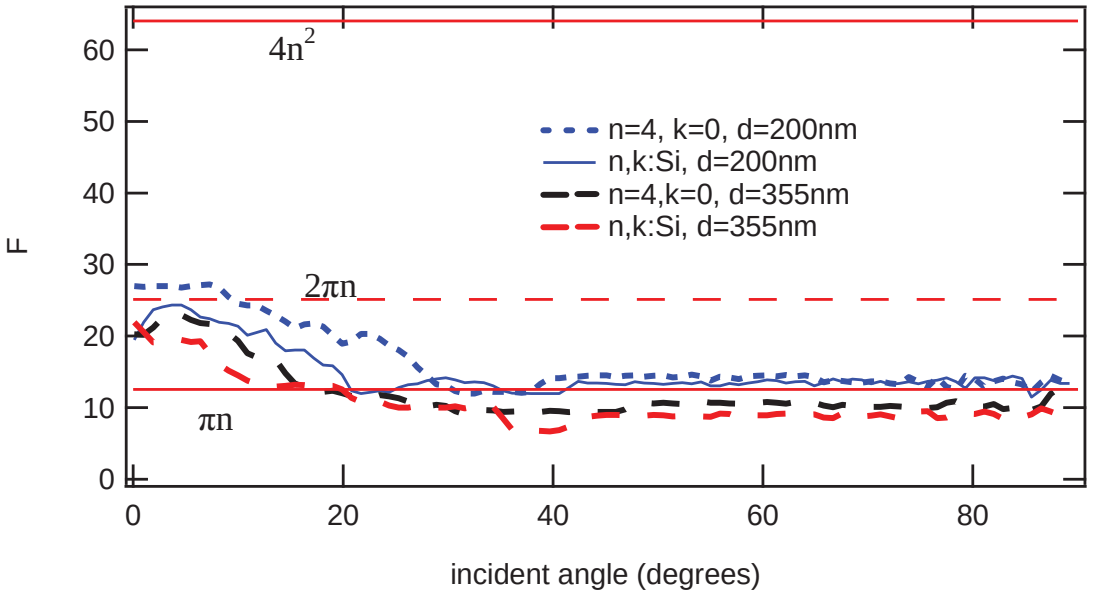

Figure 4.13: Enhancement factor of a dielectric slab averaged over the wavelengths from 600 to 900 nm as a function of incident angle for 1D grating with period of 560 nm. The horizontal lines represent the limit for 1D and 2D gratings. The other four curves represent the enhancement factor which is obtained by the "idealized" model for the 200 nm thick slab with n=4 (dotted blue), the 200 nm thick a-Si:H slab (solid blue), the 355 nm thick slab with n=4 (dashed black) and the 355 nm thick a-Si:H slab (dashed red). For simplicity, on axis incidence is considered only.

4.3.2 The open nature of the thin film

The assumption of periodicity along a cell thickness (in z direction) is not valid for open guided wave structures. In these devices, field penetration into air makes the effective guide thickness larger than its physical thickness. The difference between the effective and the physical thickness is not negligible if the mode is close to the light line of air in the dispersion diagram. This increased effective thickness makes the dispersion deviates the dispersion diagram of the device from the dispersion of a closed waveguide. This deviation normally happens in the form of a compression towards lower energies (longer wavelengths). This, in turn, means a higher density of guided modes, and thus, a higher potential for absorption enhancement.

To continue the discussion, we obtain the enhancement factor of a thin a-Si:H slab using the "real" model. We have recently applied the "real model" at normal incident to thin-film solar cells [109]. For other angles, both the number of channels N and the number of resonances

ΔM should be modified. Number of channels is the same for both "idealized" and "real" models because it only concerns the phase-matching (or equivalently the Bragg) condition in xy plane and is independent of the transverse direction z. Obtaining ΔM is more complicated and is explained here.

4.3.3 Counting the resonances of the flat interface structure

The Transfer Matrix Method (TMM) and the Reflection Pole Method (RPM) [61] are used to calculate the reflection and the dispersion diagrams respectively. Using TMM, forward and backward fields in the incident medium (air) and the transmission medium (silver) can be related with a simple 2 by 2 matrix Q.

$$\begin{pmatrix} A_t \\ B_t \end{pmatrix} = Q \begin{pmatrix} A_i \\ B_i \end{pmatrix} = \begin{pmatrix} q_{11} & q_{12} \\ q_{21} & q_{22} \end{pmatrix} \begin{pmatrix} A_i \\ B_i \end{pmatrix} \tag{4.33}$$

In the above equation, A and B stand for the forward and backward waves respectively and the indices i and t correspond to the incident or the transmission medium respectively. Without losing generality we assume all the waves normalized to the incident wave, i.e. $A_i = 1$. Since light does not illuminate the structure from the bottom, $B_t = 0$. Therefore, Eq. 4.33 reduces to the system of two equations and two unknowns which can be solved very easily. Specifically, reflection from the top interface can be represented as

$$r_c = r_c \exp\left(j\phi_c\right) = -\frac{q_{21}}{q_{22}} \tag{4.34}$$

Theoretically, poles of the reflection coefficient r_c correspond to the guided modes. As evident in Eq. 4.34, reflection becomes infinite when $q_{22} = 0$. The RPM monitors the phase ϕ_{RPM} of $q_{22} = \left|q_{22}\right| \exp\left(j\phi_{RPM}\right)$ when the longitudinal wave vector, $k_{\|}$, is changing. In the case of pure dielectric waveguides, ϕ_{RPM} will change in steps equal to π exactly at the $k_{\|}$ values corresponding to propagation constants of the waveguide modes. If loss is introduced into the structure as well, ϕ_{RPM} varies abruptly by about π around the propagation constants of the modes [61]. So, an "effective" number of modes can be found for each polarizations by the dividing amount of variation of ϕ_{RPM} by π. The word "effective" is used since in thin films, the individual resonances are relatively wide compared to the case of thick layers. Therefore, it is not always possible to distinguish different resonances since at each wavelength, there may be more than one resonance which enhances absorption.

To find the number of allowed resonances, ΔM, in each energy range $[E, \Delta E]$, we should con-

sider limitations imposed by both the ϕ_{RPM} and the periodicity P along x direction. The latter criterion necessitates that

$$k_{\parallel} = k_0 \sin\theta + \frac{2\pi m}{P} \tag{4.35}$$

Note that we take into account only parts of the phase diagrams which correspond to $k_{\parallel} > k_0$ to consider only the guided modes.

Once ΔM is calculated, it is possible find F via the "real model" as explained below.

4.3.4 Calculation of the enhancement factor in the "real model"

The process of finding the absorption enhancement factor, F, via the "real model" can be described as follows:

1. Divide the energy range into tiny subintervals δE.
2. Move on the curve of +1 diffraction order, i.e. $m = 1$ in Eq. 4.35, and find the change of ϕ_{RPM} (introduced in section 4.3.3) on this curve in each energy subinterval δE. Divide this phase shift by π to obtain the effective number of modes δm in δE.
3. Divide δm by the average phase index (n_p) on the curve $m = 1$ over δE.
4. Repeat the previous steps for different diffraction orders which excite the guided modes in the spectral range of interest.
5. Add $\delta E/n_p$ for different diffraction orders at each δE to obtain a total $\delta E/n_p$ which depends only on the photon energy and not on the diffraction order.
6. Find the number of diffraction orders, N,at each δE.
7. Calculate the enhancement factor F via $F = \frac{c}{Nd}\frac{\delta m}{n_p}$ and average it over the whole wavelength range of interest to find the average enhancement factor.

Logically, the speed of the method depend on the choice of δE, however, practically this is not a limitation for the simulations. Furthermore, because the enhancement factor is averaged over a broad spectral range, the method is not very sensitive to the choice of δE. Of course δE should be very smaller than the spectral range over which the average is taken.

In the second example, we obtain the enhancement factor of a 355 nm thick a-Si:H slab using both "idealized" and "real" models. Fig. 4.14 shows three curves based on the "real model". Two of these curves correspond to TE and TM polarization and the third one is their average.

Also a curve which is obtained by using the "idealized model" is plotted. For the ideal model only one curve is enough because in this model the film thickness does not depend on polarization. For all of these curves, material data of a-Si:H is used. As Fig. 4.14 shows, the real model provides higher enhancement values regardless of polarization. This is because of the increased effective thickness of the film which is considered in the "real model". Equivalently, this can be considered as the lower effective guide index compared to its physical refractive index. For incident angles smaller than 25°, TM polarized fields lead to larger enhancement factor values compared to the TE polarized fields. We will see later the same phenomenon in a complete solar cell stack.

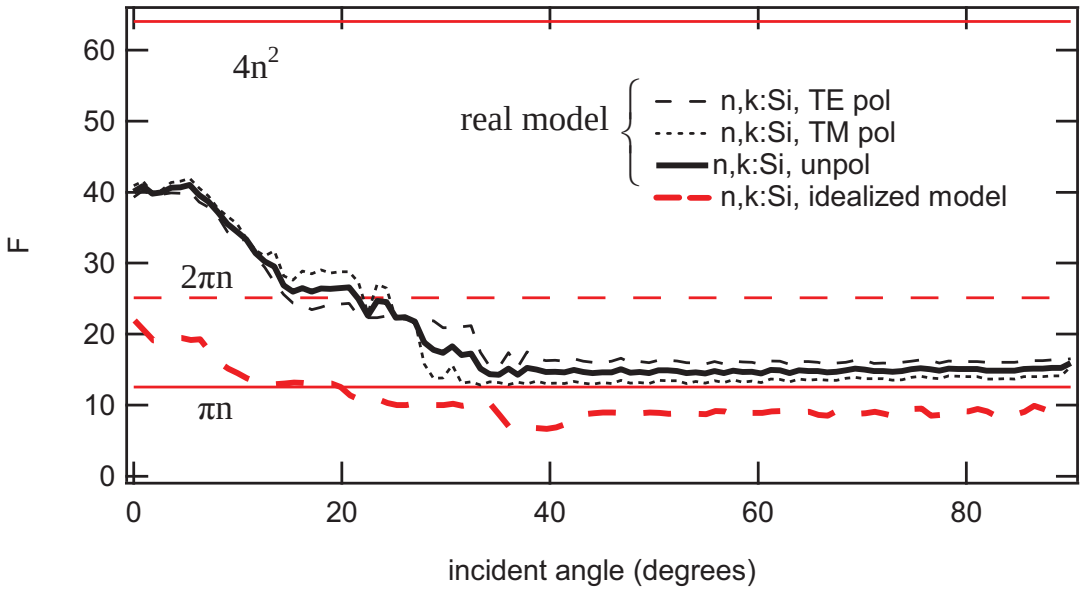

Figure 4.14: Enhancement factor of a dielectric slab averaged over the wavelengths from 600 to 900 nm obtained by the "real" and the "idealized" models as a function of incident angle for 1D gratings with a period of 560 nm. The horizontal lines represent the limit for 1D and 2D gratings. The other curves represent the enhancement factor for the 355 nm thick a-Si:H slab obtained with the idealized model (bold dashed red) and the real model in P polarization (dashed black), S polarization (dotted black) and the unpolarized case (bold black). For simplicity, on axis incidence is considered only.

4.3.5 Complete solar cell stack

For the next example, we calculate the maximal enhancement factor using the "real model" for a complete solar cell stack on a 1D grating substrate. The stack consists of 70 nm of ITO front contact, 15 nm of p-doped Si (p-Si), 180 nm of intrinsic a-Si (i-Si), 20 nm of n-doped Si (n-Si), 70 nm of ZnO and a silver back-reflector respectively from top to bottom. Because the cell consists of different materials, application of the bulk approximation (Eq. 4.17) may not be as clear as for a slab which consists of a single material. Furthermore, the bulk approximation ignores wave spread outside the film. We discussed in section 4.2.1 that instead of using the bulk refractive index n in Eq. 4.17, one should use the group index to incorporate

the modal properties of waves in the cell (Eq.4.21). For a structure with broad resonances, we assume the effective refractive index to be $n_{eff} = k_{\parallel}/k_0$ [82].

Fig. 4.15 shows the enhancement factor obtained for the cell through different models. Again the TE-polarized, the TM-polarized and the unpolarized results are presented. The enhancement factor of the complete cell is maximal at around normal incidence similar to the a-Si:H slab. However, the enhancement factor of the complete cell is smaller than the one of a-Si:H slab regardless of the incident angle. This can be because of the smaller refractive index of the complete cell compared to the a-Si:H slab. The latter discussion reveals a trade-off for thin-film solar cells: additional layers which act as buffer or anti-reflection coating can reduce the potential of the cell for absorption enhancement.

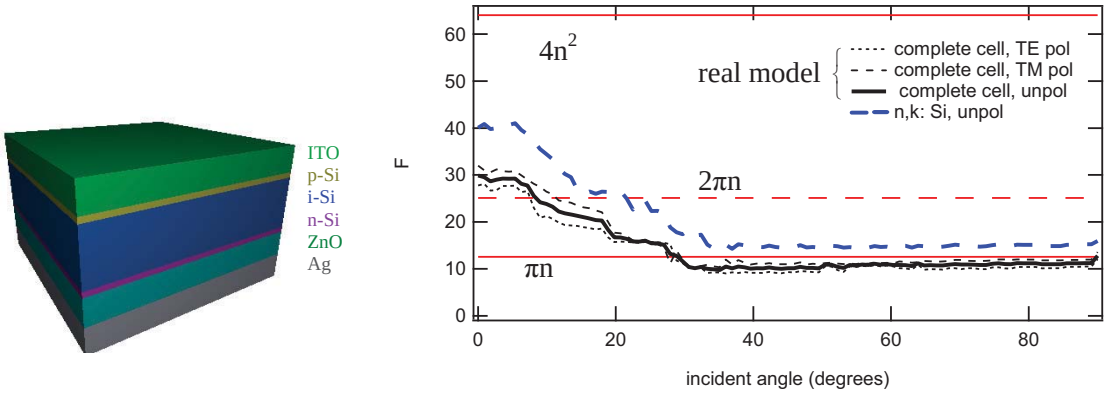

(a) (b)

Figure 4.15: (a): layers of the full functional solar cell stack including doped and contact layers. (b): Comparison of the average enhancement factor of the solar cell structure and a slab of a-Si:H as a function of incident angle for 1D gratings with a period of 560 nm. The horizontal lines represent the limit for 1D and 2D gratings. All of the other curves are obtained with the real model and they represent the enhancement factor obtained for the 355 nm thick a-Si:H slab under unpolarized illumination (bold dashed blue) and for the complete solar cell stack in P polarization (dotted black), S polarization (dashed black) and the unpolarized case (bold black). For simplicity, on axis incidence is considered only.

The two latter examples (Fig. 4.14 and Fig. 4.15) predict that the guided modes can enhance absorption further for TM polarization compared to TE polarization, especially at close-to-normal incidence. In Fig. 4.16 the phase Φ_{RPM} for the complete stack is plotted for both polarizations. Details about the definition of Φ_{RPM} and obtaining it is mentioned in section 4.3.3. In these diagrams, phase jumps show the existence of guided modes. Fig. 4.16 shows that phase variations are more considerable in TM polarization compared to TE polarization. This means a higher density of modes and potentially higher absorption enhancement by guided modes for TM waves.

Two factors affect the guided-mode excitations: material absorption (γ_i) and external cou-

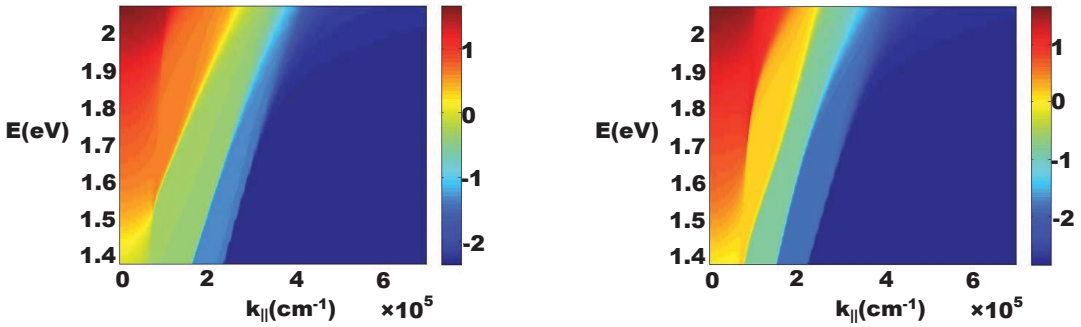

Figure 4.16: ϕ_{RPM}/π versus $k_{\parallel}$ (cm^{-1}) and energy (eV) in TE (left) and TM (right) polarization for a complete solar cell stack. Each mode is associated with a jump of about unit in these graphs.

pling (γ_e) to the other modes due to perturbation of the guided wave structure. The guided modes are associated to resonance peaks/dips or jumps in a corresponding quantity e.g. the absorption or the reflection phase. The quality factor of the resonance is determined by material absorption and external coupling. A high quality factor demonstrates that the energy which is coupled to a resonance can hardly couple outside, and neither is it absorbed in the structure. Therefore, the quality factor of the resonance ($\frac{f}{\Delta f}$) shows the capability of a resonance to trap photons. Of course this is not desired for absorption enhancement in solar cells as already discussed. Exchange of energy with the outside medium and internal absorption broaden the resonances. In the phase diagrams of Fig. 4.16 this appears as blurring of the diagram which reduces abruptness of the phase discontinuities corresponding to guided modes. In this way, blurring of the diagram at high energies is understood by high absorption of materials.

4.3.6 2D gratings: square and hexagonal periodicity

In this part we investigate the angular dependence of the upper bound of the absorption enhancement factor for 2D gratings. The method is similar to the procedure that we already explained for 1D gratings. The major difference is that the Bragg condition becomes more complex for 2D gratings because the reciprocal lattice will be two dimensional. This makes the mode counting procedure more complicated. The mode counting procedure depends on the symmetry of the two dimensional lattice e.g. hexagonal or square. Fig. 4.17a and b show the enhancement factor for the case of a 2D grating with square geometry. The grating period is 560 nm in both x and y directions. To change the incident angles, we consider two angles θ and ϕ which define the incident wave-vector direction as

$$\hat{k} = \left|\hat{k}\right| (\sin\theta\cos\phi\hat{x} + \sin\theta\sin\phi\hat{y} + \cos\theta\hat{z}) \tag{4.36}$$

The enhancement factor is plotted as a function of θ and ϕ in Fig. 4.17. The polar direction

corresponds to the θ axis and the azimuthal direction is related to ϕ. Because many mode excitations can occur in this case, the maximal enhancement factor for 2D gratings can surpass the $4n^2$ limit in both the real and the idealized model. As previously observed for 1D gratings, the enhancement factor is larger when the real model is applied. This effect is especially observed close to normal incidence. The reason is the smaller refractive index for the real model as previously explained for 1D gratings.

Fig. 4.17 indicates also that the enhancement factor shows an anisotropic behavior. It is rather strong along the sides of the Brillouin zone. The Brillouin zones of the square lattice and the hexagonal lattice geometries are depicted in Fig. 4.17c. Fig. 4.17d shows the enhancement factor for a 2D grating with hexagonal geometry with a lattice constant of 560 nm. The enhancement factor of the cell based on the hexagonal lattice takes larger values at close-to-normal incidence similar to the square geometry. The hexagonal lattice shows a rather isotropic behavior compared to square lattice. Therefore, by using hexagonal geometry one can reduce the azimuthal angular dependence of the photocurrent of a solar cell.

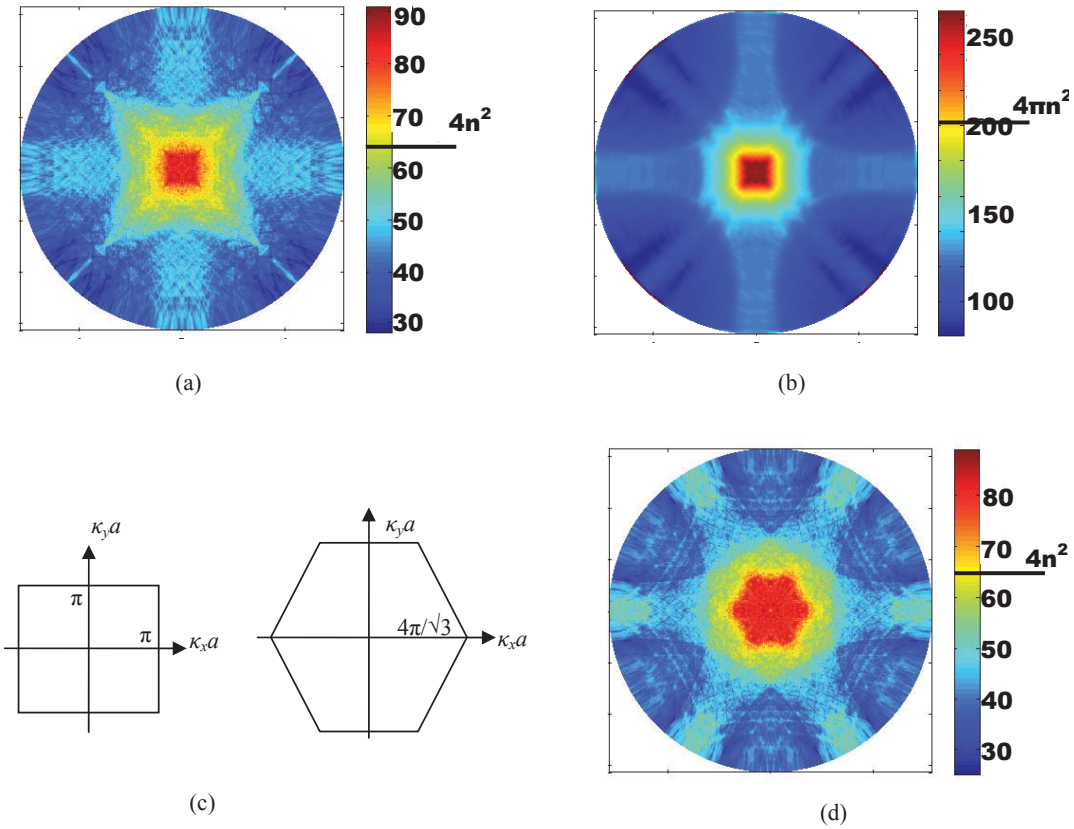

Figure 4.17: Top: angular variation of the average enhancement factor under unpolarized light obtained with the “idealized” (a) and the “real” (b) models for the square lattice. The radius represents θ and the angle shows the corresponding ϕ. Bottom: Brillouin zones for the square lattice and triangular lattice geometries (c) and angular variation of enhancement factor obtained with the "idealized" model for the triangular lattice (d).

To summarize, thin films can provide high enhancement factors if they are optimized. To obtain the enhancement factor of thin films, we should take into account penetration of the wave into air and supporting layers. This penetration of the wave compresses the optical bands. In a real device, the existence of layers with low index can reduce the enhancement factor. TM polarization provides higher enhancement factor than TE polarization. Finally, 2D periodic thin film devices can potentially surpass the $4n^2$ limit over a wide spectral range.

It is worth mentioning that although the enhancement factor is widely used in literature, its application to compare solar cells can be misleading. To obtain the enhancement factor we normalized absorption to the single pass absorption. Therefore, a small value of single pass absorption can lead to a large enhancement factor which does not necessarily correspond to remarkable enhancement in the absolute absorption value and thus, does not contribute effectively to the corresponding cell's photocurrent.

4.3.7 Impact of field overlap: practical limit

Spread of the wave outside the cell has different effects on the enhancement factor. First, it increases the effective thickness of the cell. Second, it means that the wave cannot be fully absorbed in the cell. Therefore the enhancement factor is less than the values predicted previously.

Even if the wave is totally confined to the cell, absorption does not occur only in the i-Si layer. Absorption in other layers is mainly lost in the cell and does not count in the enhancement factor.

Previously, Stuart and Hall have discussed the impact of a wave's spread outside the cell [30]. For cells made of high index absorber materials such as silicon, this effect is marginal as shown in section 4.2. Also, some part of the absorption which occurs in the cell is parasitic because it occurs in the layers of the cell with a high recombination rate. To distinguish this kind of absorption from the absorption which happens in the i-Si layer and thus contributes to photocurrent, we define the "absorption overlap" as the ratio of the absorption in the active layer of the cell to the absorption integral of the whole cell.

$$\eta_{abs} = \frac{\int_{i-Si} \epsilon_i |\mathbf{E}|^2 \, dV}{\int_{cell} \epsilon_i |\mathbf{E}|^2 \, dV} \tag{4.37}$$

where dV indicates the volume element. The absorption enhancement factor should be modified to take into account the absorption overlap.

$$F_{eff} = \sum_i \eta^i_{abs} F^i \tag{4.38}$$

where the index i is used to distinguish different resonances. The modification of the enhancement factor in Eq. 4.38 is general and not restricted to a special geometry. To evaluate it, the electric field of the mode for different energy and propagation constants is required to allow calculation of the field overlap. As primarily we assumed that the structure is a slight deviation from a planar geometry, field profiles can be approximated with the profile of a flat one. Furthermore, for each resonance, the guided-mode profile at the correspondence resonance peak can be used.

Imperfect confinement of the wave energy to a cell and parasitic absorption over the different layers of the cell reduce the enhancement factor in both thick and thin cells. However, one should note that high confinement of a mode does not necessarily result in a high amount of absorption enhancement by the mode. For example, a plasmonic mode which is localized at the metal-dielectric interface can lose a major part of its energy in the metal; therefore, its η_{abs} and F_{eff} are small. Absorption in the metal is a major challenge of applying plasmonics to thin-film solar cells [110].

Fig. 4.18 demonstrates the effect of the absorption overlap on the enhancement factor of the complete solar cell described in section 4.3.5 where a $1D$ grating coupler with $P = 560$ nm is used. The "absorption overlap" reduces the enhancement factor to almost its half. This shows that parasitic loss is a major constraint for absorption enhancement in thin-film solar cells.

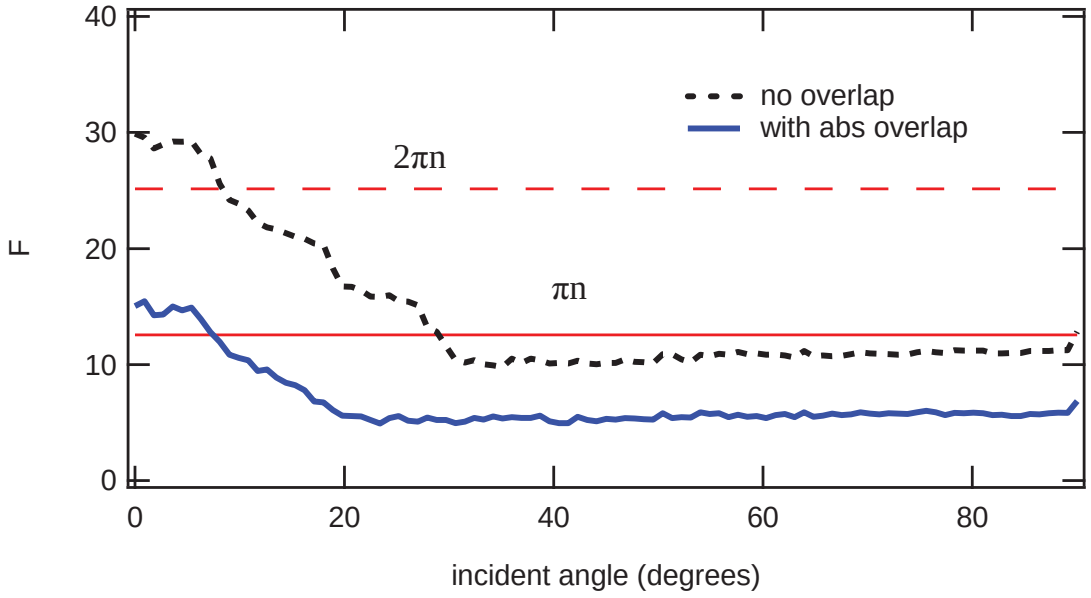

Figure 4.18: Effect of loss on the average enhancement factor of the full solar cell stack with 1D grating coupler ($P = 560nm$) under unpolarized illumination. The curve with "no overlap" is the benchmark where modification of relation (5) is not applied. The "with abs overlap" corresponds to the case where this modification is applied. For simplicity, on axis incidence is considered only.

4.3.8 Practical considerations

Up to now we have obtained the average absorption enhancement factor over the wavelength range from 600 to 900 nm. What finally matters for a solar cell regarding absorption is its photocurrent. In this part we calculate the maximal increase in the short circuit current density (J_{sc}) over the same wavelength range provided by guided modes. For this aim, we first obtain the absorption via $A = F\alpha d$. Then we calculate the increase in J_{sc} by weighting the absorption with the photon flux of the solar spectrum and integrate over the range of interest. This approximation is better than the simple averaging of the enhancement factor over the wavelengths of interest because it considers the solar spectral density also. Figure 4.19 shows the increase in the short circuit current density (ΔJ_{sc}) under unpolarized illumination versus the incident angle for the complete solar cell stack on a 1D grating coupler with P = 560 nm. The dotted curve shows ΔJ_{sc} where the absorption overlap is not considered ($\eta_{abs} = 1$), i.e. where it is assumed that the wave is fully confined to the i-Si layer. This curve shows that if absorption occurs only in the i-Si layer, the guided modes can increase the photocurrent at most by 2 mA/cm^2. Maximal photocurrent increase occurs for close to normal incidence. If we consider η_{abs} too, we obtain the solid curve. This curve takes into account the imperfect confinement of the wave to the i-Si layer. The maximal photocurrent increase is obtained still for close-to-normal incidence. In this case, photocurrent increase is limited to 1 mA/cm^2. This confirms once more the undesirable effect of parasitic absorption. Note that the value of J_{sc} provided by the single-pass absorption over the considered wavelength range is 0.0174 mA/cm^2 which is much smaller than the potential J_{sc} enhancement provided by the guided modes even assuming parasitic loss over the other layers of the cell.

It is worth mentioning that usually a cell is encapsulated beneath a planar glass sheet. In this case the incidence on the glass-ITO interface will be limited to an angular range close to normal, between normal and critical angle of glass (almost 42 degrees). The glass layer also affects the polarization of the incident light. It even modifies the whole dispersion diagram of the multilayer stack. However, the angular dependence of F and ΔJ_{sc} should not be much different from the case without glass at least qualitatively. The reason is that F depends on both of the incident angle and the refractive index of the incident medium. Limiting the incidence to small angles by increasing the refractive index of the incidence medium does not increase F due to the radiance theorem. To study more complex effects e.g. polarization, the dispersion diagram of the structure including the glass layer should be used.

Despite the tight dependence of absorption enhancement on a cell's layers, some guidelines for the design of interface textures can be concluded. In general, 2D gratings or random patterns are preferred to 1D gratings for interface texturing because they support a larger number of mode excitations. Specifically 2D gratings with hexagonal geometry can support more resonances and reduce the angular dependence of the absorption enhancement factor compared to the square geometry.

Apart from the mentioned points, the method which we used to obtain the dispersion dia-

gram can be used to analyze guided modes in thin-film solar cells. This technique can help engineering the guided modes for a cell with an arbitrary number of layers and materials, which can be an initial but important step in the design of textured solar cells.

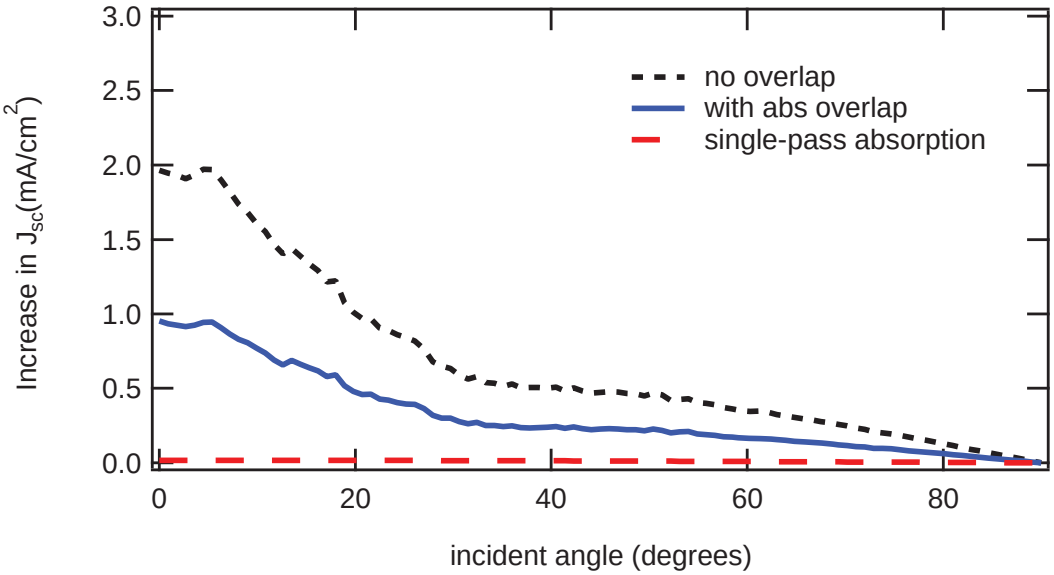

Figure 4.19: Angular dependence of photocurrent increase for the full solar cell stack with a 1D grating coupler with P=560 nm under unpolarized light. The curve with "no overlap" is where modification of Eq. (5) is not applied. The "with abs overlap" corresponds to the case where this modification is applied. For simplicity, on axis incidence is considered only. The horizontal line corresponds to the photocurrent provided by single-pass absorption.

4.4 Limit of light coupling strength in solar cells

4.4.1 The limit imposed by single-pass absorption

As already mentioned in the previous sections, enhanced light absorption is a requirement to realize cost-effective photovoltaics. To absorb light more efficiently, solar cells should be designed such that the incident light is coupled into them as strongly as possible [111, 112, 113, 114, 76, 115, 116]. This can be in turn achieved by excitation of guided modes. [117, 40, 36, 118, 44].

The extent to which guided modes can boost absorption in a solar cell depends on two main factors:

1. Number of resonances: Absorption is enhanced more if a higher number of resonance excitations is combined with few reflected orders.
2. Coupling strength: Stronger coupling to external radiation means a higher amount of absorption enhancement.

Often in the literature, only the number of modes —or equivalently their density— is considered, which assumes that coupling is so efficient that it does not affect calculations [29, 30, 20, 109]. To provide more accurate values for the maximal absorption enhancement, coupling strength of the modes should be considered as well.

In this part, an upper limit is derived for the coupling strength of the modes of a thin film to the outside radiation. For simplicity, only guided modes are considered here but radiation modes can be treated similarly. A grating coupling mechanism is assumed to excite guided modes. Also, the cell is periodic along the grating periodicity. Here, I show that the maximal coupling rate depends on the film thickness and its modal structure. The formulation mentioned here does not depend on the choice of grating texture, therefore, random textures may be analyzed analogously.

We start from Eq. 4.5 and we assume that an incident wave travels through the film. If the wave couples to a guided mode during its travel through the film, it also decouples from the mode at the end of this travel. If for simplicity the number of output ports $N = 1$, for example if a back-reflector is put underneath the film, the coupling rate is the same for both in-coupling and out-coupling. A mean time of τ_e is required for each coupling. Therefore, the whole travel time will be $2\tau_e$; one τ_e for coupling in and one τ_e for coupling out. The minimum travel time of a wave inside the film determines the minimum of τ_e and the maximum of γ_e. I verify this intuition by using the temporal coupled-mode theory.

The maximum absorption A in the film can be calculated from Eq. (4.9) [18, 20]:

$$\begin{aligned} A &= \left.\frac{\gamma_i |a|^2}{|S|^2}\right|_{\omega=\omega_0} \\ &= \left.\frac{\gamma_i \gamma_e}{(\omega-\omega_0)^2 + \left(N\frac{\gamma_e}{2} + \frac{\gamma_i}{2}\right)^2}\right|_{\omega=\omega_0} \\ &< \frac{4\gamma_i}{N^2\gamma_e}, \end{aligned} \tag{4.39}$$

Therefoe γ_e has an upper limit:

$$\gamma_e < \frac{4\gamma_i}{N^2 A} \tag{4.40}$$

Based on Eq. (4.40), there is a trade-off between the absorption and the coupling rate that eventually limits both of them. Higher absorption values represent lower coupling rates and vice versa. This shows that in the weakly absorbing regime of solar cells, guided modes can be coupled more strongly to external radiation. One should take the minimum possible value of absorption not to underestimate coupling strength. Let us assume that the wave passes through the film only once so that the absorption over this one-pass length along the film L

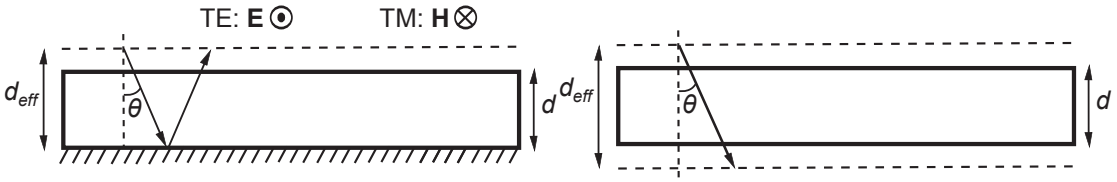

(a) (b)

Figure 4.20: Schematic of an incident wave transiting a dielectric film under an angle θ. The effective and the physical thickness of the guide are indicated by d_{eff} and d. (a) The film on a back reflector, (b) The film in air. In TE/TM polarization, electric/magnetic field is normal to the incidence plane.

is the minimum of absorption [82]:

$$A \approx \frac{\gamma_i}{v_g} L. \tag{4.41}$$

where v_g is group velocity of the mode at resonance. From Eqs. (4.40) and (4.41) one concludes that

$$\gamma_e < \frac{4 v_g}{N^2 L} = \frac{4}{N^2 \tau_t}. \tag{4.42}$$

Here $\tau_t = L/v_g$ is the wave travel time while passing through the film. For only one reflection order at the presence of back-reflector($N = 1$), Eq. (4.42) and $\gamma_e = 2/\tau_e$ lead to $\tau_e > \tau_t/2$, which is consistent with our initial intuition that $\tau_{e,min} = \tau_{t,min}/2$. Because τ_t depends on the modal structure of the film, the order of the mode to which the light couples and the cell thickness, γ_e is related to these parameters similarly. Specifically, thin-film devices should support stronger coupling compared to thick devices because they let τ_t become very small. Also, it should be possible to excite modes more effectively close to the light line of air because their group velocity is large.

For the first example, let us consider a dielectric film of thickness d and index n between a half space of air and another half space of perfect reflector as shown in Fig. 4.20a. Also assume that the guided modes of the slab are coupled to external radiation by interface texturing. An incident wave coming from the air side couples to a guided mode of the film associated with the internal reflection angle θ. The back-reflector affects the coupled mode equation in two ways; first, it makes the incident wave pass through the film twice. Second, it decreases the number of output ports to one. Based on Eq. (4.42) we can thus write [107]

$$\gamma_{e,max} = \frac{4 v_g}{2d \tan\theta} = \frac{2 v_g}{d} \frac{\sqrt{n^2 - n_p^2}}{n_p}. \tag{4.43}$$

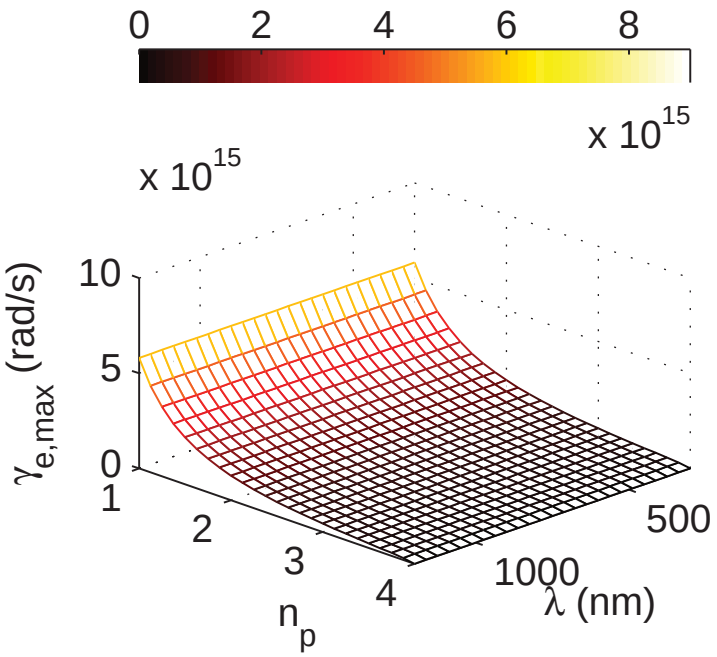

Figure 4.21: $\gamma_{e,max}$ obtained by using the phase velocity approximation in Eq. (4.43) versus wavelength (λ) and phase index (n_p) for a slab with $n = 4$ and $d = 200$ nm.

Here $n_p = {}^{c}/_{v_p}$ is the phase index where v_p is the phase velocity and c is the speed of light in air. In Eq. (4.43) we consider d and not the effective thickness of the film, d_{eff} [107], because absorption occurs only inside the waveguide.

An important point is the appearance of film thickness in the denominator of Eq. (4.43), which reveals an advantage for thin films; they allow strong mode excitation. The problem with thin films might be that the wave is not confined to them but if the mode is extremely confined, e.g. a surface plasmons, the small thickness of the film will guarantee efficient coupling of light and the high confinement of the mode insures that the mode is absorbed efficiently in the film [119, 120, 121]. The group velocity and the phase index also influence $\gamma_{e,max}$ in Eq. (4.43) but both maximize it on the light line of air. The maximal coupling rate of a film with one reflection order and a perfect back reflector occurs at $n_p = 1$ and it is equal to $2c\sqrt{n^2-1}/d$.

As a second example, consider a film suspended in air (as in Fig. 4.20b). Due to the elimination of the back reflector, this system has two ports ($N = 2$) and the incident wave passes through the film only once. For simplicity, we assume that both sides of the film have the same coupling characteristics. Eq. (4.42) suggests that

$$\gamma_{e,max} = \frac{4v_g}{(2)^2 d \tan\theta} = \frac{v_g}{d}\frac{\sqrt{n^2-n_p^2}}{n_p}. \tag{4.44}$$

Figure 4.21 shows the maximum coupling rate $\gamma_{e,max}$ for a film with refractive index $n = 4$ and thickness $d = 200$ nm as a function of the incident wavelength and the phase index n_p. The wavelengths correspond to the range of operation of solar cells. The refractive index and the thickness are chosen such that structure resembles a thin-film amorphous silicon solar cell. In Fig. 4.21, we have applied the approximation of using the phase velocity instead of the group velocity in Eq. (4.44) to obtain $\gamma_{e,max}$ regardless of polarization and band shape in the dispersion diagram. Therefore, Fig. 4.21 is plotted as a continuum and the bands should be mapped on it. The maximum of $\gamma_{e,max}$ occurs on the light line of air ($n_p = 1$) and it is equal to $c\sqrt{n^2-1}/d$ which is half of the value obtained in the previous example (Eq. (4.43)). Therefore, adding a back-reflector is beneficial not only to increase the path length of light inside the film, but also because it allows stronger coupling. In this way, a solar cell's back-reflector boosts the absorption of light in the cell which in turn increases the short-circuit current density and the open-circuit voltage, and consequently the efficiency [17].

Figure 4.22a and 4.22b show $\gamma_{e,max}$ in logarithmic scale for the same film ($n = 4$ and $d = 200$ nm) along the bands in the dispersion diagram in transverse electric (TE) and transverse magnetic (TM) polarizations. In TE polarization, the electric field is normal to the incidence plane (c.f. Fig.4.20). For these calculations, Eq. (4.44) was used with the group velocity ($v_g = d\omega/d\beta$). In both polarizations, $\gamma_{e,max}$ is maximum at the onset of the modes on the light line of air. Starting from this line and moving along the bands, $\gamma_{e,max}$ decreases in agreement with the phase index approximation of Fig. 4.21. At fixed energy or propagation constant, higher-order bands provide larger $\gamma_{e,max}$ because they correspond to smaller n_p. Specifically, the TE_2 and the TM_1 modes emerge from the light line of air in the energy range where amorphous silicon is weakly absorbing, so, they have extremely high $\gamma_{e,max}$ in this range. Note that very close to the light line of air guided modes are weakly confined to the cell, so they cannot lead to significant absorption enhancement despite their strong excitation. Nevertheless, it should be possible to find a region of optimal parameters in the dispersion diagram such that both the coupling rate and the mode confinement have reasonably high values. One might consider this in the design of solar cells.

In summary, we derived a limit for the rate of light coupling into the modes of solar cells. This limit depends on the thickness of the cell, the group velocity of the mode, and where in the dispersion diagram the mode is excited. We showed a trade-off between absorption in the cell and the coupling rate. Therefore, calculations of the maximum absorption enhancement in solar cells should be modified to consider this constraint. We applied our approach to solar cells but it can be used to provide limits and design guidelines for a broad variety of devices whose operation is based on resonant phenomena.

4.4.2 The limit imposed by Planck's law

Planck's law gives the maximum energy that can be emitted from an object at a temperature T as a function of wavelength. Assume a square cell with an area L^2. For simplicity consider also

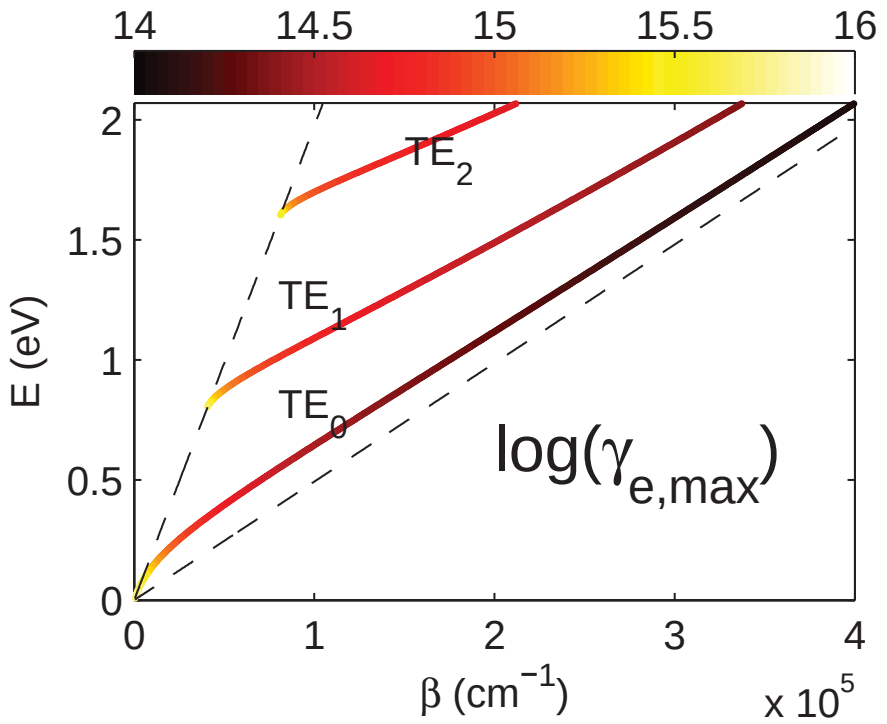

(a)

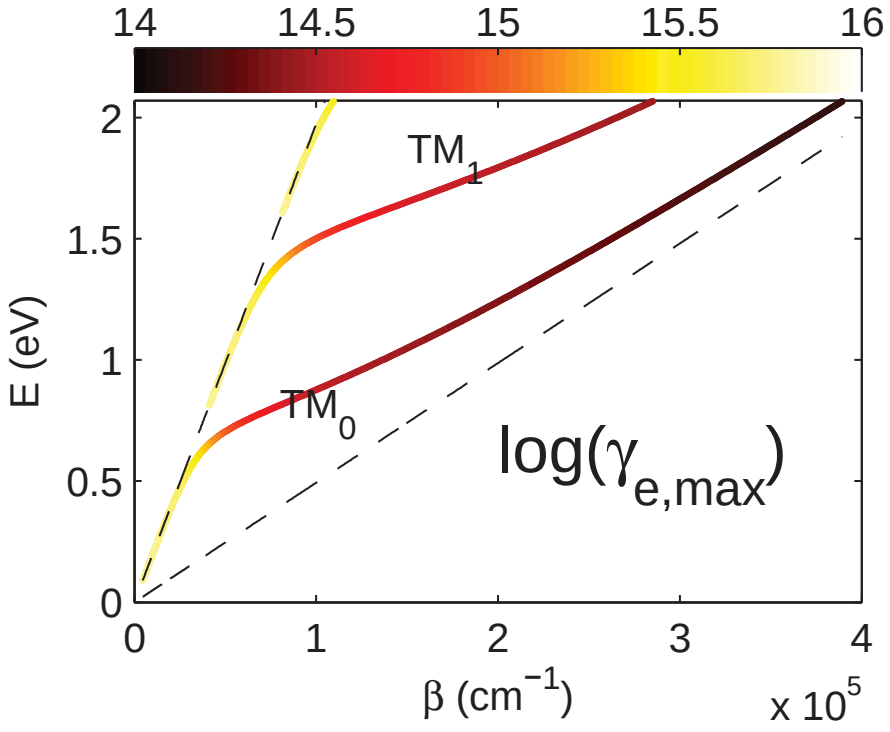

(b)

Figure 4.22: $\log_{10}(\gamma_{e,max})$ for a slab with $n = 4$ and $d = 200$ nm for (a) TE polarization and (b) TM polarization. The dashed lines show the light lines of air and the dielectric. The unit of $\gamma_{e,max}$ is rad/s.

that periodic boundary conditions can be applied and that there is a perfect back-reflector at the back of the cell so that light-coupling occurs only from the top interface of the cell. The sum of the external coupling rates of the optical modes of the cell in the angular frequency range $[\omega, \omega + \Delta\omega]$ has an upper bound [88].

$$\sum_m \gamma_m \leq \left(\frac{L}{2\pi c}\right)^2 \omega^2 \Delta\omega \tag{4.45}$$

where c is speed of light in air and m is mode index. If we also assume that all the modes have the same coupling characteristic $\gamma = \gamma_m$, Eq. 4.45 becomes

$$\gamma \leq \frac{c}{4d} \frac{\rho_{vac}}{\rho} \tag{4.46}$$

where ρ and $\rho_{vac} = \omega^2/(\pi^2 c^3)$ are the density of optical modes (states) in the cell and in air and d is the cell thickness. Two very important points can be concluded here. First, by increasing the density of states it is possible to increase absorption and second, by reducing a cell's thickness, it can be possible to push the upper bound of coupling to larger values.

At thermal equilibrium, the rate of photon emission in the angular frequency range $[\omega, \Delta\omega]$ at temperature T for each optical mode can be expressed as

$$p_m = \frac{\gamma_m}{\exp(\hbar\omega/k_B T) - 1} \tag{4.47}$$

where k_B is Boltzmann's constant. Based on Planck's formula for blackbody radiation, the rate of photon emission from the blackbody of surface area L^2 at temperature T is equal to

$$B = L^2 \left(\frac{\omega}{2\pi c}\right)^2 \frac{\Delta\omega}{\exp(\hbar\omega/k_B T) - 1} \tag{4.48}$$

Kirchheoff's law bounds the emission rate to the blackbody radiation, thus,

$$\sum_m p_m \leq B \tag{4.49}$$

This puts an upper limit on the external coupling rate. More detailed calculation can be followed in [88]. From the mentioned formulation, it appears that regardless of the texture geometry, the sum of coupling coefficients has an upper bound. Thus, stronger excitation of some modes may be at the expense of weaker excitation of the other ones. This seems to be not far from reality for a-Si solar cells.

4.5 Limits on efficiency

The upper bound of efficiency has been determined by Shockley and Queisser [32] for a p-n junction. To obtain this limit, they considered that the band gap of the semiconductor is in the form of a step function and that each photon can create one free carrier at most. Also they assumed a description in terms of blackbody radiation. This efficiency limit is about 33 percent. Different methods have been proposed to overpass this limit, the most relevant of which to this work is making tandem cells [33]. Here we briefly go over the argument of Shockley and Queisser to obtain this limit.

4.5.1 The Shockley-Queisser limit

In 1961 Shockley and Queisser wrote a key paper [32] about the limit of efficiency in a solar cell based on a single p-n junction. Their paper uses the laws of thermodynamics and the principle of detailed balance. Here we briefly show a potential for passing their limit.

Assume that each photon with an energy larger than the band gap of the absorber generates only one electron-hole pair. Power absorbed by the cell is equal to

$$P_{output} = h\nu_g A Q_s \tag{4.50}$$

where ν_g is the frequency corresponding to the band gap of the semiconductor, and Q_s denotes the number of quanta of frequency greater than ν_g incident per unit area per unit time for black-body radiation at temperature T_s and it can be obtained by using Planck's formula

$$Q_s = \left(\frac{2\pi}{c^2}\right)\int_{\nu_g}^{\infty} \frac{\nu^2 d\nu}{\exp(h\nu/kT_s)-1} \tag{4.51}$$

The incident power is equal to

$$P_s = \left(\frac{2\pi h}{c^2}\right)\int_{0}^{\infty} \frac{\nu^3 d\nu}{\exp(h\nu/kT_s)-1} \tag{4.52}$$

the efficiency limit can be thus approximated as a function of absorber band gap

$$u(\nu_g) = \frac{h\nu Q_s}{P_s}\frac{\int_{\nu_g}^{\infty} \frac{\nu^2 d\nu}{\exp(h\nu/kT_s)-1}}{\int_{0}^{\infty} \frac{\nu^3 d\nu}{\exp(h\nu/kT_s)-1}} \tag{4.53}$$

This is the ultimate limit of efficiency in a solar cell with band gap frequency of ν_g.

Shockley and Queisser further extended their calculations by considering that the maximal radiation by a cell at a temperature of T_c is described by Planck's formula. Similar to Eq. 4.51 they defined Q_c corresponding to radiation from the cell as defined below.

$$Q_c = \left(\frac{2\pi}{c^2}\right)\int_{\nu_g}^{\infty} \frac{\nu^2 d\nu}{\exp(h\nu/kT_c)-1} \tag{4.54}$$

They furthermore took into account the exponential dependence of carrier generation and recombination processes as a function of internal potential. Based on the amount of the net generation rate (equivalently net recombination), they obtain limits for the efficiency of a solar cell which are lower than the values predicted by Eq. 4.53

In summary, in this chapter limits of light absorption enhancement for thin-film solar cells were studied. For this purpose we extended the coupled-mode theory to the case of thin-films with periodic texture. Since it was assumed that the guided modes are excited very strongly, the calculations of this chapter are useful to obtain the upper bounds of absorption in a solar cell. We showed in this chapter that imperfect confinement of light to the absorber layer can decrease the absorption enhancement. Specifically, parasitic absorption can decrease the enhancement factor dramatically. We furthermore studied the effect of the incident angle on absorption enhancement. We found that absorption can be large for oblique incidence. We also compared 2D gratings based on square and hexagonal geometry and we showed that hexagonal structure can enhance absorption more isotropically. We furthermore presented an upper bound for the coupling-strength of light to the guided modes of a multilayer device such as a solar cell. This limit can also be used for other similar opto-electronic devices such as light emitting diodes.

5 Guided waves in solar cells

5.1 Introduction

One approach to enhance light absorption in a solar cell is to improve the cell morphology. Usually a solar cell is an almost-planar multilayer device. There are thus two main methods to modify its geomtry: texturing the interfaces and changing the sequence of the layers. Of course additional approaches such as placing dielectric or metallic nano-particles [122] or photonic crystals can be applied [123, 124] but these methods can be ususally considered as extensions of the two mentioned techniques or a combination of them.

Based on theoretical considerations, it was suggested that periodic interfacee textures should be more efficient than random ones [20]. However, random textures are normally preferred in practice due to ease of fabrication. Regardless of whether it is random or periodic, the surface texture couples the incident light into the modes of the cell. Strength of this coupling can depend strongly on the texture morphology and finding textures which can improve light coupling to the modes of the cell has been investigated recently by many authors [125, 126, 127, 128, 129].

Layers of a cell provide a new degree of freedom to improve light absorption in it. If the cell is made only of dielectric materials, it will support just guided modes which are confined mainly to the cell, although their confinement is not perfect and a part of the mode energy can extend outside the cell in air. Contrarily, if the cell consists of metals too, it will probably support “plasmonic modes" which are localized at the metal-dielectric interface. Here, by guided modes", we refer to the non-plasmonic modes although actually plasmonic modes are guided modes too. Plasmonic modes can provide more light confinement than guided modes, and seem theoretically a promising route towards efficient light trapping even beyond the conventional ergodic limit [30]. Despite the interesting optical properties of plasmonic modes and their theoretical promise to improve photovoltaics [119, 130, 25, 131], fabrication of high quality metallo-dielectric interfaces is still a practical challenge. A major problem is the high amount of parasitic absorption in the metal and recombination of carriers at the metal-dielectric interface.

On the other hand a back-reflector at the bottom of the cell reflects the incident photons after they pass the cell and gives them another chance to be absorbed, thus it increases absorption [29]. Also, it enhances the coupling strength of the modes [84]. A highly reflective metal e.g. Ag seems an appropriate choice of material for the back-reflector. However, a Ag back-reflector may support a plasmonic mode which is mainly absorbed at the vicinity of the silver surface. If a spacer layer is deposited on the silver layers, it shifts the plasmonic mode to higher energies (frequencies eventually), converting it to a a guided mode in the wavelength range of interest [40]. This is only one example of modifying the sequence of layers in the cell to enhance light trapping. One can consider other modifications of this sequence as a degree of freedom. Adding new layers, removing the existing layers and changing the layer thicknesses are examples of other geometrical changes which have a potential for improving light absorption in the cell.

In this chapter we explain the mechanism of absorption enhancement by guided modes in thin-film a-Si solar cells. To take into account the effect of layers sequence on the optical resonances in a cell, we use the dispersion diagram of the cell assuming that the cell is in the form of a planar multilayer. This allows us to study the nature of modes in the cell and to judge whether they are guided or plasmonic. The flat-interface model helps us also to study the impact of changing the thickness of a specific layer, e.g. the spacer layer or its consisting material. Then, the effect of texture on absorption enhancement is studied. For simplicity, we consider only one- dimensional (1D) gratings in a major part of this contribution except the last part where we compare 1D and 2D gratings. Note that a 1D grating is actually a 2D structure. It is usually expected that asymmetric textures in the form of blazed gratings can enhance absorption in a cell maximally. This is previously predicted by coupled-mode approximation [132] and also by rigorous calculations [133]. We consider three different geometries and we show that depending on texture parameters, a symmetric pattern may be able to improve light abosrption in the cell more than an asymmetric pattern especially when angular changes of photocurrent are considered. Unfortunately, solar cells literature often deals with normal incidence of light in a cell. We show that it is necessary to investigate other incident angles too, because a texture which seem non-optimal at normal incidence may outperform another texture which has a higher photocurrent under normal illumination. We also consider the effect of changing the spacer layer material (which is between the Ag and the n-Si layer) to verify the predictions of the planar model. Finally, we compare 1D and 2D gratings with an experimental sample and we discuss the extent to which texturing can enhance absorption in the cell.

The arrangement of the chapter is as follows. In section 5.2, different limitations on absorption enhancement in a solar cell are discussed briefly. To show the impact of guided modes in real thin-film Si cells, in section 5.3 we present a fabricated a-Si cell based on a 1D grating pattern. The cell shows improved absorption at long wavelengths thanks to the excitation of guided modes. The rigorous simulation of the cell provides results which correspond closely o the experimentally-obtained absorption. The planar model is then used in section 5.4 to investigate the impact of the back-reflector on modal structure of the solar cell. The effect

of both thickness and material of the spacer layer is studied in this respect. Section 5.5 is devoted to comparison of different textures and studying their angular response. Symmetry of the texture, grating depth and the effect of the spacer material on the EQE of the different textures are investigated in section 5.5. Finally 2D gratings are considered in section 5.5.3.

5.2 Physical limitations on coupling

Interface texturing plays a major role in coupling solar radiation to the guided modes of a solar cell. In the ideally planar structures, the guided modes are fully trapped inside the cell so their energy cannot couple outside. This may seem beneficial at the first glance since once light is inside the cell, its energy can be fully absorbed at least theoretically. However, due to Kirchhoff's law, in-coupling and out-coupling processes are reciprocal i.e. their coupling coefficient for in- and out-coupling are equal. This means that if the guided modes and the outside radiation are not coupled, there is no light to trap by the guided mode and to absorb. However if the guided mode is slightly coupled to the external radiation, the photons which couple in, are almost perfectly trapped and hence absorbed nearly completely. Another scenario is when coupling is strong. In this case, light can get inside the cell easily but it can couple out and escape easily too. This introduces a fundamental trade-off between in- and out-coupling in the cell. A major question is whether the coupling should be high or low to maximize absorption. Recently, it was demonstrated that in the weak absorption limit, maximal coupling is an essential to realize higher absorption [20].

Another physical limitation is imposed by Planck′s law of radiation [88]. Due to Planck′s law, the maximal electromagnetic emission (or equivalently absorption) by an object is limited to Black body radiation. This limits the magnitude of the coupling coefficient of guided modes. Regardless of the number of guided modes, their coupling coefficients are limited such that their total emission is under the radiation of a Black body at the temperature of the cell.

While Planck′s law describes a limit for the coupling strength, however it does not determine the exact value of coupling. Coupling strength is determined by both the layers of the cell and the exact shape of the interfaces. Therefore, it seems at least hard to define a general easy-to-calculate formula for the coupling strength if possible at all. Recently, remarkable effort has been spent over optimization of the interfaces of the solar cells to enhance coupling [134, 44, 135, 136]. However, little has been studied on the impact of cell thickness on coupling strength. Nevertheless, it has been recently shown that coupling strength also depends inversely on the cell thickness [88, 84]. This puts another limitation on coupling and emphasizes again the importance of studying the dispersion of the planar device.

5.3 An example: Absorption enhancement in an a-Si cell

To show the importance of guided mode excitation for absorption enhancement, thus photoucurrent and efficiency increase in thin-film solar cells, we fabricated an a-Si cell which

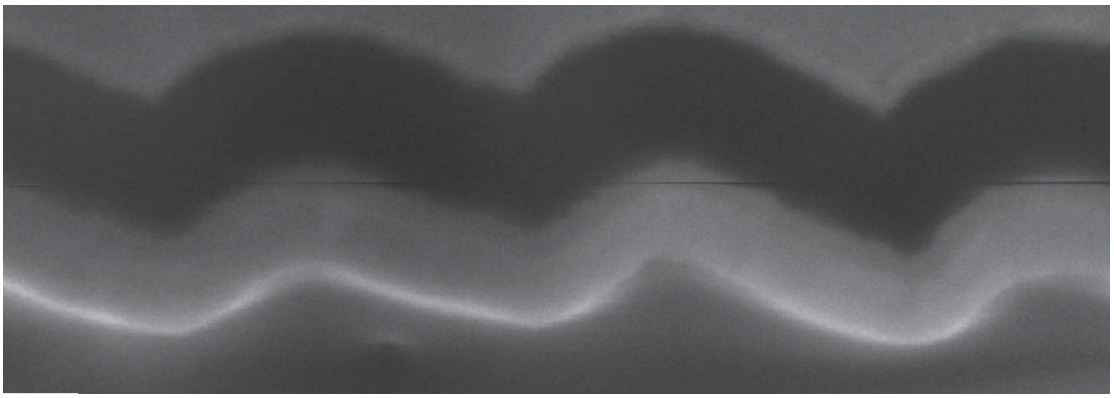

(a)

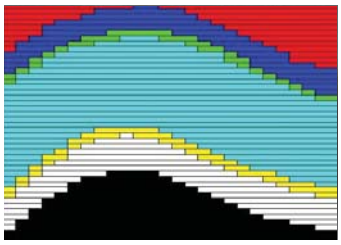

(b)

Figure 5.1: (a): SEM micrograph of the fabricated cell. (b): The RCWA model which is used for the simulations Sequence of layers from top to bottom is ITO (50 nm), p-Si (15 nm), i-Si (180 nm), n-Si (20 nm), ZnO (70 nm) and Ag, and grating period is 550 nm. The dark part of SEM shows the Si layers.

from top to bottom consists of ITO (50 nm), p-Si(15 nm), i-Si (180 nm), n-Si (20 nm), ZnO (70 nm) and Ag back-reflector[1]. The back-reflector has a 1D grating pattern with a period of 550 nm. We measured the external quantum efficiency (EQE) of the cell for different wavelengths. We also simulated the cell by using the rigorous coupled-mode analysis (RCWA) method [2]. The fabricated cell and the applied RCWA model are shown in Fig. 5.1. The method allows implementation of the cell interfaces such that the implemented interfaces resemble the texture of the real device. In this way, the non-conformalities in the deposition of different layers of the cell are taken into account.

Fig. 5.2 shows the EQE of the cell which is obtained through both experiment and simulation, under in-plane oblique incidence of light, for both TE and TM polarizations, as a function of the incident angle and wavelength. The resonances due to guided modes are observed in both simulation and experiment; the peaks at wavelengths longer than around 650 nm mainly correspond to the excitation of guided modes. Experimentally, in TE polarization, these excitations increase the EQE over a wide angular range at angles mainly other than normal. The simulation supports this strong enhancement of EQE at oblique incidence but it also reveals that there should be some relatively strong mode excitations at wavelengths

[1] In this section some of the results mentioned in Ref. [44] are used.

[2] For the simulations of this chapter, 31 Fourier orders were used in TE polarization and 91 orders were used in TM.

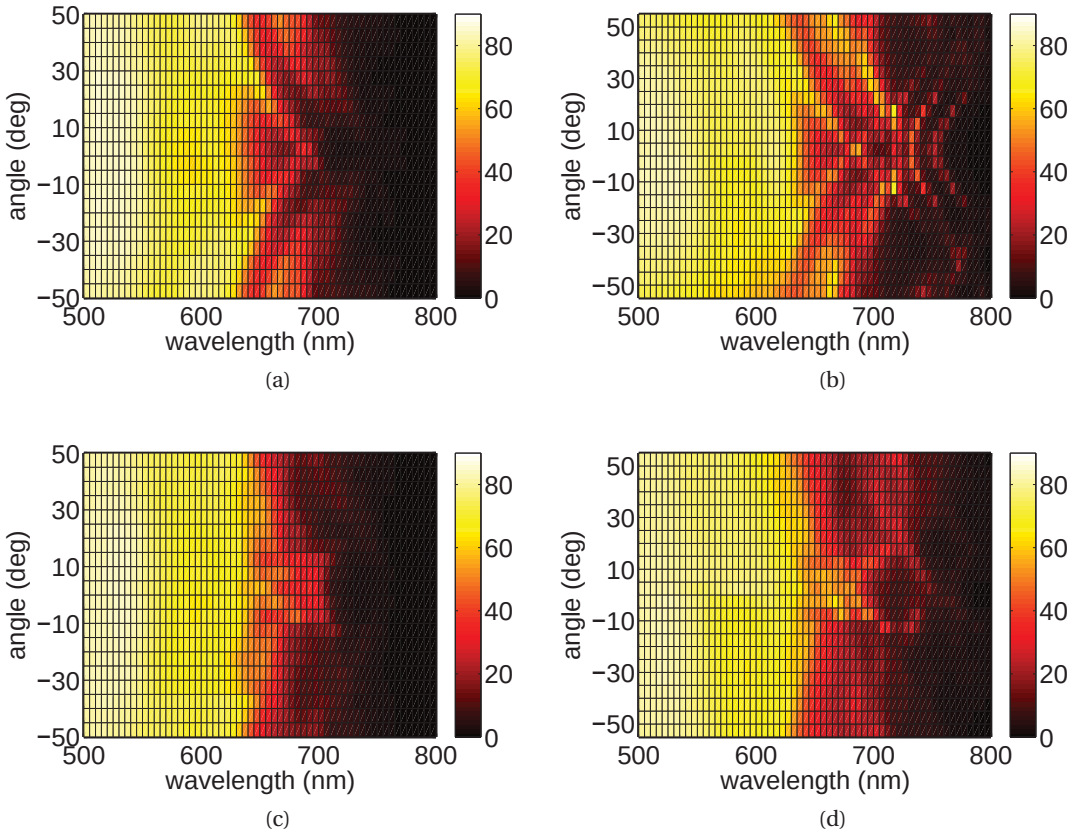

Figure 5.2: The EQE as a function of the incident angle and wavelength for the a-Si cell obtained through (a): experiment for TE-polarized illumination, (b): simulation for TE-polarized illumination, (c): experiment for TM-polarized illumination, (d): simulation for TM-polarized illumination.

longer than 700 nm at about normal incidence. These resonances are not captured in the experimental EQE. In TM polarization, the most significant enhancement is observed for around normal incidence, in both experiment and simulation.

The difference between the simulation and the experimental results may originate from various sources. First of all, in practice geometrical parameters of the grating may differ from one period to another. This may appear in the EQE as broadened resonances with lower peaks. Also some sharp resonances may not be observed clearly because they may be spread out over a wider spectrum. Imperfections in the device operation, such as ohmic losses can also reduce the measured EQE compared to the simulated values. Despite all these points, up to around 700 nm the experimental and simulated EQEs correspond to each other relatively well. As the wavelength becomes larger, their difference becomes more pronounced.

As this experiment and the corresponding simulations reveal, guided modes can effectively increase light absorption in a solar cell. Therefore, it is important to investigate them in more detail, and to study the ways that they can be excited more strongly. Specifically, it is of in-

terest to obtain cell geometries which can support such strong excitations. In Ref. [44], we presented an optimization of the mentioned solar cell for different back-reflector geometries. Our calculations showed that asymmetric textures may allow the existence of geometrical parameters which result in relatively high photocurrent for both polarizations.

In the previous chapter we studied mainly physical limitation on absorption enhancement in thin-film solar cells. For this aim, the exact geometries were not required. In this chapter, our focus is on specific close-to-reality geometries, and we go beyond optimization by studying physics of thin-film silicon solar cells considering realistic geometries.

5.4 Planar model: The impact of back-reflector

As a first approximation, one can use the band diagram of the planar device without interface texturing as an initial guess of the guided modes dispersion of the textured device. Of course in the real device, the bands are deviated from the modal structure of the planar geometry. However, if the texturing does not change the geometry significantly, this planar device approximation gives reasonable values for the propagation constants.

We consider a single junction a-Si solar cell stack. From bottom to top, the cell consists of a silver back-reflector, a 70 nm ZnO spacer, an n-i-p junction of a-Si:H with respective thicknesses of 20, 250 and 15 nm, and 50 nm ITO electrode. Fig. 5.3 shows the band diagram of the planar device which is obtained by the reflection pole method (RPM) [61] in both polarizations. In the dispersion diagram, the guided modes are between the light line of air and Si, which is a result of spread of wave energy over Si, other layers and air. If absorption is high, it becomes hard to detect modes because the resonances get very wide. For a fixed energy, the fundamental mode (0-th order mode) appears at higher parallel wavevectors ($k_{\|}$) compared to the other modes, regardless of polarization.

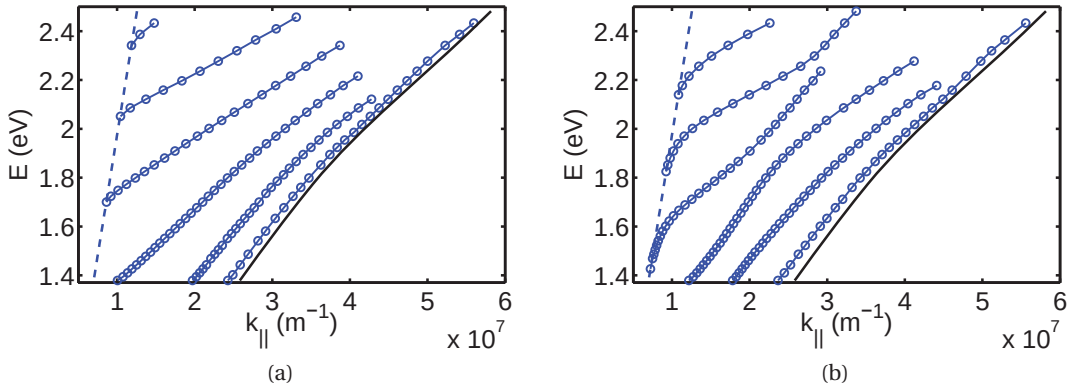

Figure 5.3: Dispersion diagram of a thin-film a-Si:H stack which consists of Ag, ZnO (70 nm), n-Si (20 nm), i-Si (250 nm), p-Si (15 nm) and ITO (50 nm) from bottom to top. (a)TE polarization (b) TM polarization. The dashed blue line is the light line of air and the black solid line is the light line of i-Si.

Fig. 5.4 shows the normalized magnitude of the electric field along the cell thickness at the wavelength of 700 nm (1.77 eV) under TE polarized illumination. Normalization for field amplitude is applied with respect to its highest value for each case. The vertical lines show the planar interfaces. The leftmost part is air and the rightmost region is Ag. In both air and Ag, increasing mode order results in more spread of the wave over space. This is in agreement with the intuition that in the dispersion diagram, the closer the mode to the Si light line, the more localized its energy to the Si layer.

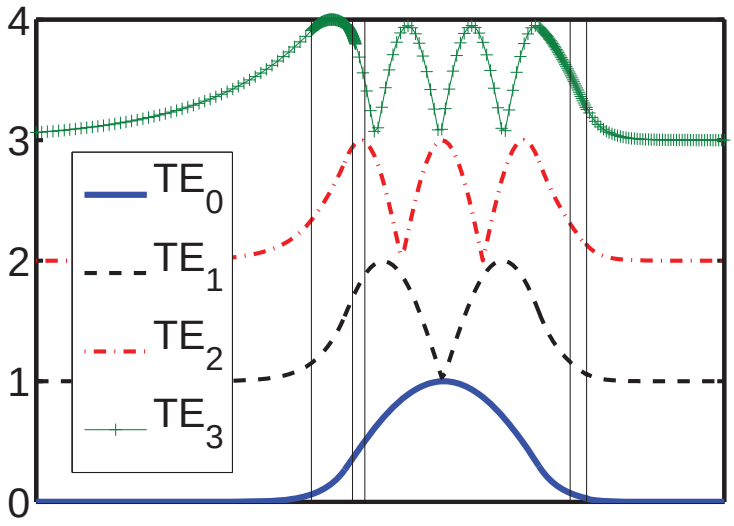

(a)

Figure 5.4: Normalized electric field magnitude for the TE modes of the cell at the energy of 1.77 eV (wavelength of 700 nm). The field is normalized to its largest value in each case. The horizontal axis shows the thickness of the structure. The air side occurs in leftmost part.

Fig. 5.5 shows the dispersion of the planar stack when the ZnO spacer layer is removed. In TE polarization, the only remarkable difference is that the guided modes are shifted slightly towards higher energies. However, in TM polarization, there is a dramatic difference in the dispersion diagram. The lowest order mode falls down to lower energies. It even goes beyond the light line of silicon in the dispersion diagram. Its dramatic displacement leaves space for the other modes to reconfigure their position in the dispersion diagram. However, the total number of modes in the dispersion diagram stays constant in the considered spectral range.

Violation of the placement between the light lines of air and Si in the dispersion diagram by the low-order mode in TM polarization is the characteristic of a surface plasmon. As its name suggests, a surface plasmon is a surface wave; its profile peaks exactly at the metallo-dielectric interface and decays into both adjacent media. Fig. 5.6 shows the normalized absolute value of the magnetic field for the planar stack (without the spacer layer) at the wavelength of 700 nm (1.77 eV) under TM polarized light. The fundamental mode is very localized to the metallic interface and its peak intensity is exactly on this interface. This is why it is ab-

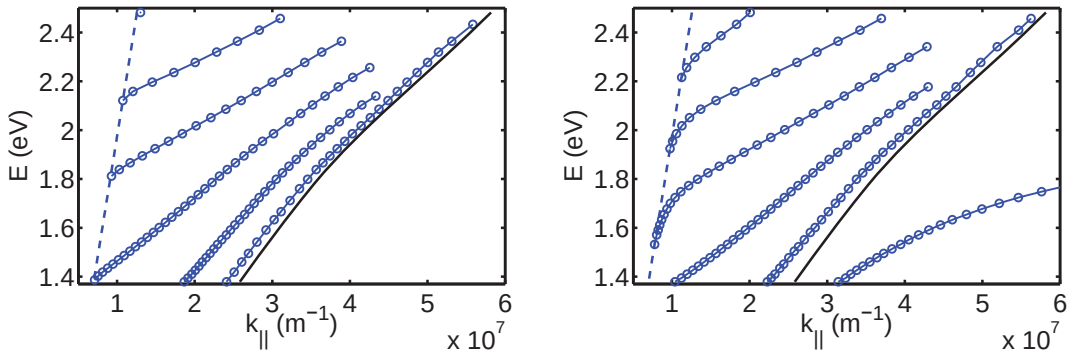

Figure 5.5: Dispersion diagram of a thin-film a-Si:H stack without spacer layer, which consists of Ag, n-Si (20 nm), i-Si (250 nm), p-Si (15 nm) and ITO (50 nm) from bottom to top. (a)TE polarization (b) TM polarization. The dashed blue line is the light line of air and the black solid line is the light line of i-Si.

solutely important to put the absorber as close as possible to this interface if it is intended to use the plasmon for improving photocurrent in the cell. Apart from this mode, the other modes show a normal guided-mode behavior. Their field amplitude extends mainly over the i-Si layer. The tail of profile in air shows the same trend as observed for TE modes: higher order modes are less confined to the stack and spread more over air.

5.4.1 Change of spacer material

It is clear by now that the spacer can have a remarkable effect on the optical properties of the lowest order TM mode. One important parameter to study is the material of which the spacer is made. In the previous example the spacer was assumed to be made of ZnO. Here, we assume that the spacer is made of MgF_2 and we compare the bands to the case with ZnO spacer. Our purpose here is to explore the effect of this material replacement only theoretically; in practice, MgF_2 will require some effort for electrical contacting.

Fig. 5.7 compares the dispersion diagram of the cell in two cases where a ZnO or MgF_2 spacer layer has been used. Both materials are almost lossless over the spectral range of interest, especially at long wavelengths, however, ZnO ($n \approx 2$) has a refractive index which is larger than the refractive index of MgF_2 ($n \approx 1.38$). In both cases, a spacer thickness of 70 nm has been considered. The red circles and the blue dots correspond to the cells with ZnO and MgF_2 layer respectively. Fig. 5.7a shows the bands for the two cases in TE polarization. In TE, both structures have almost the same dispersion diagram. In TM (Fig. 5.7b), the high order bands are deviated more compared to lower order bands. It seems that the TM modes with the same order are similar in shape and in their starting point at their onset on the light line of air. By moving on the bands from the light line of air to the light line of Si, the bands of the two cells (MgF_2 and ZnO) deviate from each other. Specially, band of the fundamental

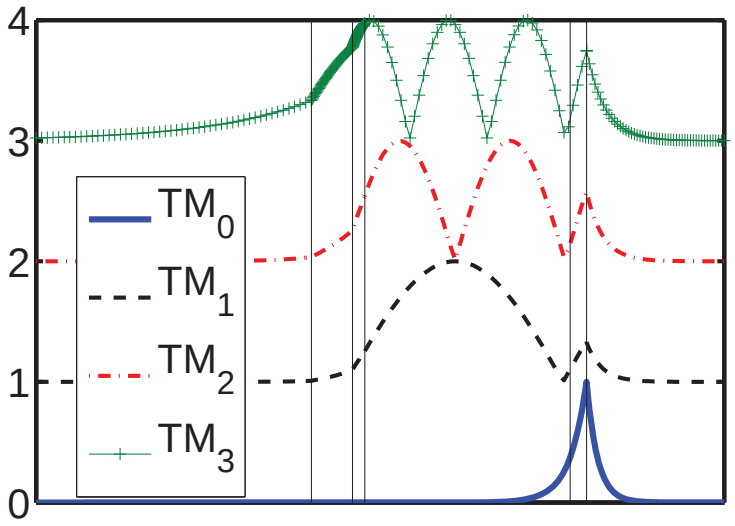

(a)

Figure 5.6: Normalized magnetic field magnitude for the TM modes of the cell without spacer layer at the energy of 1.77 eV (wavelength of 700 nm). The field is normalized to its largest value in each case. The horizontal axis shows the thickness of the structure. The air side occurs in leftmost part.

mode is very similar in both cases. This is because this mode is localized very well in the Si layer. Because the only difference between the two cases is the material used in the spacer, variation of the bands from one case two the other one is a sign of spread of electromagnetic energy over the spacer.

The refractive index of the spacer material has a key role in light-trapping in the cell, even if it does not absorb light at all. We note that the spacer can play two contradictory roles from an optical point of view. First, it can attract the electric energy of the external field because the electromagnetic energy density is proportional to permittivity. This is confirmed in Fig. 5.7b by the appearance of the bands of the same order at lower energies for the ZnO spacer compared to the MgF_2 one. However, more attraction of electromagnetic energy does not necessarily guarantee a higher absorption because the high refractive index of the spacer can also attract energy which is spread over the Si layer and result in reduction of field profile overlap with the active layer. It seems, thus, not easy to guess which one of these effects finally wins and attraction of energy by the spacer can lead to a higher photocurrent or not. For this, we need to study the impact of spacer in more detail. Later in section 5.5.2 we study the impact of spacer material is a cell based on a one-dimensional grating.

5.4.2 Effect of spacer thickness

Thickness of the spacer is another parameter which can affect the guided waves in the cell. In the extreme case where thickness of the spacer tends to zero, a plasmonic mode can coexist

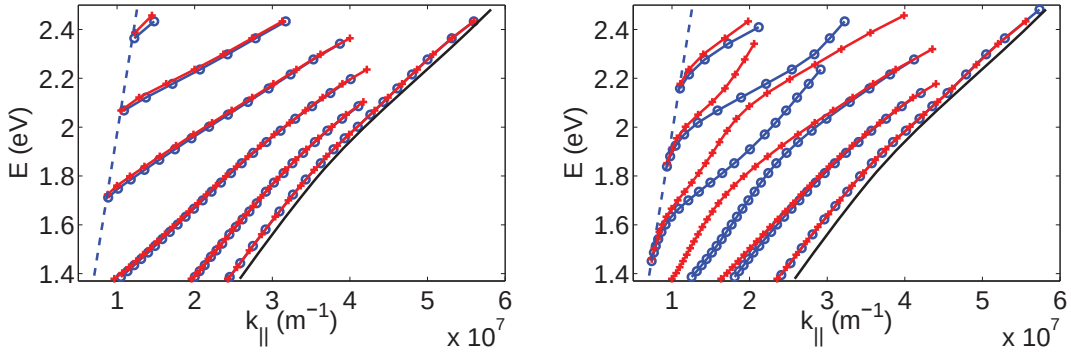

Figure 5.7: Dispersion diagram of a thin-film a-Si:H stack which consists of Ag, spacer (70 nm), n-Si (20 nm), i-Si (250 nm), p-Si (15 nm) and ITO (50 nm) from bottom to top. (a)TE polarization (b) TM polarization. The circles show the bands of the cell with ZnO spacer. The curves with '+' sign represent the bands of the MgF_2 spacer.

with higher order guided modes. It is interesting to find out how the thickness of the spacer changes the nature of the mode. In this part we study the effect of spacer thickness on the optical bands of the planar thin-film solar cell.

Fig. 5.8 shows the dispersion diagram of the cell with different ZnO spacer thicknesses of 70, 10 and 5 nm. Also the bands of the cell with no spacer are plotted in the figure. The cross marks shows the bands of the cell without spacer, and the circles, triangles and solid correspond to the spacer thickness of 5, 10 and 70 nm respectively.

Fig. 5.8a shows the bands of the cells in TE polarization. In TE polarization, the higher order modes of the cell with the thickest spacer (70 nm) show the largest deviation from the corresponding bands of the other cells. However, overall the bands are not much modified with changing the spacer thickness.

Fig. 5.8b shows the bands of the cells in TM polarization. In TM polarization, the optical bands deviate remarkably with changing the spacer thickness. For the higher order modes, the cell with the thickest spacer shows the most significant band deviations. These deviations are most pronounced for the TM_0 mode. The lowest order mode is a plasmonic mode for the cell without spacer. For the spacer thickness of 5 nm, this lowest order mode is still a plasmonic mode because it occurs beyond the light line of Si. Spacer thickness of the 10 nm and 70 nm correspond to conventional guided modes which occur between the light line of air and Si, thus they do not support any plasmonic modes. The fundamental mode of the cell with 10 nm spacer is very close to the light line of Si which shows that it is very localized in Si. However, for the spacer thickness of 70 nm, this mode is shifted towards higher energies. This is expected that by increasing the spacer thickness, the fundamental mode (which can be guided or plasmonic) is pushed towards higher photon energies. The reason is that increased thickness of the low-index spacer reduces the effective refractive index of the

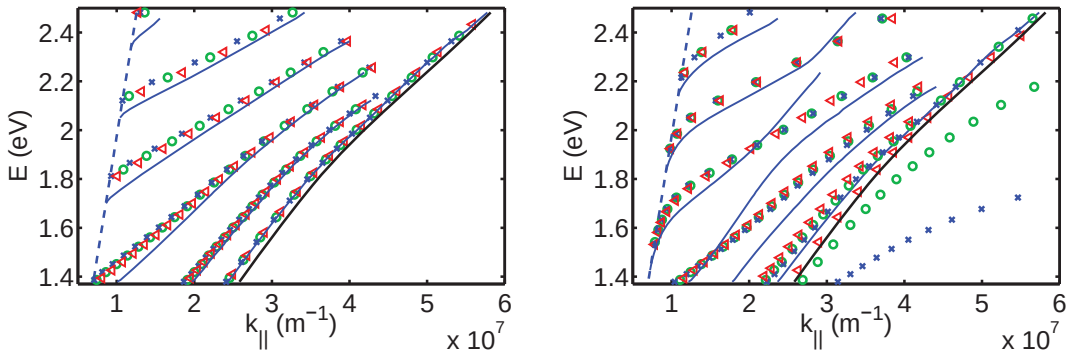

Figure 5.8: Dispersion diagram of a thin film a-Si:H stack which consists of Ag, ZnO (variable thickness), n-Si (20 nm), i-Si (250 nm), p-Si (15 nm) and ITO (50 nm) from bottom to top. (a)TE polarization (b) TM polarization. The blue crosses shows the bands of the cell without spacer, and the green circles, red triangles and blue solid correspond to the spacer thickness of 5, 10 and 70 nm respectively.

whole cell. However, it is hard to guess intuitively that in TM polarization, this band shift is more significant for a thinner spacer thickness, as observed in Fig. 5.8b. Altogether, a thin spacer layer can change the nature of the plasmonic mode into a guided mode. Nevertheless, for very thin spacer layers, the mode may still be called plasmonic according to the dispersion diagram of the multilayer stack.

5.5 Texture geometry and diffraction phenomena

The modes which are obtained in the dispersion diagrams need to be coupled to external radiation. This is done by texturing the interfaces of the structure. Geometry of this texture is of primary importance for both the number of excitations and the coupling strength. For example, it has been shown recently that using the hexagonal geometry may result in larger absorption than the square lattice [132, 83]. The reason is the higher number of mode excitations for hexagonal geometry.

For 1D gratings, the Bragg condition takes a simple form

$$k_{\parallel}^{m} = k_{\parallel}^{0} + \frac{m\lambda}{\Lambda} \tag{5.1}$$

where $k_{\parallel}^{0}$ is the parallel component of the unperturbed wave-vector. The effect of the grating is to shift the parallel component of the wave-vector by multiplies of the reciprocal lattice vector. For 2D gratings, the reciprocal and thus the number of diffraction orders depends on

lattice geometry in real space. In this case, the Bragg condition can be expressed as

$$\vec{k}_{\parallel}^{m_1,m_2} = \vec{k}_{\parallel}^{0,0} + \lambda\,(m_1\mathbf{e}_1/\Lambda_1 + m_2\mathbf{e}_2/\Lambda_2) \tag{5.2}$$

where $\mathbf{e}_1$ and $\mathbf{e}_2$ are the reciprocal lattice vectors. From Eq. 5.2 the impact of the lattice geometry on the number of resonances can be understood. The periodic pattern can excite guided modes for all m_1 and m_2 integers that satisfy the criterion $\left|\vec{k}_{\parallel}^{m_1,m_2}\right| < nk_0$.

Apart from the general geometry of the grating which was studied in section 4.1.2, the details of its pattern are important too. For example symmetry of the grating seems to have a pattern on absorption enhancement. In general, a grating texture which has several spatial frequency components, can shift the guided modes by using these components; therefore, it seems primarily that the richer the Fourier decomposition of a texture is, the more probable it will enhance absorption. This however needs to be investigated in more detail.

5.5.1 Effect of texture symmetry

Texturing a cell's interfaces couples light to its guided modes. The geometry of the texture can change the coupling properties of the cell. The exact amount of coupling can be obtained through a numerical simulation of the cell but it is possible to figure out rules of thumb too. For example, coupling can be improved by increasing the texture height (modulation depth) [107]. However high aspect ratios are hard to fabricate. They can also deteriorate a cell's electronic properties for example they can result in the appearance of shunts in the cell.

Symmetry of the texture is another geometrical parameter which affects coupling properties of the texture. Based on the work of Heine and Morf [133], asymmetric textures are preferred. Superiority of asymmetric textures can be attributed to the higher number of mode excitations that they support. In a recent calculation of the upper bound of absorption in solar cells, Yu *et al.* assumed that asymmetric patterns can enhance absorption in solar cells twice as strongly as symmetric patterns [20].

While an asymmetric texture can excite more resonances compared to a symmetric one, it is not clear whether its resonances are excited as strongly. In other words, it is possible that a single wide resonance can enhance absorption more significantly than a multitude of sharp resonances. Are asymmetric patterns preferred even after considering coupling strength? In the following example we try to respond this question.

Consider an a-Si solar cell which from top to bottom consists of ITO (50 nm), p-Si (15 nm), i-Si (250 nm), n-Si (20 nm), ZnO (70 nm) and Ag. Assume that the silver back-reflector is textured into three different 1D grating patterns: sinusoidal, symmetric trapezoid and asymmetric sawtooth. The normalized shape of the patterns are depicted in Fig. 5.9. Depth of grating and its period is considered 150 and 500 nm respectively for all cases. Also assume that the

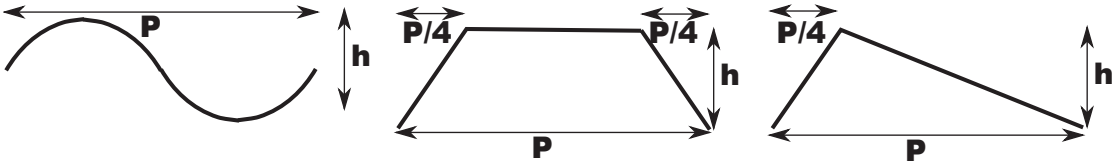

Figure 5.9: The different back-reflectors which are simulated.

interfaces of the cell are conformal. This is consistent with the nearly conformal growth of the cell layers in fabrication as long as moderate thickness is used. We simulate the cells under in-plane oblique incidence of TE-polarized (electric field parallel to the grooves) light. For simplicity we consider only in-plane illumination which means that the incidence plane is normal to the grating grooves. Fig. 5.10 shows angle-resolved EQE of the cells based on the different back-reflector shapes. For symmetric shapes, only positive angles are considered since negative angles lead to similar results. The peaks at wavelengths longer than 650 nm are signatures of guided modes. Based on these EQE plots, EQE varies as a function of both the incident angle and wavelength. The final benchmark to compare light absorption in the cells is the short circuit current density.

Fig. 5.11a compares the short circuit current density of the cells as a function of incident angle under TE-polarized in-plane incidence. It is observed that the symmetric patterns can provide J_{sc} as large as for the asymmetric pattern. At normal illumination, this is exaggerated because both symmetric patterns result in a J_{sc} higher than the one of the asymmetric pattern. The symmetric trapezoidal pattern seems to be less efficient than the two other patterns at around 30 degrees. Furthermore the sinusoidal pattern results in quite a high J_{sc} although it may seem that its Fourier spectrum is not rich enough to perform coupling as efficiently as the two other textures. Another important point is that the maximal photocurrent is obtained for angles other than normal. This puts an important question to a huge body of photovoltaic literature which only report J_{sc} or EQE under normal incidence of light and has been previously addressed by us [82, 137].

Fig. 5.11b compares the J_{sc} of the cells under TM-polarized light. Other conditions are the same as before. This time, normal incidence results in higher light absorption except for the symmetric trapezoidal grating. Overall, the sinusoidal and the asymmetric patterns show a similar trend for J_{sc} variations. The main difference is that for negative angles, the asymmetric grating provides higher photocurrent and for positive angles, the sinusoidal grating does so. Again the sinusoidal grating performs better than the symmetric trapezoidal grating for almost all incident angles.

Fig. 5.11c shows the unpolarized short circuit current density of the cells. These results are obtained by averaging the TE- and TM-polarized results. The sinusoidal grating performs better than the two other gratings at normal incidence and its J_{sc} is slightly larger than the one of asymmetric grating. The sinusoidal grating also provides the highest J_{sc} values for positive angles but for negative angles, its J_{sc} is less than the J_{sc} of the asymmetric grating.

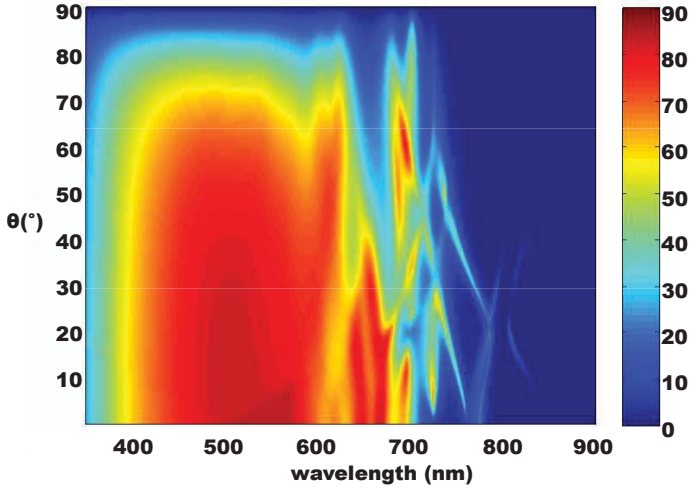

(a)

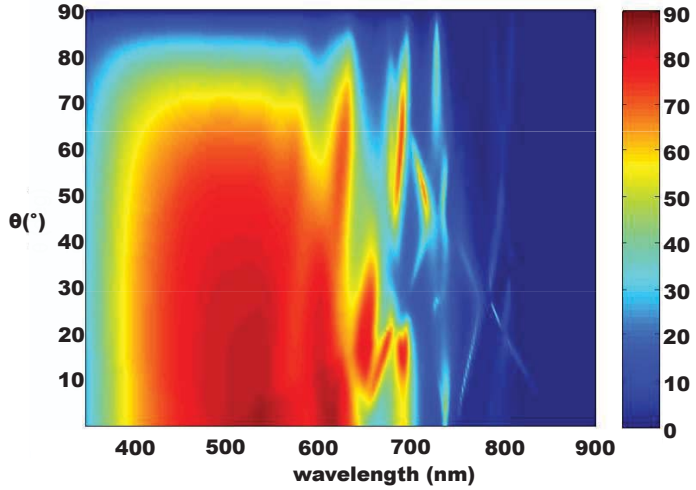

(b)

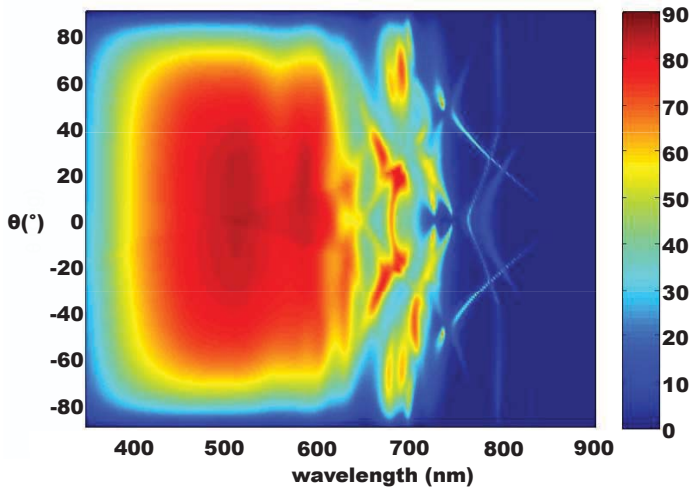

(c)

Figure 5.10: TE polarized EQE of the cells based on 1D grating with (a) sinusoidal (b) symmetric trapezoidal and (c) asymmetric geometry. The grating depth is 150 nm.

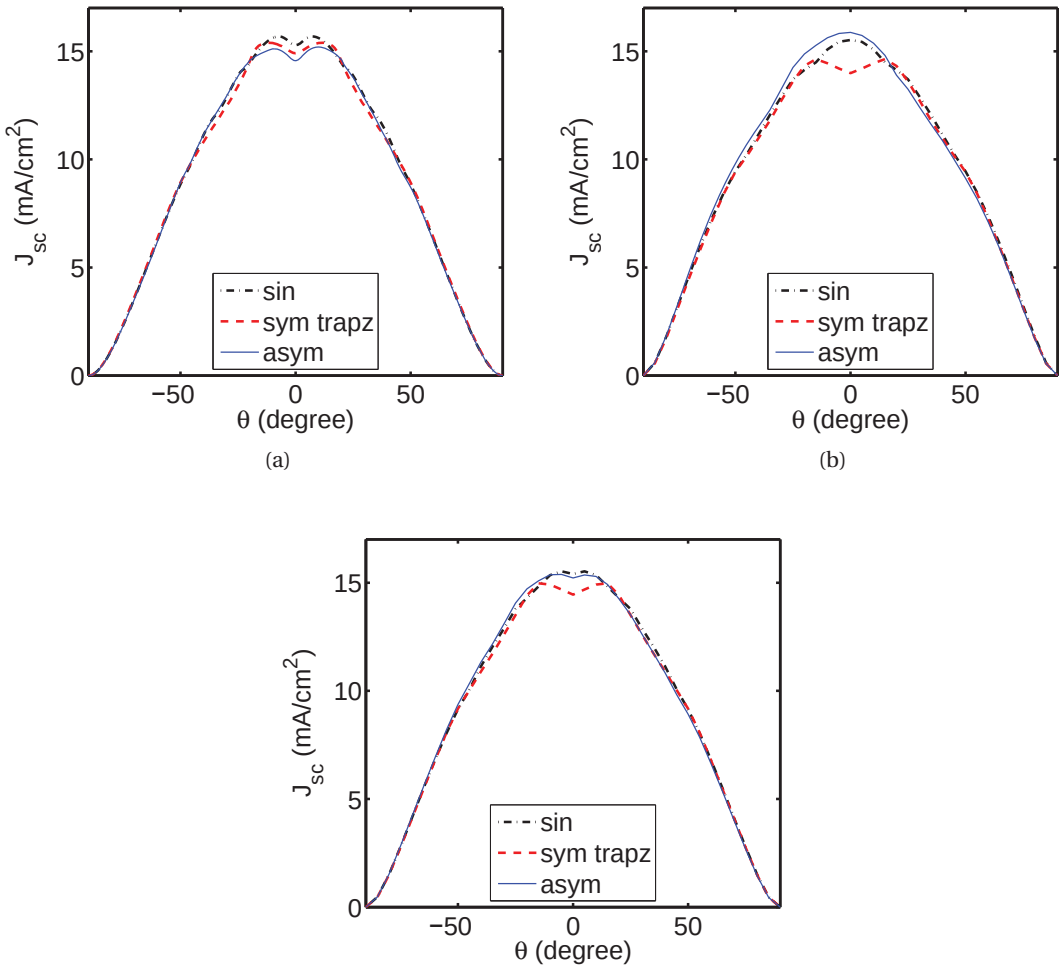

Figure 5.11: The short circuit current density as a function of the incident angle for the three different geometries under (a) TE, (b) TM, and (c) unpolarized illumination. The grating depth is 150 nm.

The asymmetric grating performs generally better at negative angles but at positive angles, its J_{sc} is smaller than the two other cells.

Figs. 5.12a, 5.12b and 5.12c compare the TE- and TM- polarized photocurrents for the sinusoidal, trapezoidal and asymmetric pattern respectively. In all of the cells, TM polarization of light provides higher J_{sc} at large angles. For almost normal incidence, TM polarization is preferred only for the asymmetric pattern. For the asymmetric grating, TM polarization is better except for angles around 30 degrees.

Fig. 5.13 shows the TE-polarized EQE as a function of wavelength and incident angle for the cells when the peak to valley depth is changed from 150 nm to 300 nm. Compared to the cell with 150 nm grating depth (Fig. 5.10), EQE values are relatively higher in general and diffraction phenomena are more observable. Regardless of the grating shape, there is a region of high EQE which starts from the wavelength of 500 nm towards longer wavelengths. As Fig. 5.13 shows, this high EQE region seems to occur between two lines which are the mirror image of each other with respect to horizontal axis ($\theta = 0$). These lines are actually curves which correspond to the appearance of first order reflection. Regardless of the grating shape, the condition of existence of only one reflection order has a strong impact on the coupling strength of guided modes and it ameliorates the EQE. As previously stated by Yu *et al.*, the existence of only one reflection order in a cell with back-reflector can improve light absorption beyond the ergodic limit [20]. There is also another curve of EQE variation appearing at shorter wavelength which seem to separate a high-EQE region from a low EQE region. This curve corresponds to the appearance of the second order reflection orders. For the asymmetric grating, this curve is pronounced well for negative angles but for positive angles, its presence is not as apparent.

Fig. 5.14 compares the angular behavior J_{sc} of different texture under TE (Fig. 5.14a), TM (Fig. 5.14b) and unpolarized (Fig. 5.14c) illumination. In TE poalrization, the asymmetric grating produces the highest J_{sc}. However, when a broader range of angles are considered, the symmetric trapezoidal pattern seems to outperform the other cells. In TM polarization, the asymmetric grating has the lowest J_{sc} under normal illumination and at positive incident angles. But it excels the two other grating patterns at negative incidence angles similar to the previous example with the grating depth of 150 nm. For unpolarized illumination, the symmetric trapezoidal pattern seems to be the optimum of the three patterns for all possible incident angles. This example puts a question on the intuition that asymmetric patterns can enhance absorption more significantly than the symmetric patterns. Based on the two mentioned examples, it seems that this intuition is questionable for deep gratings.

Fig. 5.15 compares the TE and TM polarized J_{sc} for each grating pattern where the grating depth is 300 nm. For the sinusoidal grating, the TM polarized J_{sc} is slightly lower at close to normal illumination but it is much superior at large incident angles. The superiority of TM polarized photocurrent to the TE polarized one is observed in all of the considered grating patterns but it is more pronounced for the sinusoidal pattern. For the symmetric trapezoidal

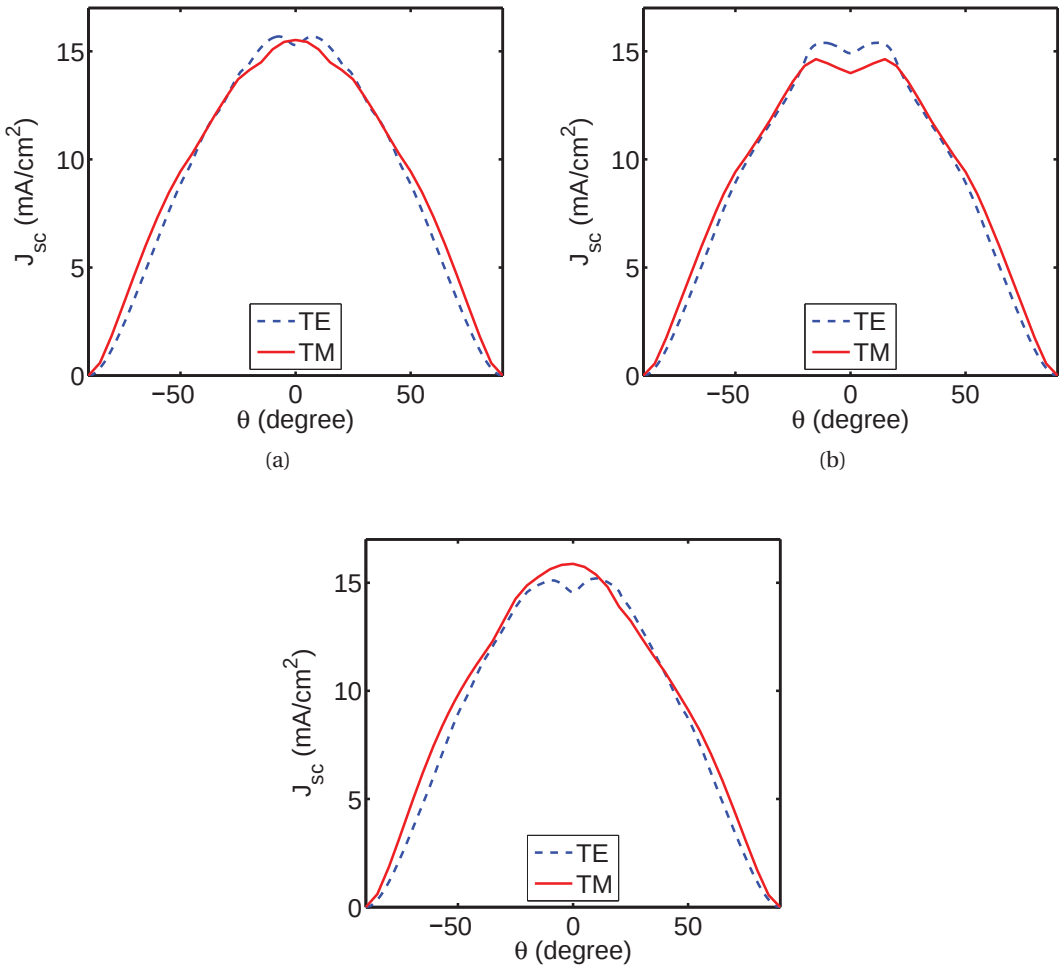

Figure 5.12: The short circuit current density as a function of the incident angle for the cell based on a 1D grating with the (a) sinusoidal, (b) symmetric trapezoidal, and (c) asymmetric pattern. The grating depth is 150 nm.

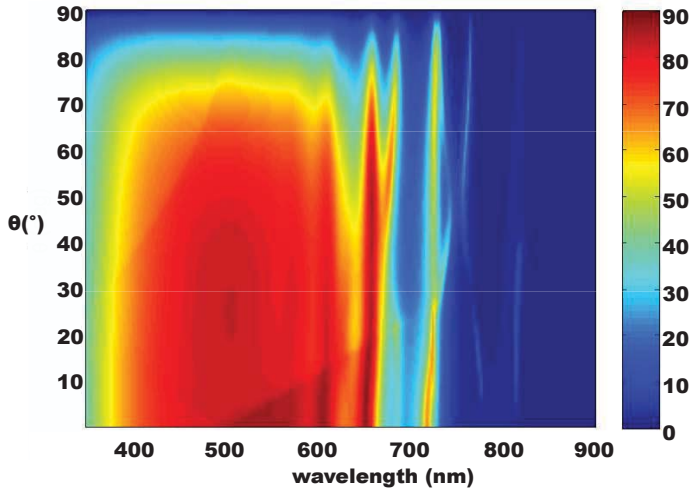

(a)

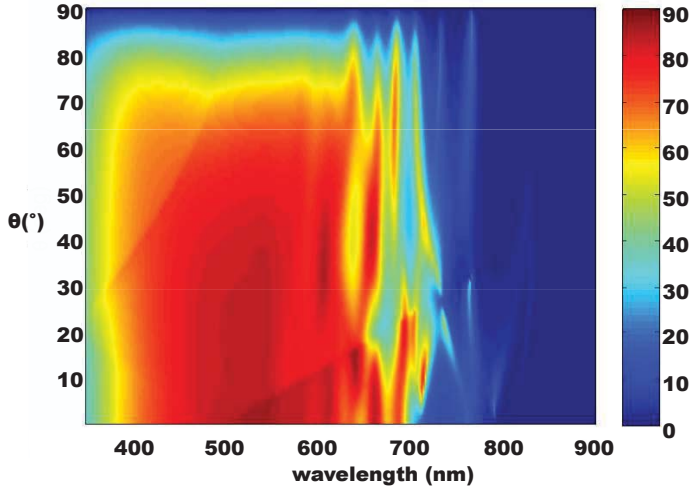

(b)

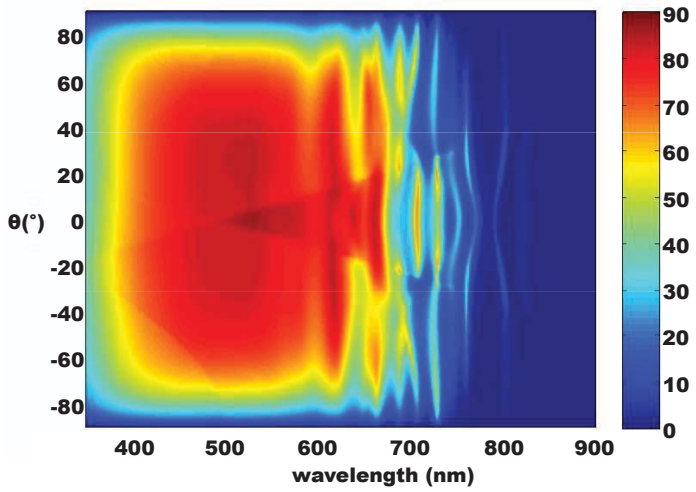

(c)

Figure 5.13: TE polarized EQE of the cells based on 1D grating with (a) sinusoidal (b) symmetric trapezoidal and (c) asymmetric geometry. The grating depth is 300 nm.

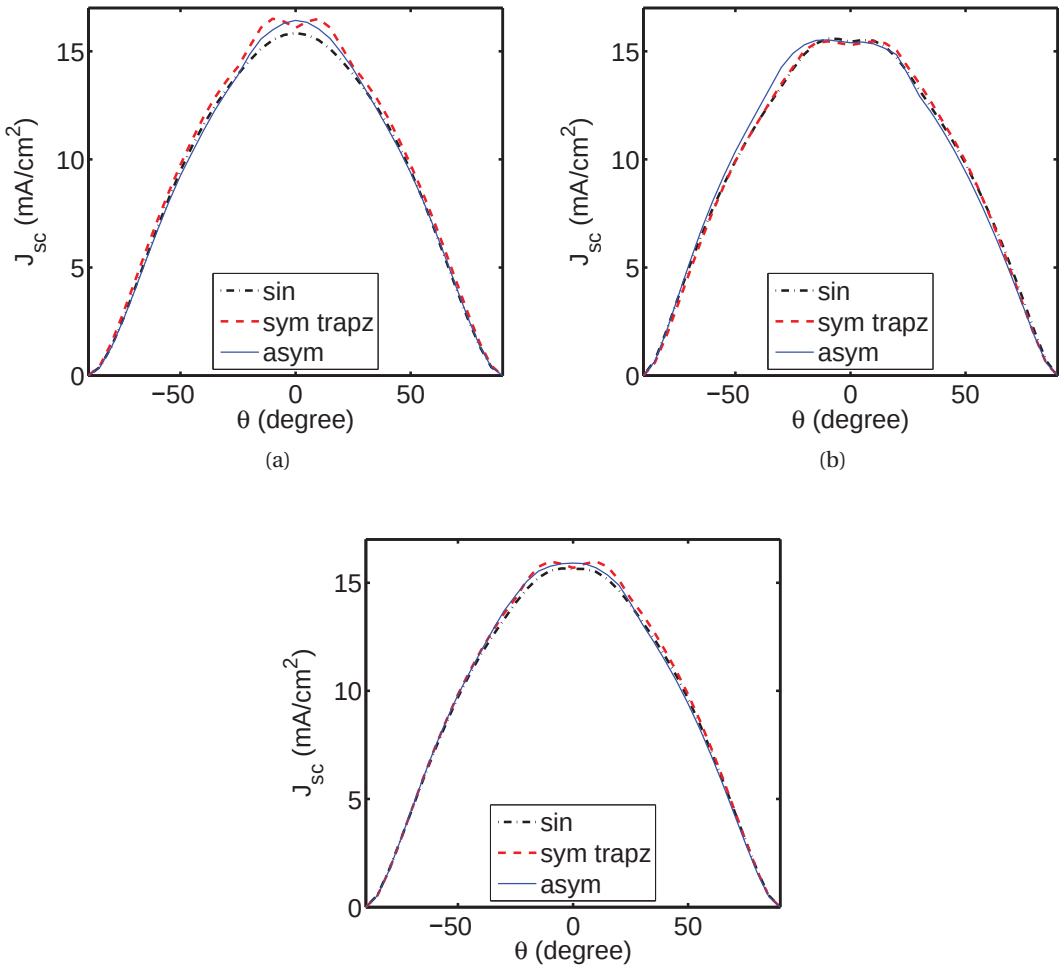

Figure 5.14: The short circuit current density as a function of the incident angle for the three different geometries under (a) TE, (b) TM, and (c) unpolarized illumination. The grating depth is 300 nm.

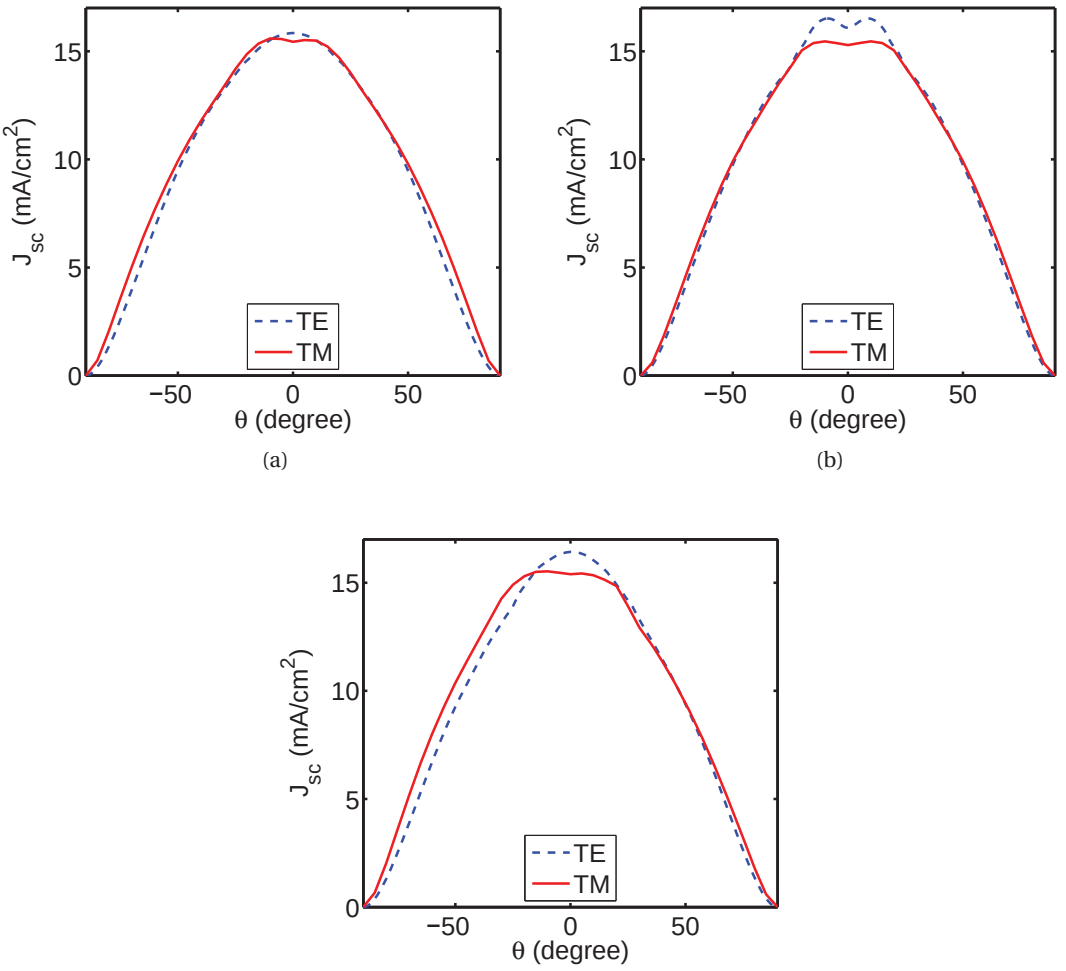

Figure 5.15: The short circuit current density as a function of the incident angle for the cell based on a 1D grating with the (a) sinusoidal, (b) symmetric trapezoidal, and (c) asymmetric pattern. The grating depth is 300 nm.

pattern, under normal incidence, the J_{sc} is significantly larger in TE polarization compared to TM polarization. This advantage of TE polarization remains valid until around 45 degree. At larger incident angles, TM polarization results in larger photocurrent. For the asymmetric pattern, still TE polarization is superior over a limited angular range around normal illumination. At larger angles, especially at negative angles, TM polarization leads to larger photocurrent. Overall, TE polarized light seems to be beneficial at close to normal incidence and TM polarized illumination helps increasing the photocurrent at larger incidence angles.

Fig. 5.16 compares the unpolarized J_{sc} of the different grating patterns for the grating depths of 150 and 300 nm to reveal the impact of grating depth on the J_{sc}. For the sinusoidal pattern, the effect of grating depth is marginal at around normal incidence. At larger angles, however, the grating depth has a clear impact and its corresponding photocurrent becomes significantly larger than the photocurrent of the shallower grating. For the symmetric trapezoidal and the asymmetric grating patterns, the effect of grating depth on photocurrent increase is pronounced clearly over almost all the range of incident angles. As mentioned, the asymmetric and the symmetric trapezoidal grating patterns resulted in the largest photocurrent for the grating depth of 150 nm and 300 nm respectively. Fig. 5.16d compares these two best obtained J_{sc}s. The illumination is unpolarized. It is observed that the deeper grating outperforms the shallower grating. Based on these observations, it seems that the grating depth has a clear effect on absorption enhancement in solar cells but to find an optimal texture, simulations are necessary to do. Furthermore, it appears that the effect of grating depth on the photocurrrent is more pronounced compared to the grating texture symmetry.

5.5.2 Change of spacer in cell based on 1D gratings

As previously discussed in section 5.4.1, the spacer material can have an impact on the photocurrent in the thin-film solar cell. We showed that the change of spacer material can modify the optical bands of the solar cell, thus, it may either increase or decrease light absorption in a cell. Here, we consider a cell based on a 1D Ag grating and by rigorous calculation, we study the impact of spacer material on a cell's J_{sc}. The cell geometry is similar to the previous example and a grating depth of 150 nm has been considered. The only difference from the previous example is that the spacer material is changed from ZnO to MgF_2. As previously discussed in section 5.4.1, the higher refractive index of ZnO compared to MgF_2 can attract electromagnetic energy more effectively into the cell but similarly it can do the same to the energy which is spread over the i-Si layer towards the spacer layer. In this section we perform rigorous calculations to understand which of these two effects is dominant at last.

Fig. 5.17a shows the unpolarized J_{sc} for the cell with MgF_2 spacer for the different grating patterns. Similar to the case with ZnO spacer, the asymmetric grating provides the largest photocurrent at negative angles but it gives the smallest photocurrent value at positive angles. At close to normal incidence, its corresponding J_{sc} is slightly larger than the sinusoidal grating. By assuming that the range of incident angles is limited we can choose the asymmet-

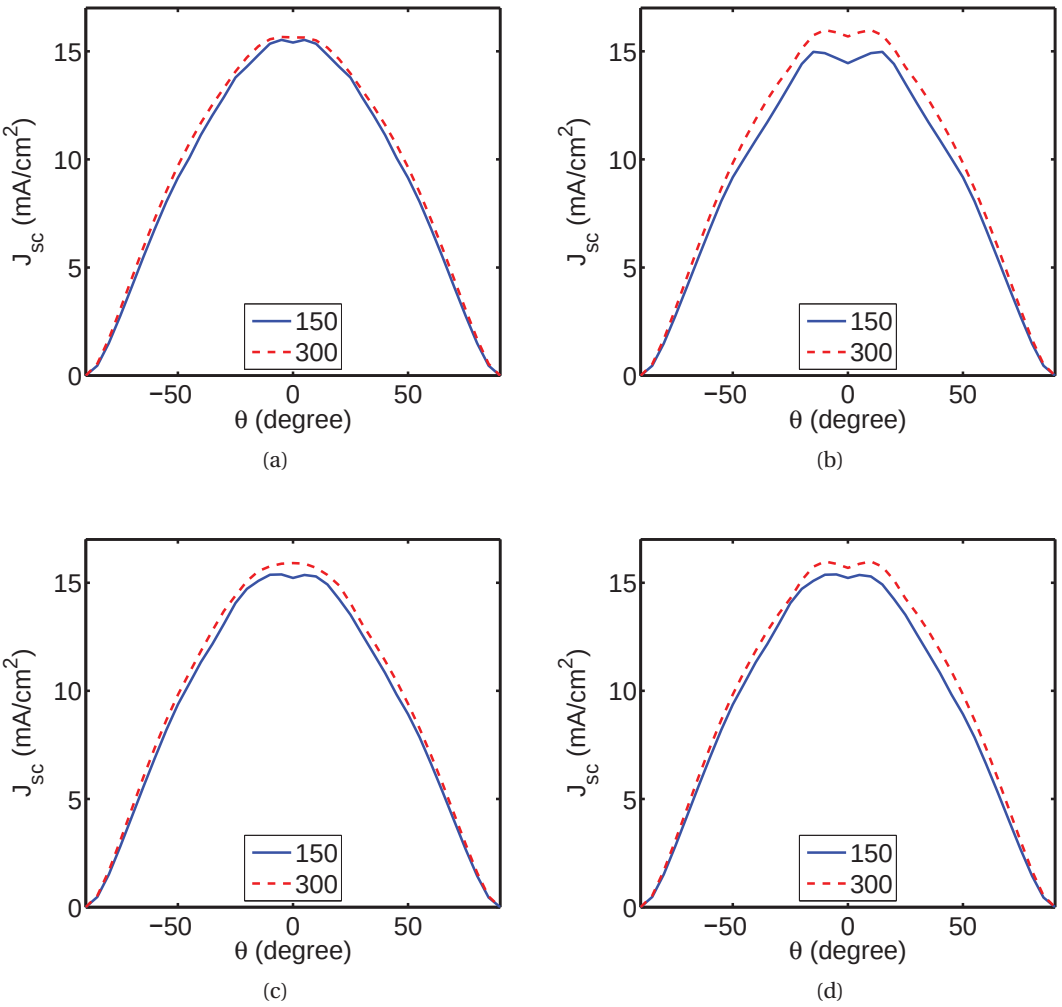

Figure 5.16: Comparison of the unpolarized short circuit current density as a function of the incident angle for the cell based on a 1D grating with the (a) sinusoidal, (b) symmetric trapezoidal, and (c) asymmetric pattern. The blue solid curves and the red dashed correspond to the grating depth of 150 and 300 nm respectively. (d) The best textures for unpolarized illumination for each grating depth.

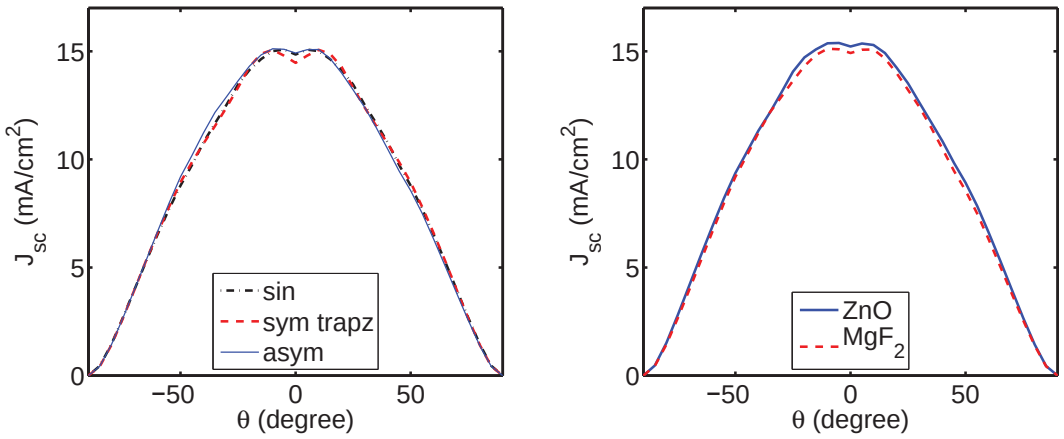

Figure 5.17: (a) Unpolarized photocurrent of the cell with MgF_2 spacer as a function of the incident angle for the different grating textures with 150 nm depth. (b) Best unpolarized results for the cells with MgF_2 (blue solid) and ZnO (red dashed) spacer.

ric pattern as the optimal pattern similar to the case of ZnO spacer. Fig. 5.17b compares the J_{sc} of the cells based on asymmetric patterns under unpolarized illumination for MgF_2 and ZnO spacers. The ZnO spacer provides a higher photocurrent over all incident angles. This shows that a higher refractive index of spacer has attracted energy into the cell and thus has increased light absorption. Nevertheless, it seems that this conclusion may not be extended to the general case and rigorous calculation is inevitable for different geometries.

5.5.3 Two-dimensional gratings

Two-dimensional (2D) gratings can excite more resonances compared to 1D gratings. As observed in the previous section, the higher number of resonances can lead to more efficient light absorption at least for an angular range close to normal incidence. One should perform rigorous calculations to find how much the guided modes can enhance absorption in a solar cell.

Consider a thin-film a-Si solar cell with the following layers from top to bottom: ITO (60 nm), p-Si (15 nm), i-Si (200 or 250 nm), n-Si (20 nm), ZnO (70 nm) and Ag (back-reflector). By changing the back-reflector geometry, we study the impact of different parameters on light absorption in the cell. Assume that the cell is based on a 2D grating with symmetric square geometry as depicted in Fig. 5.18a. Period of the grating is 500 nm in both periodic directions [3]. Simulations of this section are based on rigorous finite element calculations.

Fig. 5.19a demonstrates the rigorous calculation of the EQE of the cell with the i-Si thickness

[3] We did not optimize the period here; our aim is mainly understanding in this part.

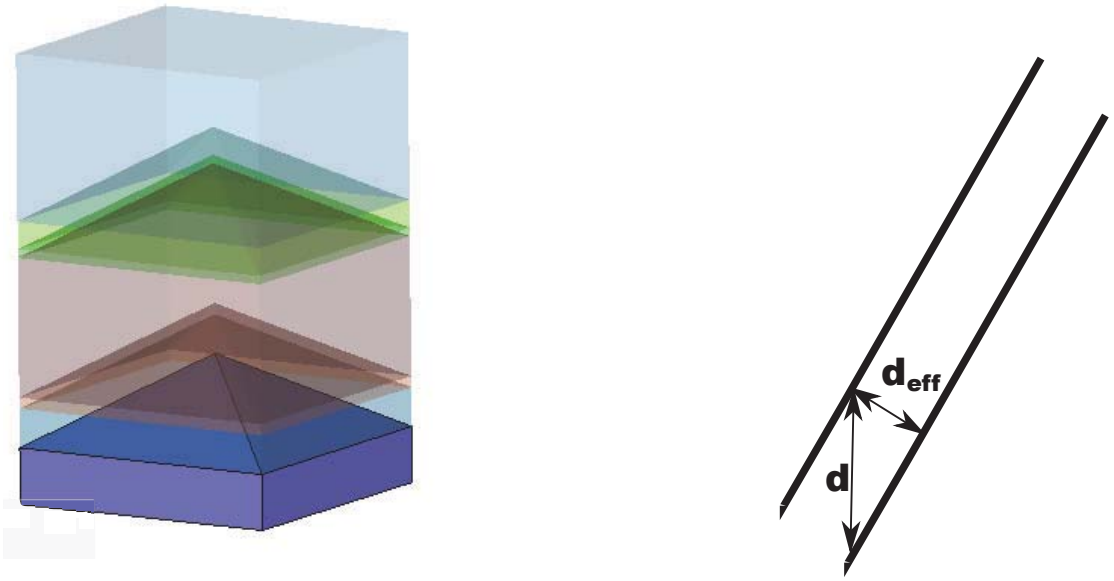

(a) (b)

Figure 5.18: (a): Schematics of the solar cell based on a 2D symmetric square grating. (b): The thickness of the layers as considered in the simulations (d) and the minimum thickness of the layer observed by the incident photons (d_{eff}).

of 200 nm for two different grating peak to valley depths of 150 and 300 nm[4]. At short wavelengths, there is a remarkable difference between the EQEs. According to Fig. 5.18b, this can be explained by the difference between the vertical (d) and the effective thickness (d_{eff}) of the cell layers, which are connected by $d_{eff} = d\cos\theta$ where θ is the incidence angle. In the simulations, usually d is kept constant, thus a smaller effective thickness is obtained for deep gratings. In the experiment this enhancement is not as pronounced as in the simulations because of the almost-isotropic behavior of the deposition process.

Fig. 5.19a shows also that an increased grating depth enhances the EQE at wavelengths longer than 500 nm. At these wavelengths, the front layers of the cell are almost transparent and their effect on the EQE is marginal. The impact of interference is the same for both cases because the thickness of the layers is similar in both cases. Thus, I interpret the difference between the two EQEs as the stronger excitation of guided modes for the deeper grating [5]. At longer wavelengths, the EQE of the deeper grating is still larger but this superiority diminishes at wavelengths longer than 700 nm. Overall, the 300 nm deep grating shows a larger EQE over a broad wavelength range from about 400 to 700 nm [6].

We repeat the same simulation for the i-Si thickness of 250 nm. The resulted EQEs are plotted

[4]The simulation is done by the HFSS software package[138]

[5]Here I have assumed that near-field effects do not influence the optical response of the cell after at wavelengths longer than 500 nm remarkably.

[6]Fabrication of solar cells with high aspect ratios might be problematic in practice, at least with the present technology.

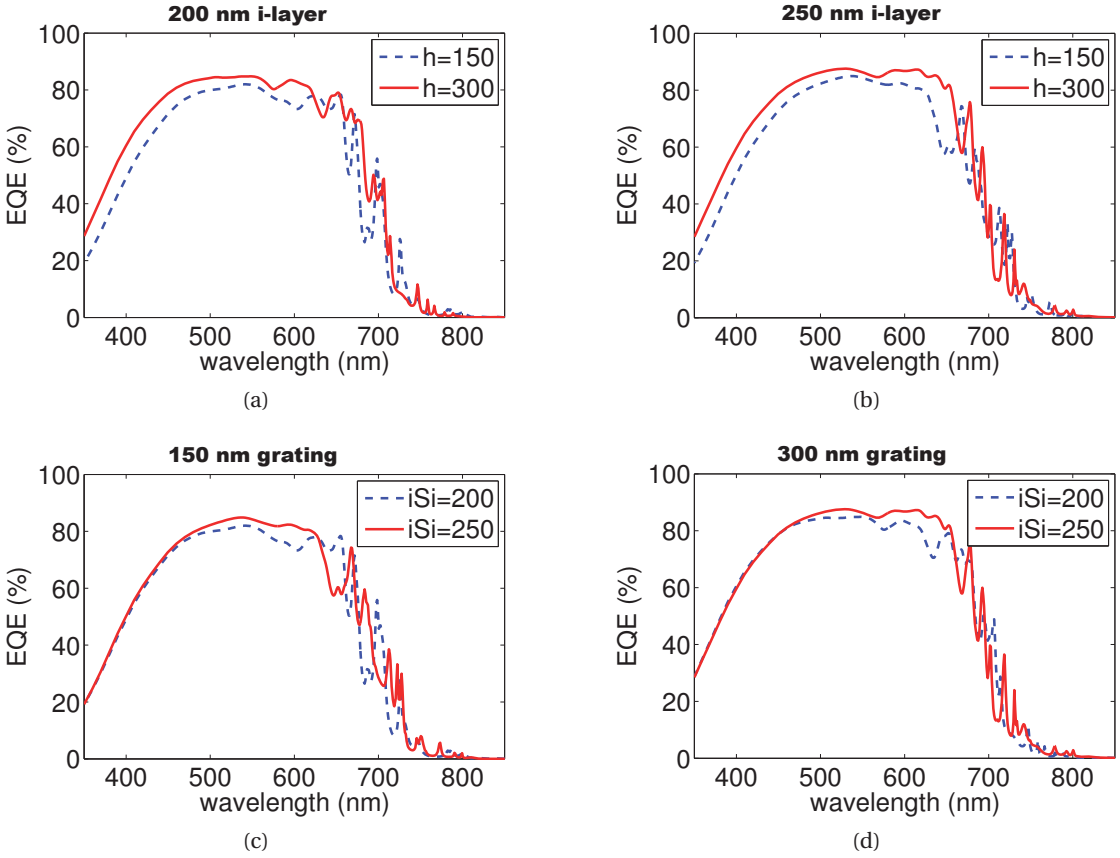

Figure 5.19: Effect of grating depth (h) and i-Si layer thickness on the EQE of the cell with an Ag back-reflector in the shape of a symmetric square pyramid. (a): The i-Si layer thickness is 200 nm. (b): The i-Si layer thickness is 250 nm. (c): Grating depth is 150 nm. (d): Grating depth is 300 nm.

in Fig. 5.19b. Again the EQEs are (spuriously) different at short wavelengths. The EQE peak drop at around 650 nm is shifted towards longer wavelengths for the deeper grating; this is the major difference between the two EQEs. At long wavelengths the EQEs are very similar. It seems that if the i-Si layer is thick enough, the grating depth does not change the EQE that much.

As a next example, let us study the effect of i-Si thickness in more detail by keeping the grating depth constant. Fig. 5.19c considers the case where grating depth is 150 nm, and compares i-Si layer thicknesses of 200 and 250 nm. At short wavelengths, the EQE of the cells is very similar, which is due to the resemblance of the cell geometry in the front layers. The thicker cell has a remarkable advantage over the wavelengths from 500 to 650 nm. At longer wavelengths, there is not a remarkable difference between the two cells.

The latter example is repeated for a grating depth of $h = 300$ nm and the results are plotted in Fig. 5.19d. The observations are similar to the previous case; the EQEs are similar at short and long wavelengths and the thickness of the i-Si layer mainly affects the EQE in the wavelength

range from 500 to 650 nm.

Symmetry of the grating pattern is another important factor to study. For this, we consider a symmetric grating as before and an asymmetric grating, which are plotted in Fig. 5.20a and 5.20b respectively. The asymmetric pattern is the same asymmetric pattern as Fig. 5.9 applied in both periodic directions. The cell is the similar to the previous example; the only differences are the i-Si layer thickness (180 nm) and the period (550 nm). Figs. 5.20c and 5.20d show the EQE of the cell for a grating depth of 150 and 300 nm respectively. For both cells. Asymmetry of the grating leads to slightly higher EQE. This can be attributed to the richer spectrum of an asymmetric pattern in comparison with a symmetric pattern.

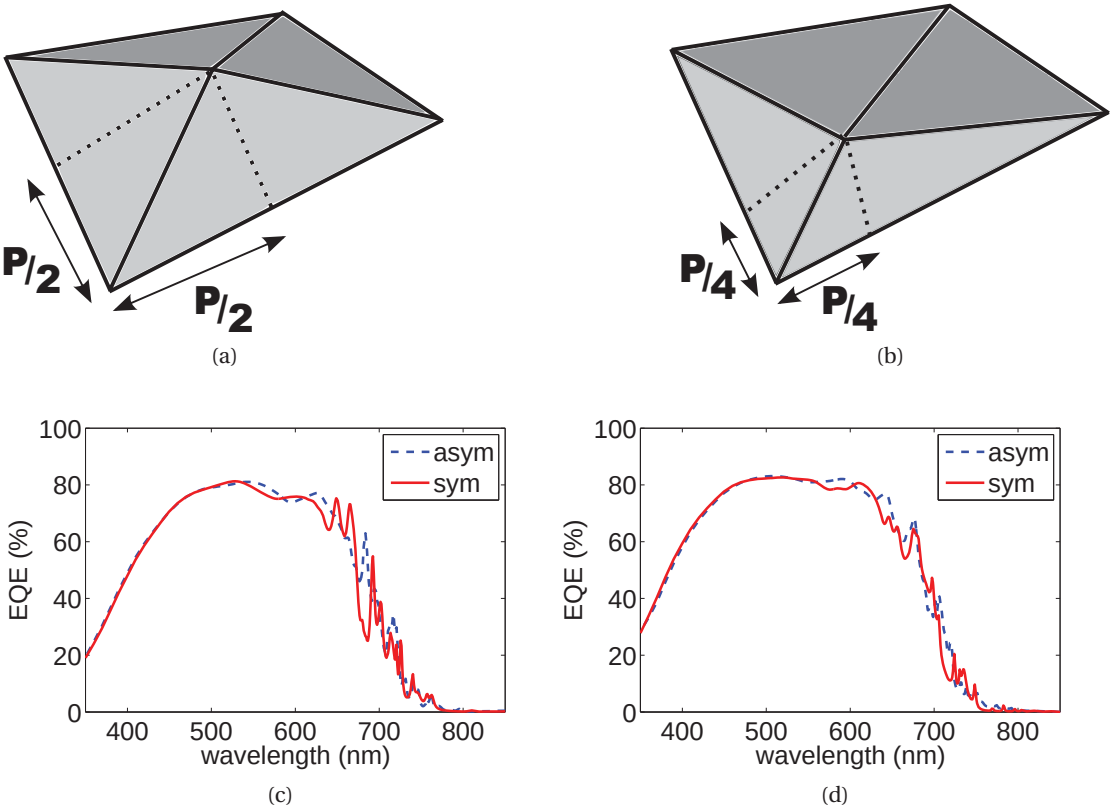

Figure 5.20: Effect of grating symmetry on the EQE of the cell with an Ag back-reflector. (a): A period of the symmetric grating, (b): A period of the asymmetric grating, (c): Grating depth is 150 nm, (d): Grating depth is 300 nm.

In summary, in this chapter we studied the impact of geometrical changes on the absorption in thin-film silicon solar cells. The difference of the previous chapter and this one is that in the former, generic structures were considered and optical limits were obtained, but in this chapter specific geometries were considered and analyzed rigorously by electromagnetic simulation. To understand the physics of the solar cell, we primarily used a planar model, and by using the corresponding dispersion diagrams, we investigated the impact of the back-reflector parameters. Specifically we changed the buffer layer material or thickness

to find out its effect on the modal structure of the solar cell. Then we considered a-Si cells based on 1D metallic grating Ag back-reflectors and we investigated the effect of geometrical parameters of the grating on the EQE and J_{sc} over a wide angular range. In general, when the grating becomes deep, diffraction effects become more visible. Asymmetric textures provide higher photoucrrent for a range of angles at the expense of reducing photocurrent for some other angles. Thus, depending on the rangne of angles of interest, the optimal structure may be symmertic or asymmetric. Overall, it seems that the photo-generated current is a complex function of the back-reflector shape, and an optimal shape of back-reflector depends tightly on parameters such as layer thicknesses, materials which are used in the cell, angular range of interest, etc. Specifically, a structure which seems optimal for normal illumination may be non-optimal if other incident angles are considered too. Thus, a general optimization procedure should consider a range of incident angles rather than only a single one. This is often neglected in the existing literature. We also simulated symmetric and asymmetric back-reflectors based on 2D gratings under normal illumination. Asymmetry and depth of the grating increase the photocurrent for these 2D gratings under normal incidence.

6 Suggested alternative structures

6.1 Unbuffered metallic back-reflectors

Using a back-reflector can improve both photocurrent and efficiency of a solar cell [17]. If this back-reflector is metallic, it can support a plasmon which may seem an interesting means to realize high efficiency solar cells [119]. Plasmonics provides a way to localize light very tightly at a metal-dielectric interface. As mentioned in section 4.4, high confinement of light to the active layer of the cell is a necessity to obtain high photocurrent. Theoretically, plasmonics seems useful in the design of very thin solar cells [139] because it fulfills both conditions of high confinement and strong coupling [84]. To clarify whether plasmonics can excel the conventional techniques of absorption enhancement such as interface texturing, research has been done recently, and one of the best plasmonic cells has been fabricated by H. Tan in Delft university [26]. Normally its is observed that to obtain higher photocurrent, we need to suppress the surface plasmon by putting a ZnO buffer layer on the metallic back-reflector [40]. In this section I show that by removing this buffer layer one may gain a considerable amount of photocurrent over a wide band of wavelengths from before 500 nm to after 600 nm; hence, there is no reason to deposit the buffer layer, at least from the optical point of view. I show that the effect is observed in both TE and TM polarizations, thus, it may not be attributed necessarily to the presence of a surface plasmon, because in TE polarization no surface plasmon exists.

It is important to note that a plasmon intensity peaks at the interface between a metal and a dielectric and decays into both of them although the decay is sharper in the metal. Thus, to benefit from the plasmonic absorption maximally, the absorber should be put as close as possible to the metallo-dielectric interface. In most of the publications regarding plasmonic solar cells, a buffer layer is put between the metal surface and the silicon layer, as depicted in Fig. 6.1a. This buffer layer shifts the optical bands of the plasmonic mode such that the mode occurs between light line of air and silicon. Thus, the mode is no longer plasmonic because it is converted into a guided mode. To investigate a truly plasmonic solar cell, we consider the following stack: ITO (60 nm), p-Si (20 nm), i-Si (230 nm) and Ag as the back-reflector,

(a) (b)

Figure 6.1: (a) Schematic view of a cell with buffer layer; The layers are ITO, p-Si, i-Si, n-Si, ZnO and Ag respectively, (b) The same cell when there is no ZnO buffer and n-Si layers. Light comes from below and the back-reflector is on top

which is schematically shown in Fig. 6.1b. The ZnO and n-Si layers are eliminated to allow absorption of the surface plasmon. The cell includes a Schottky junction at the back side. To allow efficient light-coupling, the back-reflector is designed in the form of a sinusoidal grating with the period of 500 nm and peak to valley height of 140 nm. Elimination of the n-Si layer results in poor carrier collection and the photocurrent has to be collected by applying a reverse bias in the experiments. Fig. 6.2 shows the cell's EQE in TM polarization predicted by RCWA optical simulations. Absorption in the p-Si layer is the main cause of EQE loss at short wavelengths but this layer absorbs less as the wavelength increases. Absorption in the Ag back-reflector shows a opposite behavior; at short wavelength it is negligible but as the wavelength increases, it becomes more important. Absorption in the ITO layer and reflection from the cell show a trend similar to the absorption in Ag; they are generally larger at longer wavelengths. The dips in the reflection are associated with the presence of modes in the structure. The dips at 650 and 700 nm are related to excitation of modes which are localized mainly in the i-Si layer, thus, they enhance EQE. At longer wavelength, for example at around 700 nm and at 750 nm, the dips are due to the excitation of surface plasmons, which are absorbed more in Ag. Note also that the variation of reflection at around 750 nm is almost perfectly compensated by the change in absorption in Ag. However, at 700 nm, absorption in Ag does not fully compensate reflection variations. The reason is that at 700 nm Si can also absorb light to some extent. There are three distinguishable resonances at the wavelengths of 525, 585 and 660 nm. The intensity profile at each one of these resonances is plotted in Fig. 6.3. It appears that for the resonances at wavelengths of 525 and 585 nm the back-reflector geometry plays a decisive role. As Fig.s 6.3a and 6.3b show, in these wavelengths the peak of the sinusoidal profile concentrates the field amplitude. The third peak which occurs at 660 nm is different from the first two in the sense that it is similar to a hybrid mode which includes both a guided mode and a plasmonic component (Fig. 6.3c) as noticeable by the increased field amplitude at the Si-Ag interface. At longer wavelength, the plasmon increases absorption in Ag and therefore the EQE decays after 660 nm. The intensity profile at 700 nm

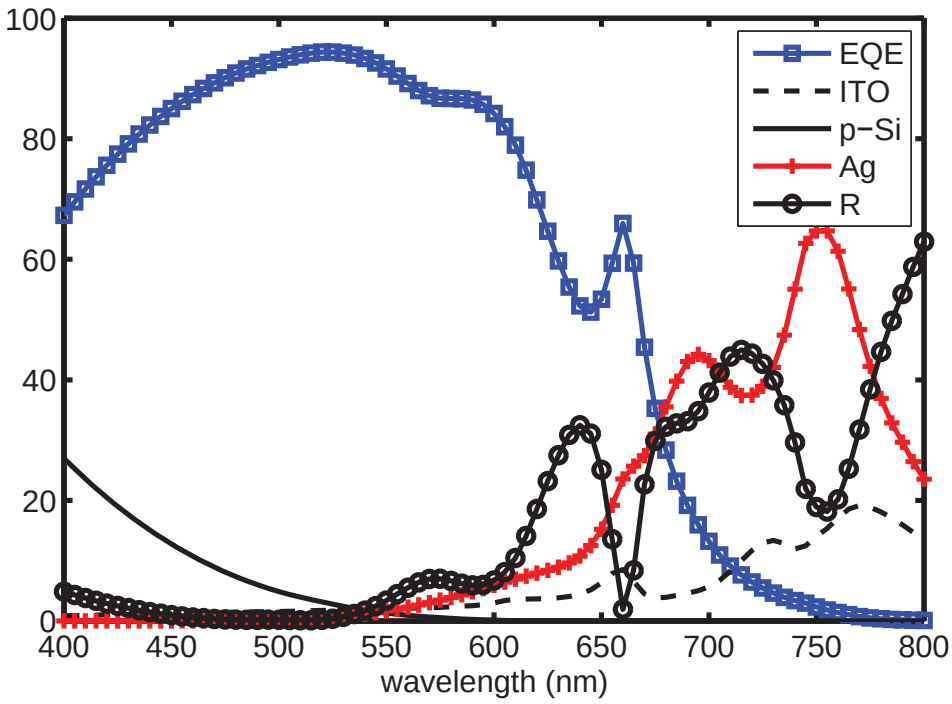

Figure 6.2: TM polarized EQE of the plasmonic cell based on a silver grating. Sequence of layers from top to bottom is ITO (60 nm), p-Si (20 nm), i-Si (230 nm) and Ag. The peaks at 525, 585 correspond to interferences and the tail after 660 nm corresponds to a plasmon. The peak at 660 nm is the signature of guided mode.

(Fig. 6.3d) shows the intensity peak is at the metallic interface which is the characteristic of a plasmonic mode.

To give an idea about the absorption enhancement provided by the plasmonic and interference effects in the cell, I simulate the same structure while it also includes a ZnO (60 nm) and a n-Si (20 nm) layer on Ag and the rest of the layers are as before. Fig. 6.1a shows the geometry under investigation and Fig. 6.4 shows its EQE. The guided-mode resonance is shifted towards longer wavelengths in the presence of ZnO layer. As shown in Fig. 6.4, over a wide band range from 450 to 620 nm, the resonances increases the EQE more effectively when the buffer layer is absent. Fig. 6.4 also shows the EQE of a the plasmonic cell when i-Si layer thickness is reduced to 80 nm. This value is chosen because normally thinner cells suffer dramatically from shunts. Although the i-Si layer is significantly thinner in the latter cell, EQE drop is not as dramatic. At around 600 nm, this thin cell even overtakes the cell with ZnO buffer layer thanks to exploiting the appearance of an resonance similar to the one discussed for the primary plasmonic cell.

In Fig. 6.5 the absorption in individual layers of the plasmonic cell and total reflection from the cells are plotted. As depicted in Fig. 6.5a, in the wavelength range under 600 nm, absorption in the top layers (p-Si and ITO) is almost the same in both the plasmonic cell and

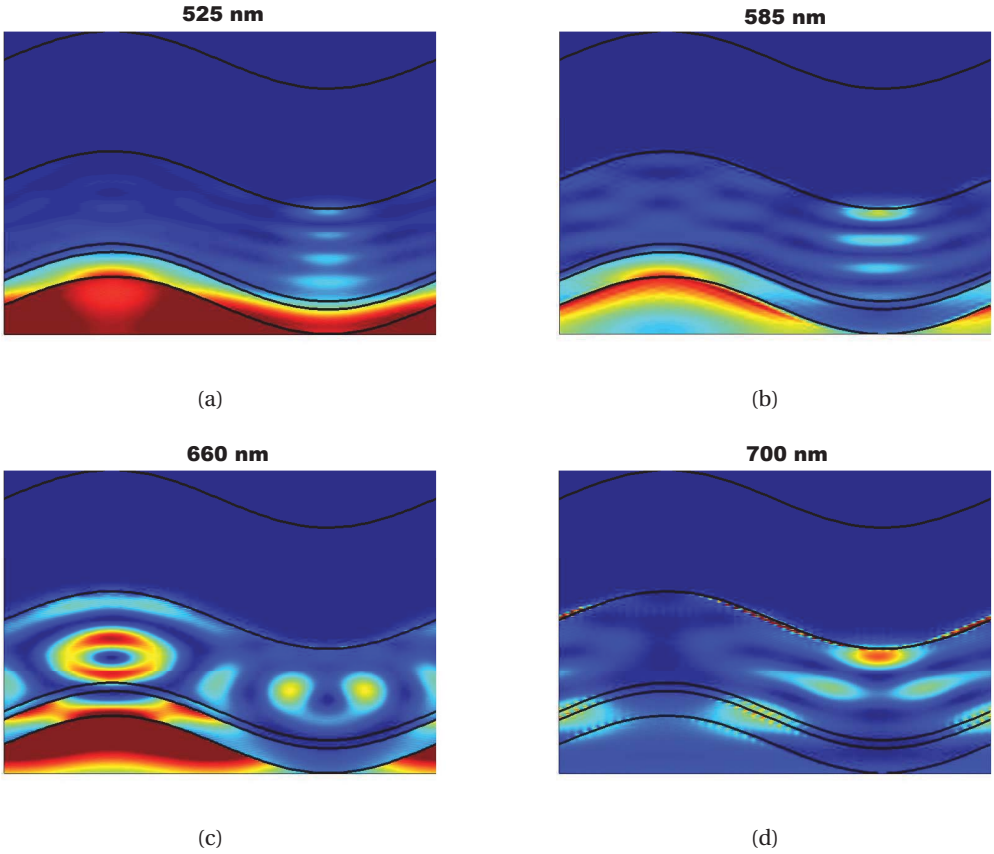

Figure 6.3: TM polarized Intensity profile of the plasmonic solar cell at the wavelengths of 525 nm (a), 585 nm (b), 660 nm (c) and 700 nm (d). Light enters the cell from bottom.

the cell with buffer layer. Absorption in the bottom layers demonstrates a different behavior. Fig. 6.5b shows that in the cell with buffer at short wavelengths absorption in the n-Si layer is almost equal to absorption in the Ag back-reflector. As the wavelength increases, these layers absorb more light. At around 580 nm, n-Si and Ag layers eat up about 20 percent of the incident energy. After 600 nm, absorption in the n-Si layer decreases because of approaching the band gap of Si. Contrary to the n-Si layer, the ZnO layer does not absorb that much over the entire wavelength range of interest thanks to its almost zero extinction coefficient. In the plasmonic cell, the Ag back-reflector does not absorb a lot at short wavelength. Surprisingly the back-reflector of the cell with buffer absorbs more light at wavelengths shorter than 650 nm. At longer wavelength, however, it absorbs much more than the case where ZnO buffer is used. But, this seems not an advantage for the cell with buffer because there is an exchange of energy between reflection from the cell and parasitic absorption over other layers of the cell. As shown in Fig. 6.5c, variations in the absorption in Ag is compensated mainly by reflection changes. The rest of the energy is absorbed by the ITO layer.

My colleague Karin Söderström fabricated this cell and we measured the EQE of the cell. Bias of -0.5 V was applied to the cell for carrier collection. Fig 6.5d compares the experimental

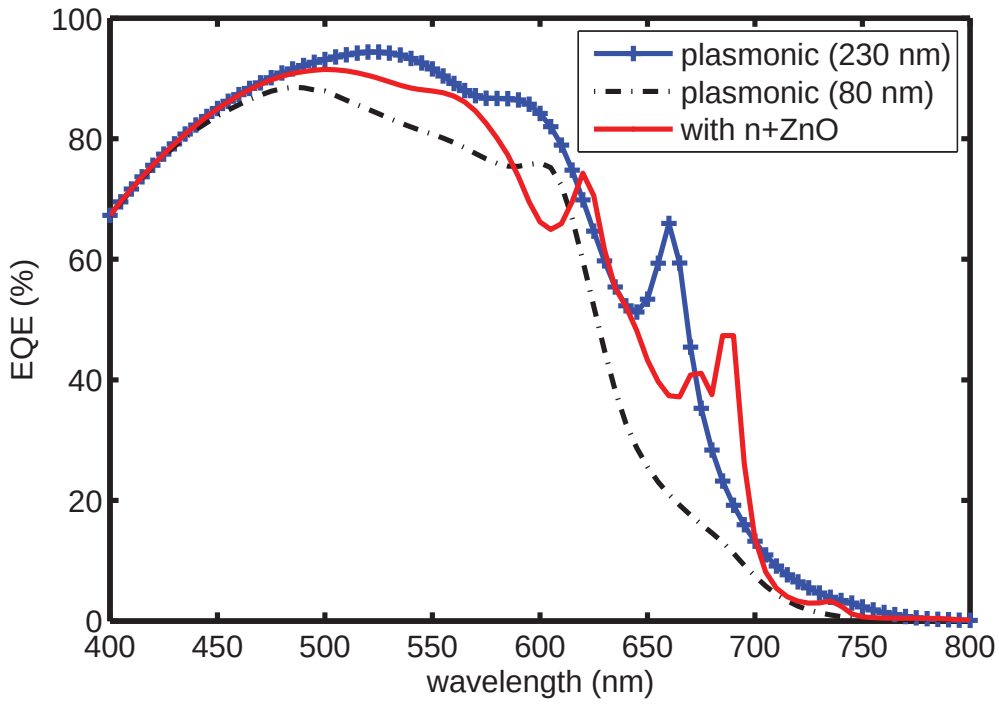

Figure 6.4: Comparison of EQE of the plasmonic cell with two i-Si thicknesses of 230 and 80 nm and a cell which has ZnO (60 nm) and n-Si (20 nm) on top of Ag. The rest of the layers are identical. The results are plotted for TM polarization

EQE and the EQE obtained from simulation in the wavelength range of interest. At long wavelengths after the peak at 660 nm, the simulation and the experimental results fit very well revealing that the carriers generated by the surface plasmon have been successfully collected. Contrarily at wavelengths shorter than 600 nm, there is a difference between experiment and simulation which is attributed to the existence of shunts in the cell. We hope that by proper fabrication of a cell, it is possible to approach the EQE predicted by simulation.

Up to now we have just considered the TM polarized response of the cells. Because solar illumination is not polarized, it is important to consider behavior of the cells under TE polarized light as well. Fig. 6.6 compares the EQE of the plasmonic cells with i-Si layers of 230 and 80 nm thickness to the cell with buffer layer. The cell with 80 nm i-Si layer has the lowest EQE due to the too small thickness of the active absorber layer. However, the two other cells show a relatively similar optical response. At the wavelength shorter than 550 nm, both cells have an almost equal EQE. At longer wavelengths their EQE includes peaks and dips as a signature of optical resonances.

The remarkable difference between the TE-polarized EQE of the cells at around 600 nm can be understood better by comparing intensity profiles. Fig. 6.6 shows the intensity profile for the three cells at the wavelength of 595 nm which corresponds to the peak of EQE for the plasmonic cell (i-Si= 230 nm). In all cases, the metallic back-reflector reflects the light

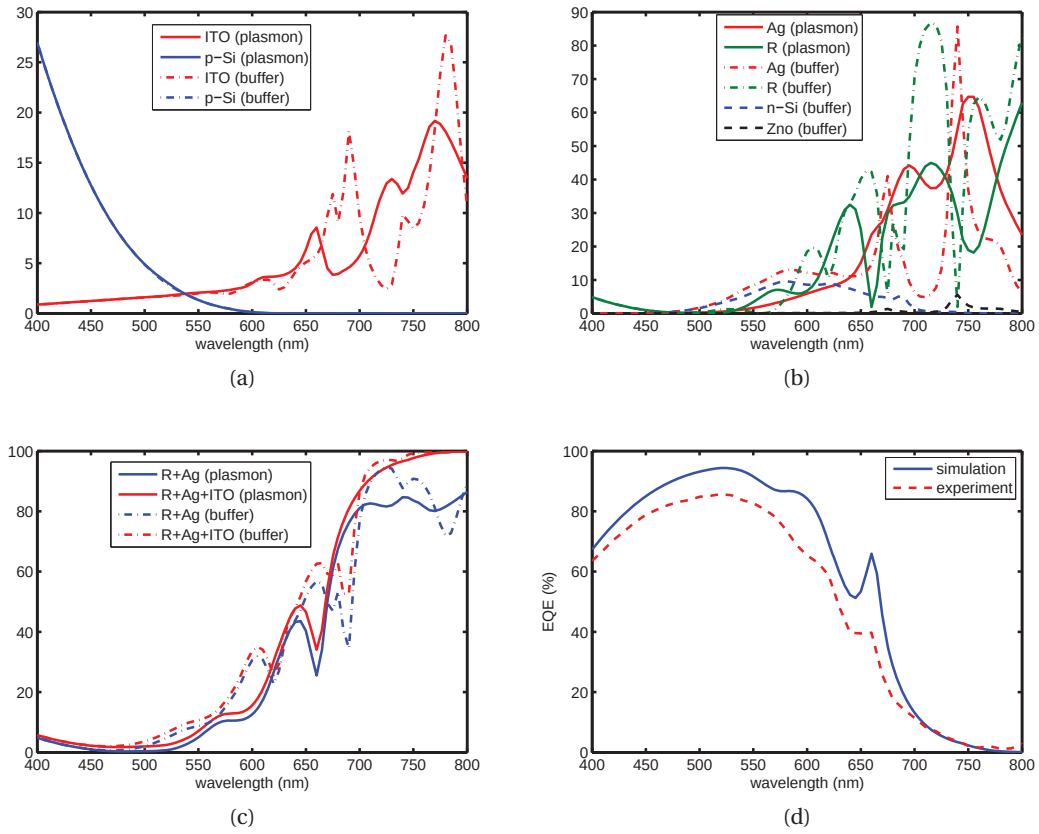

Figure 6.5: (a) Absorption in the top layers (p-Si and ITO) of the plasmonic and the cell with buffer layer (b) Total reflection and absorption in the bottom layers (the layers under the i-Si layer) of the plasmonic and the cell with buffer layer. (c) The trade-off between reflection and absorption in electrodes of the plasmonic and the cell with buffer layer. (d) Comparison of the simulation result and the experimentally-obtained EQE under -0.5 V bias for the plasmonic cell. All parts from (a) to (d) represent results under TM-polarized light.

back into the cell. However, for the thin cell and the cell with buffer an intensity peak occurs on a doped Si layer and therefore, reduces the EQE. For the thick plasmonic cell there is an intensity peak on the p-Si layer but it is rather weak and is less-pronounced.

It is instructive to compare optical absorption in the two different polarizations for the same cell. This is done in Fig. 6.7. Fig. 6.7a shows the EQE obtained in both polarizations for the plasmonic cell (i-Si= 230 nm). It is observed that except at short wavelength range under 500 nm, TE polarized illumination permits higher EQE. Interestingly the peak at 600 nm is even more pronounced in TE than in TM polarization. At longer wavelengths, EQE is covered by a tail of resonances which permit enhancing EQE. For the thin plasmonic cell (Fig. 6.7b), EQE is larger in TM polarization than in TE polarization except at around 650 nm where there is well-pronounced guided-mode resonance in TE-polarized EQE. Also at around 540 nm, there is a peak in the TE-polarized EQE which may be attributed to optical interference. The cell

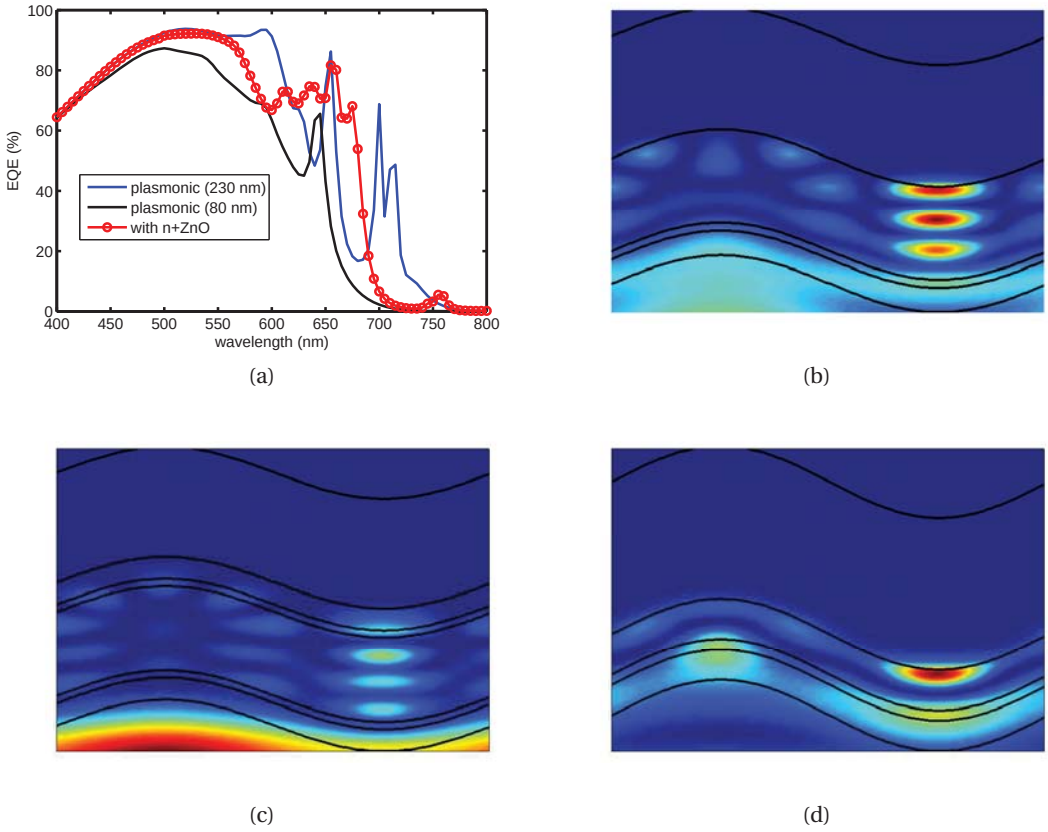

Figure 6.6: (a) Comparison of EQE of the plasmonic cell with two i-Si thicknesses of 230 and 80 nm and a cell which has ZnO (60 nm) and n-Si (20 nm) on top of Ag. The rest of the layers are identical. (b) Intensity profile at 595 nm for the plasmonic cell. (c) Intensity profile at 595 nm for the cell with buffer. (d) Intensity profile at 595 nm for the thin plasmonic cell (i-Si = 80 nm). The results are plotted for TE polarization

with buffer layer behaves similarly to the thick plasmonic cell: TE-polarized light results in lower EQE at short wavelengths and in higher EQE at longer wavelengths. Specifically, the TE-polarized EQE is significantly larger than the TM-polarized one at around 650 nm where a number of guided-mode resonances improve absorption in Si. Corresponding resonances seem to be shifted to slightly longer wavelengths in TM polarization. Also at around 550 nm, the TE polarized illumination results in higher absorption in silicon. To ease the comparison, we divide the EQE obtained from the two different polarizations for each cell.

$$r(\lambda) = \frac{EQE_{TM}}{EQE_{TE}}. \tag{6.1}$$

Fig.6.7d shows the values of r as a function of incident wavelength. For all cells r is slightly above unity at short wavelengths. At wavelengths longer than 670 nm, the thin plasmonic cell can provide larger r. Fig. 6.7 reveals different messages. First, at short wavelengths, TM

polarized EQE is slightly higher than the TE polarized one. This can be attributed to the difference of the electromagnetic boundary conditions in the two polarizations. Second, as a cell becomes very thin, TM-polarized light can enhance the EQE more than TE-polarized light. However, this does not mean that absorption is high in TM polarization at long wavelengths. EQE is very low in both polarizations but their ratio, r, can be large.

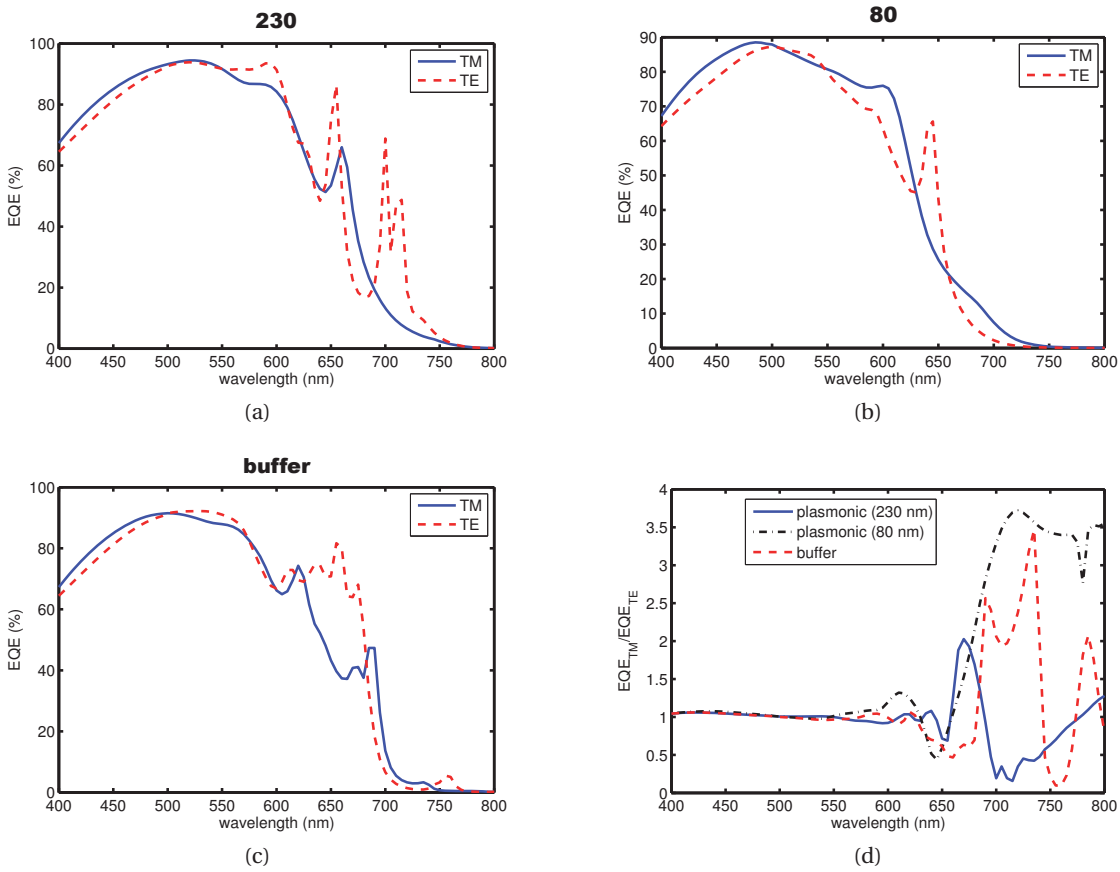

Figure 6.7: (a) TE- and TM-polarized EQE for the plasmonic cell with 230 nm i-Si, (b) TE- and TM-polarized EQE for the plasmonic cell with 80 nm i-Si, (c) TE- and TM-polarized EQE for the cell with the ZnO buffer layer. (d) The EQE ratio ($r = \frac{EQE_{TM}}{EQE_{TE}}$) for the three cells.

One problem with the mentioned unbuffered geometry can be lack of a strong electric field inside the i-layer to collect the generated carriers. To prevent these problems, it can be useful to deposit an n-Si layer on top of the Ag back-reflector before the deposition of the i-Si layer. While keeping in mind that it is required to check the validity of these guesses in experiment, it is interesting to investigate the impact of deposition of an n-Si layer on the Ag grating at least from the optical point of view.

Fig. 6.8 shows the effect of the presence of the n-Si layer between the Ag back-reflector and the i-Si active layer in both TE and TM polarizations. The horizontal lines show the short circuit current density (J_{sc}) at the presence of a 60 nm ZnO buffer layer. Overall, J_{sc} is larger for

TE polarized light. Elimination of the buffer layer improves the photocurrent regardless of polarization. As the thickness of the n-Si layer is increased the photocurrent drops. The reason is that as depicted in the field profiles of Fig. 6.6 and Fig. 6.3, the maximum of intensity occurs close to the metallic interface. Therefore, if carriers generated in the very close proximity of this interface cannot be collected efficiently because of recombination, photocurrent should decrease. At a n-Si layer thickness of about 9 nm, the photocurrent of the cells with and without buffer layer become equal. For thicker n-Si layers, the cell with ZnO buffer results in higher photocurrent.

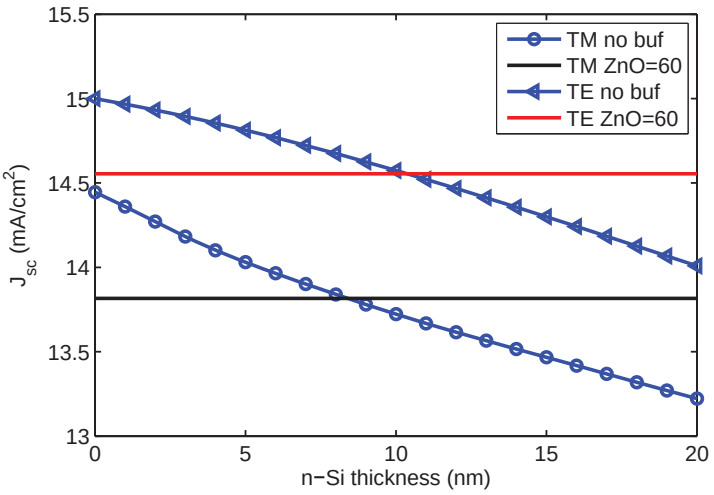

Figure 6.8: Comparison of the J_{sc} of the cells with and without buffer layer. For the cell without buffer, an n-Si layer with variable thickness is assumed between the i-Si layer and the Ag back-reflector. The rest of the layers are identical. The results are plotted for TM polarization

6.2 Embedded nano-particles or nano-wires

In typical amorphous silicon cells, all the layers are considered continuous and almost conformal. As a result, a cell's scattering properties depend tightly on the growth template design. It is true that fabrication of a cell with uniform conformal layers may be easier, however, it seems that these condition do not allow optimal absorption enhancement in a solar cell. By adding other degrees of freedom to the design criteria, it can be possible to scatter light more efficiently and thus increase the photocurrent of a cell.

To change the conformality condition, an idea is to put nano-particles in the layers of a cell. These particles can be put in different layers of a cell as depicted in Fig. 1.6. Let us consider a typical a-Si solar cell based on a metallic substrate. These particles can be put in any of ZnO, i-Si or ITO layers. Special care must be taken not to destroy the electronic properties of a cell. To comply with this, the choice of material for the nano-particles and the fabrication process should be done carefully. We assume that these points can be addressed properly and we focus on the optics of these solar cells including dielectric nano-particles.

Assume a thin film amorphous silicon (a-Si) solar cell with a geometry similar to the one depicted in Fig. 6.9. We study the optical impact of the nano-particles on light absorption in the cell with RCWA calculations. To simplify the calculations, we assume a two-dimensional (2D) geometry. Besides, we consider ZnO nano-spheres, which in 2D means nano-wires with cylindrical cross-section. We take into account the layers in the intrinsic silicon (i-Si) layer. Furthermore. we assume in-plane incidence which helps separating the problem into two distinguished polarizations. The TE/TM polarization is the case where the electric/magnetic field is along the geometrical invariance direction. Finally we consider that the particles are arranged into a 1D periodic form with a period of 500 nm.

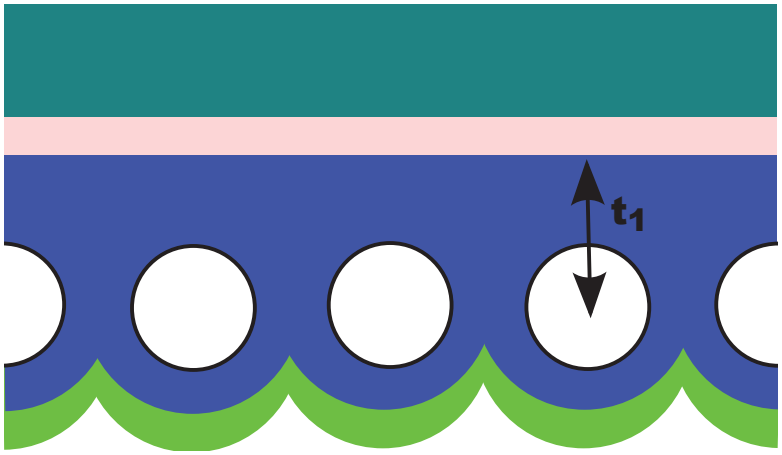

Figure 6.9: An a-Si cell with nano-particles inside the i-Si layer. The particles also introduce a texture in the front layers. Back-reflector is on top.

Fig. 6.9 shows schematically a cell with a nano-particles inside its i-Si layer. The nano-particles are put at a certain distance from the bottom which can be obtained based on their particle radius. This distance is considered here according to the following equation.

$$t_1 = \left(d_{i-Si} + D_{eff,particle}\right)/2 \tag{6.2}$$

where d_{i-Si} is the i-Si layer thickness, $N_{particle}$ is the number of embedded nano-particles in each period, and $D_{eff,particle}$ is the effective diameter of this particle- layer which can be expressed as

$$D_{eff,particle} = N_{particle} \times \pi r^2_{particle}. \tag{6.3}$$

In other words, $D_{eff,particle}$ is the volume that the particles occupy inside the cell. The top layers are considered to be textured as depicted in Fig. 6.9. To form these texture, we consider them initially to be flat and with a distance imposed by the layer thicknesses as depicted in

Fig. 6.9. Then we assume that the nano-particles shift the layers to a radius equal to

$$r_t = r_{particle} + \begin{cases} d_{i-Si}/2 + d_{p-Si} + d_{ITO} & \text{first interface} \\ d_{i-Si}/2 + d_{p-Si} & \text{second interface} \\ d_{i-Si}/2 & \text{third interface} \end{cases} \tag{6.4}$$

Finally, we shift these three top layers such that the whole volume of ITO- p-Si and i-Si remains constant in the cell. This latter constraint is applied to guarantee that the amount of material in each layer remains constant. This is important to ensure that the probably absorption enhancement is not because of physically thicker layers.

Assuming a flat back-reflector, embedding the nano-wire changes the optical properties of the cell due to at least two different effects: introduction of surface texture which changes reflection from the cell, and appearance of new optical modes in the dispersion diagram of the cell. To distinguish these two effects as far as possible, we consider also a cell with the same surface texture in the top layers. The bottom layers are flat in both cases with and without nano-particles.

Fig. 6.10 shows the J_{sc} (mA/cm^2) in the cases with and without nano-wires, for both TE and TM polarizations. The vertical and the horizontal axes show the diameter of the nano-wires and the number of the nano-wires respectively. The center of all of the nano-wires is considered to be on the same horizontal plane for each case. Fig. 6.10a shows the J_{sc} of the cells without nano-wires in TE polarization; increasing the number of particles (wires) in this case means changing the front texture correspondingly. This reduces the photocurrent based on Fig. 6.10a. When the nano-wires are present (Fig. 6.10b), this situation changes and a higher number of wires may result in higher photocurrent, for example for a diameter of 100 nm. In TM polarization, a similar trend is observed for the cases with and without nano-wires (Fig. 6.10c and Fig. 6.10c). An interesting point is that the presence of nano-wires improves the photocurrent in TM polarization even for small diameter of wires, regardless their number.

Since the highest J_{sc} is observed when only one wire is present per period, we focus on this case here. Figs. 6.11a and 6.11b show the effect of presence of the wires on J_{sc} in TE and TM polarization respectively. In TE, the presence of the wires improves the photocurrent for all diameters. In TM, the presence of the wire enhances the J_{sc} only when its diameter is close to 300 nm, or very large, close to 500 nm. However, the most prominent enhancement is at around 300 nm, which is close to 1 mA/cm^2.

Because of the difference of effect of the nano-wires on the J_{sc} in the TE and TM polarizations, and also because sunlight is not naturally polarized, we consider the unpolarized case too. In the latter case J_{sc} can be obtained by taking the average of the TE and TM results. Fig. 6.12a and Fig. 6.12b show the J_{sc} under unpolarized light respectively for when the wires are not and are present. Almost regardless of the number and diameter of wires, the presence of wires enhances the J_{sc}. The highest J_{sc} is obtained for only one wire per period, and a diameter of

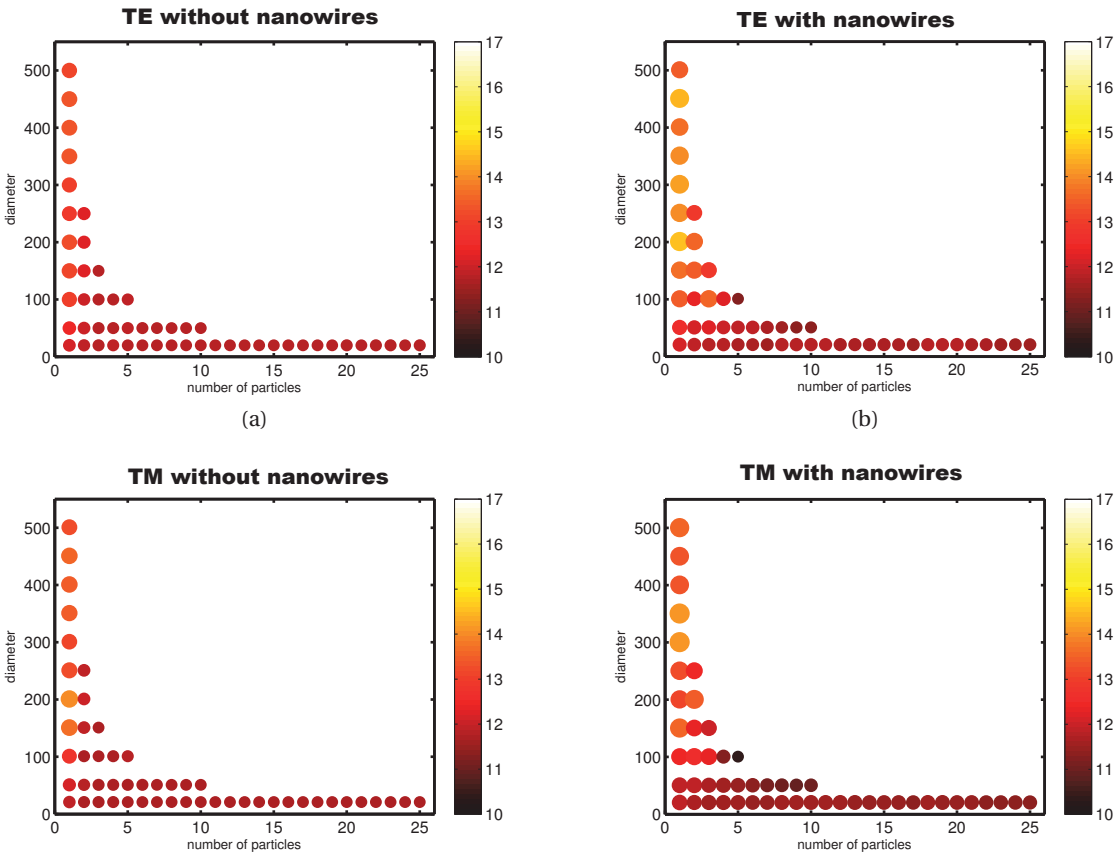

(a) (b) (c) (d)

Figure 6.10: J_{sc} (mA/cm^2) as a function of the number and the diameter of the nano-wires (a): TE without nano-wires, (b): TE with nano-wires, and (c): TM without nano-wires, (d): TM with nano-wires.

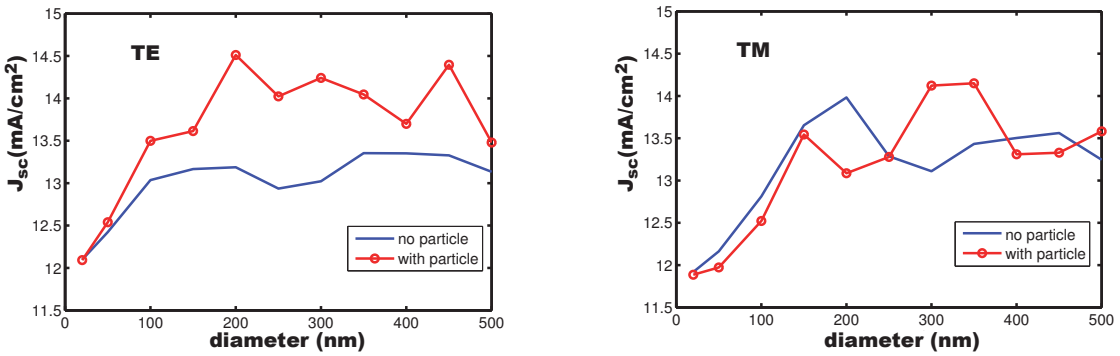

(a) (b)

Figure 6.11: J_{sc} (mA/cm^2) for only one particle per period in (a): TE polarization, (b): TM polarization.

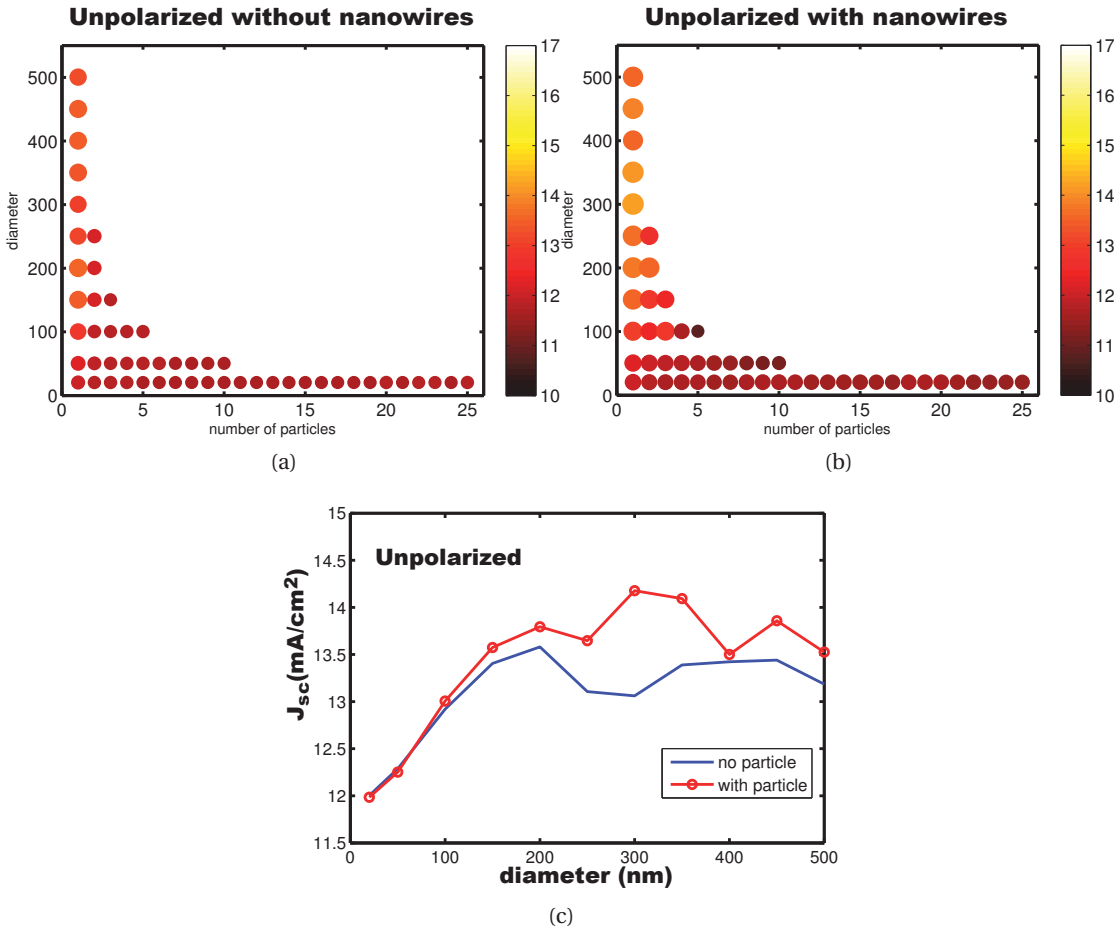

Figure 6.12: Unpolarized J_{sc} (mA/cm^2) as a function of the number and the diameter of the nano-wires (a): without nano-wires, (b): with nano-wires. (c): J_{sc} (mA/cm^2) for only one particle per period under unpolarized light.

around 300 to 350 nm. Fig. 6.12c shows the J_{sc} for only one wire per period, in the absence and presence of wires. The most significant improvement is obtained for a diameter of 300 nm, which also brings the largest J_{sc}. For small wires, the J_{sc} remains almost unchanged.

To give the reader a feeling of the enhancement introduced by the nano-wires, the EQE of the cell with $d = 300$ nm and $P = 500$ nm is plotted in both polarizations for the two cases of with and without nano-wires in Fig. 6.13. In both polarizations, the presence of nano-wires enhances the EQE over the almost whole wavelengths from 550 to 700 nm.

One possible concern about the nano-particles or nano-wires is that they may interfere with carrier collection. This can happen in different scenarios. First, formation of voids around the particle and the improper material quality at the particles interface may form defects an thus cause problems for carrier collection. Second, they can reduce the influence of the internal electric field on the generated carriers and deviated carrier transform inside the cell

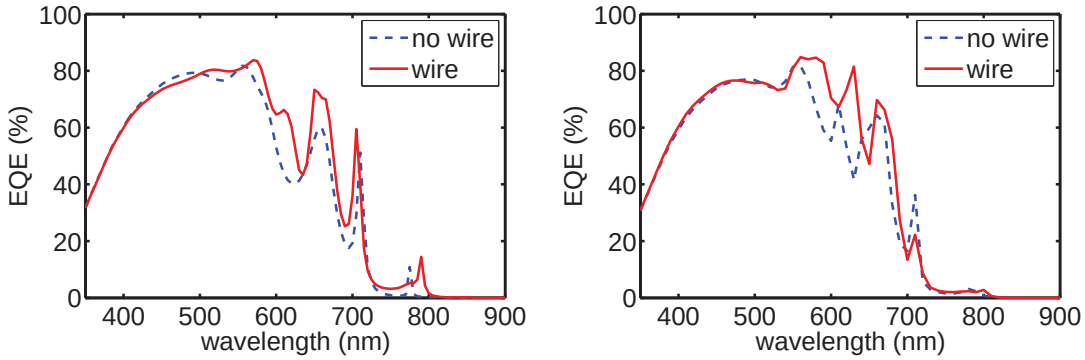

Figure 6.13: Comparison of the EQE of the cells with and without nanowires. Nanowire diameter is 300 nm and period of the nano-wire array is 500 nm. (a): TE polarization, (b): TM polarization. Normal illumination is considered.

from its desired form. Third, the nano-particles increase the cell thickness and thus, it seems that a stronger internal field will be needed to collect the carriers. One should pay attention at these points in the fabrication of these cell. Finally, it should be possible to find an optimum point where the nano-particles enhance absorption in an a-Si cell optically without changing its electronics that much.

In summary two types of unconventional structures were studied in this chapter. First an a-Si cell without a buffer layer was investigated. The existence of this buffer layer can avoid appearance of a plasmon which is absorbed strongly in the metallic back-reflector. Despite this positive effect, the buffer layer has a disadvantage: it attracts the electromagnetic energy towards itself, thus reduces confinement of the wave to the Si layer. This eventually reduces the EQE. In this chapter we have shown by rigorous calculation that elimination of this buffer layer in a-Si cells can increase photocurrent. The second structure which was studied in this chapter is an a-Si cell in which a periodic array of ZnO nano-wires are embedded. It is shown that considering the same interface texture for the different layers of the cell, and also assuming that the total volume of different layers (except the added ZnO wires) is preserved, the wires can enhance J_{sc}. Optimization of nano-wire radius and period of the nano-wire array shows that under normal incidence, for a period of 500 nm and for a nano-wire diameter of 300 nm, the J_{sc} becomes maximal.

7 Conclusions and outlook

In this thesis, absorption enhancement in thin-film solar cells is studied from an optical perspective. Both approximate and exact simulations are used for the physical understanding and optimization of thin-film amorphous silicon (a-Si) solar cells. The simulations are done mainly with the codes which I developed during the PhD.

Optical properties of a-Si cells depend tightly on the their interaction with light at nanoscale. This means that ray optics approximation is no longer valid for the optical analysis of these cells and rigorous calculation is a necessity, especially when it comes to metallic structures and plasmonics. In the literature, different numerical methods and software packages are used for this purpose. Unfortunately, most of these methods are either memory-hungry or time-consuming. Often, the mentioned problems are bypassed by applying coarse computational grids, which results in numerical error and produces unreliable results. Unfortunately, the results of such simulations are very rarely benchmarked in the literature. A method which can simulate thin-film solar cells in a fast and accurate way is thus of interest for understanding, design and optimization of solar cells.

First, I implemented codes based on the rigorous coupled-wave analysis (RCWA) method. Chapter 2 and 3 of the thesis explain briefly the electromagnetic theory for the analysis of thin-film solar cells and the basics and some details of the implemented methods. I applied different variants of RCWA which are explained in chapter 3. Finally it seems that a combination of the finite element method (FEM) and the RCWA can be an (almost) optimal method for the optical simulation of solar cells. The eigenvalue problem can be solved in each slice by a FEM solver, and the boundary conditions can be applied as in the conventional RCWA. Since the mesh generated by the FEM in each two slices may be different, a common basis is required to link the modes of the slices, for example trigonometric functions as in Fourier expansion.

In chapter 4 of the thesis, the limits of light absorption enhancement and efficiency increase in thin-film solar cells are investigated. The limits were obtained for both idealized structures, for example a dielectric slab, and more realistic cases such as a full stack of layers of

an a-Si cell over broad angular and wavelength range. The considered textures were periodic in one or two directions. Hexagonal gratings were found to enhance absorption more significantly than gratings with square geometry. It was also found that depending on the period of the texture, the optimal incidence angle can change. For these studies, the coupled-mode theory (CMT) was used, which is a common approach for the physical understanding of resonant systems. I have extended the application of this method to thin-film solar cells with wavelength-scale periodic texture. Based on the summary of the existing literature regarding the limits of light absorption and efficiency in solar cells, which is presented in chapter 4, it seems that light absorption in a solar cell may be enhanced by excitation of surface modes, for example surface plasmons, a wavelength-scale periodic coupler, and small thickness of the cell. Complying with these requirements may result in boosting cell efficiencies beyond the present values.

Guided modes are studied in chapter 5. Guided modes of a-Si cells are extracted in an equivalent planar model. The effect of spacer material and thickness are studied. Furthermore, the impact of back-reflector geometry on the photocurrent of a-Si cells in n-i-p configuration is investigated over a broad angular range. It is observed that a texture which seems optimal under normal incidence of light can be non-optimal for other incident angles. Thus, it is necessary to conduct studies of solar cells also under oblique incidence; unfortunately this is often neglected in the literature. Three dimensional simulations of solar cells based on 2D periodic gratings (chapter 5) reveal that using asymmetric back-reflectors can enhance EQE similarly to increasing the i-Si layer thickness.

Chapter 6 discusses two non-conventional configurations for thin-film a-Si cell. In the first geometry, which is an a-Si plasmonic cell, the buffer layer is removed and the thickness of the n-doped Si layer is changed. It is observed that for n-Si thicknesses below 10 nm, the plasmonic cell can excel a conventional a-Si cell from the optical point of view. From the electronic point of view, this should be sufficient to create the internal field that is necessary for the collection of photogenerated charge carriers. In our experiments, a-Si thickness cannot be less than 80 nm. Thinner a-Si layers will result in shunts. However, a very thin cell may have a high efficiency, potentially higher than the efficiency of thick cells. It seems interesting to investigate the efficiency of solar cells with an absorber which is very thin, in the range of a few nanometers.

The methods and results that were used and developed in this thesis to find the upper bounds of light absorption can be applied to a vast variety of opto-electronics devices. Primarily they have been used to study various types of solar cells, with different cell thickness and light absorber materials. The applicability of these methods goes far beyond Si cells; some examples are III-V cells, polymer cells, dye synthesized cells, CIGS cells, etc.

As it was mentioned in section 1.4, making a solar cell very thin may reduce its parasitic effects and thus increase its efficiency. From an electronic point of view, this may happen thanks to the reduction in the amount of non-radiative recombination e.g. Auger recombina-

tion. Such very small cell thicknesses may also support strong light absorption if the device is designed properly. To obtain the absorptive capabilities of such thin-film devices, a discrete model similar to the one presented in this thesis can be helpful, especially if the scale of the applied texture is in the order of wavelength. By considering the mechanisms responsible for non-radiative recombination in a cell, it can be possible to extend the method to obtain the limits of the cell efficiency.

Applicability of the mentioned methods is not restricted to solar cells. Electromagnetic reciprocity reveals that in the same way that light can couple into the optical modes of a device, the electromagnetic energy of these modes can couple to outside radiation. The second case is related to devices which radiate electromagnetic waves, for example Light Emitting Diodes (LEDs). A difference of solar cells and LEDs is that the operation wavelengths of a solar cell and an LED are not the same. Furthermore, economical and technical constraints of their fabrication can be different. Nevertheless, there are intrinsic resemblances between the efficient absorption of light in a solar cell and emission of light from an LED, and similar methods can be applied to increase quantum efficiency in both cases. More specifically, an appropriate choice of texture morphology and device thickness can increase an LEDs efficiency. To understand the influence of such parameters, and to be able to propose structures which can improve the efficiency of an LED, the methods used in this thesis can be adapted to the corresponding case. It should be mentioned that efficient absorption or emission of electromagnetic energy covers a much wider domain of research than solar cells or LEDs; different types of radar systems, radiative cooling, and radiators of electromagnetic energy at non-optical wavelengths are some example. The innate similarities between these diverse applications make the methods that were used in this thesis applicable to a broad domain of research and application.

Despite the studies on solar cell design and fabrication, there seem to be a remarkable potential to boost light absorption in solar cells. At present, parasitic absorption is a bottleneck to exploiting sunlight energy to the full extent. Making more transparent doped layers is thus of critical importance, especially when very thin films are desired. It seems worth investigation whether it is possible to enhance absorption at short wavelength geometrically, without using highly-transparent doped layers. TCO layers are another limiting parameter of the present solar cells. Even if these TCO layers are completely transparent, they reduce energy confinement to the Si layer. If the cell is very thin, this effect can have a remarkable effect on the EQE. Thus engineering the opto-electronic properties of these TCO layers seems of importance for Si solar cells. Another major constraint is that for high-energy photons with an energy above the band gap energy of the absorber semiconductor, the excess energy is mainly lost in the form of heat. Finding ways to harness this excess energy can be interesting.

Scattering of light by interface textures is still a topic of ongoing research. Independent of the type of the cell, efficient scattering of light can increase light absorption in the cell. Although this has driven both theoretical and experimental research, there are still a lot of questions to respond. One problem to investigate is that associating experiments and simulations seems

difficult especially when the size of the geometrical features goes down. For this purpose, using numerical methods which can model multi-scale structures efficiently seems important. It may be true that for relatively thick cells an exact solution of Maxwell's equations may not be needed, however, as the thickness of the cell goes under several hundreds of nanometers, exact solution of Maxwell's equations may be required to understand the optical properies of the cell.

Plasmonics is a main topic which needs more investigation. At present, it seems that the nanoscale roughness which occurs in practice at the metal/semiconductor interface is a bottleneck of plasmonic and leads to strong absorption of light by the metal. A complementary idea is to harvest the energy which is absorbed by the textured metal in other ways; capturing hot electrons and water-splitting are some examples of the latter choice which are not directly related to photovoltaics but are still in the domain of energy harvesting. If the interface between the metal and the semiconductor can be fabricated with very high quality, then the interesting properties of surface plasmons may become accessible. For the high-quality fabrication of the metallic interface, planar geometry seems preferred. While this appears contradictory to strong coupling of light to the modes of the structure, usually it is observed that at long-wavelength regime, the sum of reflection and absorption in the metal is almost constant. This means that texturing the metal can reduce reflection but the corresponding absorption occurs in the metal, not in the Si layer. Thus to use the surface plasmons in a thin-film solar cell, it seems that (at least primarily) one should try to focus on the fabrication of a very high-quality planar metal-semiconductor interface.

Finally, it seems that there is a large room to improve light trapping in thin-film photovoltaics. To approach the high efficiencies that are predicted theoretically, physics of the different types of thin-film solar cells should be investigated in more detail. Also, related fabrication methods and technologies should be improved. This motivates a global effort to provide abundant, widely-accessible, cost-effective and green enegy in an international scale.

A Radiance definition

Radiance is the amount of electromagnetic power that an emitting surface radiates into a specific solid angle. The unit for radiance is W· sr^{-1}· m^{-2}. It should not be mistaken for spectral radiance which has a unit of W· sr^{-1}· $m^{-}2$· Hz^{-1} or intensity which has a unit of W· m^{-2}. Radiance is a density function and measures the angular dependence of light intensity emitted, absorbed or scattered by an object.

Let us consider $d^2\Phi$ be the power emitted into a solid angle $d\Omega$ by a source with an infinitesimal surface area dA. The radiance L is defined as [140, 141, 142]

$$L = \frac{d^2\Phi}{dA\cos\theta d\Omega} \tag{A.1}$$

A Lambertian scatterer scatters light isotropically, which means that it has the same radiance independent of the angle from which it is viewed. Thus, according to Eq. A.1 its emitted power into the solid angle $d\Omega$ is proportional to $\cos\theta$. This is known as Lambert's cosine law, after the name of Johann Heinrich Lambert.

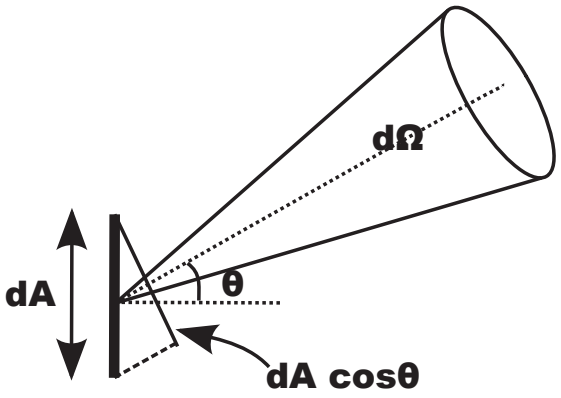

Figure A.1: Power is emitted from the source with the surface area dA into the solid angle $d\Omega$ at an angle θ.

B Silicon optical data

In this appendix, optical data of amorphous and microcrystalline silicon are compared.

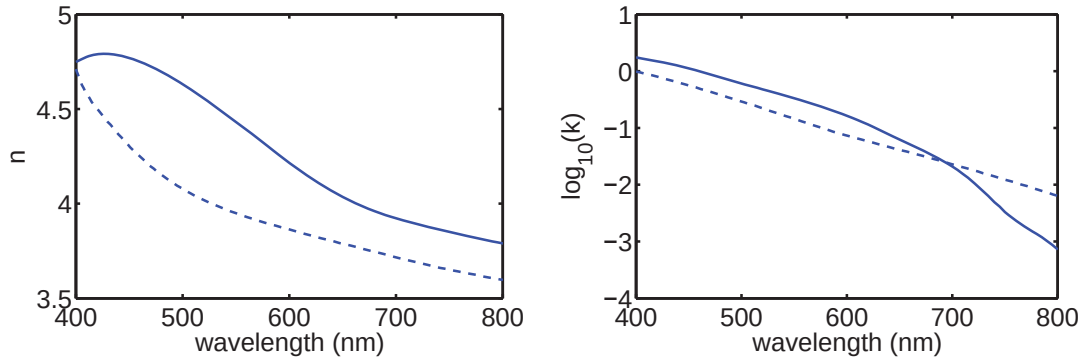

(a) (b)

Figure B.1: Optical data of a-Si:H (solid)and μc-Si (dashed). (a): refractive index, n, (b): extinction coefficient, k.

Bibliography

[1] "Key world energy statistics," tech. rep., International Energy Agency, 2012.

[2] "Energiläget i siffror 2010 /Energy in Sweden facts and figures 2010," tech. rep., The Swedish Energy Agency, 2010.

[3] O. Geden, "Climate change – what next after the 2C boundary?." *The Guardian*, 11 June 2013. Available: http://www.guardian.co.uk/science/political-science/2013/jun/11/science-policy1 [Last accessed: 4 September 2013].

[4] "Climate change 2007: Synthesis report," tech. rep., The Swedish Energy Agency, 2007.

[5] J. Tsao, N. Lewis, and G. Crabtree, "Solar FAQs," 2006. http://www.sandia.gov/~jytsao/.

[6] "Trans-US solar plane finishes flight." *BBC News*, 7 July 2013. Available: http://www.bbc.co.uk/news/science-environment-23195087 [Last accessed: 4 September 2013].

[7] M. A. Green, K. Emery, Y. Hishikawa, W. Warta, and E. D. Dunlop, "Solar cell efficiency tables (version 40)," vol. 20, no. 5, p. 606–614, 2012.

[8] T. Matsui, H. Sai, T. Suezaki, M. Matsumoto, K. Saito, I. Yoshida, and M. Kondo, "Development of highly stable and efficient amorphous silicon based solar cells," in *Presented in EU PVSEC*.

[9] D. E. Carlson and C. R. Wronski, "Amorphous silicon solar cell," *Applied Physics Letters*, vol. 28, no. 11, pp. 671–673, 1976.

[10] D. Staebler and C. Wronski, "Reversible conductivity changes in discharge-produced amorphous Si," *Applied Physics Letters*, vol. 31, p. 292, 1977.

[11] S. Guha, K. Narasimhan, and S. Pietruszko, "On light-induced effect in amorphous hydrogenated silicon," *Journal of Applied Physics*, vol. 52, p. 859, 1981.

[12] J. Hanak and V. Korsun, "Optical stability studies of a-Si:H solar cells," in *16th Photovoltaic Specialists Conference*, vol. 1, pp. 1381–1383, 1982.

[13] H. Keppner, J. Meier, P. Torres, D. Fischer, and A. Shah, "Microcrystalline silicon and micromorph tandem solar cells," *Applied physics A*, vol. 69, no. 2, pp. 169–177, 1999.

[14] G. P. Smestad, *Optoelectronics of solar cells*. Bellingham, Washington: SPIE Press, 2002.

[15] http://rredc.nrel.gov/solar/spectra/am1.5/.

[16] T. Tiedje, E. Yablonovitch, G. D. Cody, and B. G. Brooks, "Limiting efficiency of silicon solar cells," *Electron Devices, IEEE Transactions on*, vol. 31, no. 5, pp. 711–716, 1984.

[17] O. D. Miller, E. Yablonovitch, and S. R. Kurtz, "Strong internal and external luminescence as solar cells approach the shockley–queisser limit," *IEEE Journal of Photovoltaics*, vol. 2, no. 3, pp. 303–311, 2012.

[18] H. A. Haus, *Waves and fields in optoelectronics*, vol. 1. Englewood Cliffs, New Jersey: Prentice-Hall, 1984.

[19] M. Berginski, J. Hupkes, M. Schulte, G. Schope, H. Stiebig, B. Rech, and M. Wuttig, "The effect of front ZnO:Al surface texture and optical transparency on efficient light trapping in silicon thin-film solar cells," *Journal of Applied Physics*, vol. 101, no. 7, pp. 074903–074903, 2007.

[20] Z. Yu, A. Raman, and S. Fan, "Fundamental limit of nanophotonic light trapping in solar cells," *Proceedings of the National Academy of Sciences*, vol. 107, no. 41, pp. 17491–17496, 2010.

[21] Y. A. Akimov and W. Koh, "Resonant and nonresonant plasmonic nanoparticle enhancement for thin-film silicon solar cells," *Nanotechnology*, vol. 21, no. 23, p. 235201, 2010.

[22] Y. A. Akimov and W. S. Koh, "Design of plasmonic nanoparticles for efficient subwavelength light trapping in thin-film solar cells," *Plasmonics*, vol. 6, no. 1, pp. 155–161, 2011.

[23] S. Pillai, K. Catchpole, T. Trupke, and M. Green, "Surface plasmon enhanced silicon solar cells," *Journal of applied physics*, vol. 101, p. 093105, 2007.

[24] K. Aydin, V. E. Ferry, R. M. Briggs, and H. A. Atwater, "Broadband polarization-independent resonant light absorption using ultrathin plasmonic super absorbers," *Nature communications*, vol. 2, p. 517, 2011.

[25] K. Catchpole, A. Polman, *et al.*, "Plasmonic solar cells," *Optics Express*, vol. 16, no. 26, pp. 21793–21800, 2008.

[26] H. Tan, R. Santbergen, A. H. Smets, and M. Zeman, "Plasmonic light trapping in thin-film silicon solar cells with improved self-assembled silver nanoparticles," *Nano letters*, vol. 12, no. 8, pp. 4070–4076, 2012.

[27] Y. A. Akimov, W. Koh, S. Sian, and S. Ren, "Nanoparticle-enhanced thin film solar cells: Metallic or dielectric nanoparticles?," *Applied Physics Letters*, vol. 96, no. 7, pp. 073111–073111, 2010.

[28] P. Matheu, S. Lim, D. Derkacs, C. McPheeters, and E. Yu, "Metal and dielectric nanoparticle scattering for improved optical absorption in photovoltaic devices," *Applied Physics Letters*, vol. 93, no. 11, pp. 113108–113108, 2008.

[29] E. Yablonovitch and G. Cody, "Intensity enhancement in textured optical sheets for solar cells," *IEEE Transactions on Electron Devices*, vol. 29, no. 2, pp. 300–305, 1982.

[30] H. R. Stuart and D. G. Hall, "Thermodynamic limit to light trapping in thin planar structures," *Journal of the Optical Society of America A*, vol. 14, no. 11, pp. 3001–3008, 1997.

[31] H. W. Deckman, C. Wronski, H. Witzke, and E. Yablonovitch, "Optically enhanced amorphous silicon solar cells," *Applied Physics Letters*, vol. 42, no. 11, pp. 968–970, 1983.

[32] W. Shockley and H. J. Queisser, "Detailed balance limit of efficiency of p-n junction solar cells," *Journal of Applied Physics*, vol. 32, no. 3, pp. 510–519, 1961.

[33] A. D. Vos, "Detailed balance limit of the efficiency of tandem solar cells," *Journal of Physics D: Applied Physics*, vol. 13, no. 5, p. 839, 1980.

[34] S. Fahr, T. Kirchartz, C. Rockstuhl, and F. Lederer, "Approaching the lambertian limit in randomly textured thin-film solar cells," *Optics Express*, vol. 19, no. 104, pp. A865–A874, 2011.

[35] S. E. Han and G. Chen, "Toward the lambertian limit of light trapping in thin nanostructured silicon solar cells," *Nano letters*, vol. 10, no. 11, pp. 4692–4696, 2010.

[36] K. Söderström, F.-J. Haug, J. Escarré, O. Cubero, and C. Ballif, "Photocurrent increase in n-i-p thin film silicon solar cells by guided mode excitation via grating coupler," *Applied Physics Letters*, vol. 96, no. 21, pp. 213508–213508, 2010.

[37] V. E. Ferry, J. N. Munday, and H. A. Atwater, "Design considerations for plasmonic photovoltaics," *Advanced Materials*, vol. 22, no. 43, pp. 4794–4808, 2010.

[38] M. Smerlak, "A blackbody is not a blackbox," *European Journal of Physics*, vol. 32, no. 5, p. 1143, 2011.

[39] V. E. Ferry, M. A. Verschuuren, H. B. Li, E. Verhagen, R. J. Walters, R. E. Schropp, H. A. Atwater, and A. Polman, "Light trapping in ultrathin plasmonic solar cells," *Optics Express*, vol. 18, no. S2, pp. A237–A245, 2010.

[40] F. J. Haug, T. Söderström, O. Cubero, V. Terrazzoni-Daudrix, and C. Ballif, "Influence of the ZnO buffer on the guided mode structure in Si/ZnO/Ag multilayers," vol. 106, no. 4, pp. 044502–044502–7, 2009.

[41] H. Haus, W.-P. Huang, S. Kawakami, and N. Whitaker, "Coupled-mode theory of optical waveguides," *Proceedings of the IEEE*, vol. 5, no. 1, pp. 16–23, 1987.

[42] A. Taflove and S. C. Hagness, *Computational Electrodynamics: The Finite Difference Time Domain Method*. Norwood, MA: Artech House, 1995.

[43] O. Isabella, S. Solntsev, D. Caratelli, and M. Zeman, "3-D optical modeling of thin-film silicon solar cells on diffraction gratings," *Progress in Photovoltaics: Research and Applications*, vol. 21, no. 1, pp. 94–108, 2013.

[44] A. Naqavi, K. Söderström, F.-J. Haug, V. Paeder, T. Scharf, H. P. Herzig, and C. Ballif, "Understanding of photocurrent enhancement in real thin film solar cells: towards optimal one-dimensional gratings," *Optics Express*, vol. 19, no. 1, pp. 128–140, 2011.

[45] A. Naqavi, F.-J. Haug, K. Söderström, O. Isabella, H. P. Herzig, C. Ballif, and M. Zeman, "Geometrical impact on guided mode excitation in solar cells," in *Solid-State and Organic Lighting*, Optical Society of America, 2012.

[46] T. Rylander and A. Bondeson, "Application of stable FEM-FDTD hybrid to scattering problems," *IEEE Transactions on Antennas and Propagation*, vol. 50, no. 2, pp. 141–144, 2002.

[47] R. Garg, *Analytical and Computational Methods in Electromagnetics*. Artech House, 2008.

[48] D. Sullivan, J. Liu, and M. Kuzyk, "Three-dimensional optical pulse simulation using the FDTD method," *IEEE Transactions on Microwave Theory and Techniques*, vol. 48, no. 7, pp. 1127–1133, 2000.

[49] M. Zeman, O. Isabella, S. Solntsev, and K. Jäger, "Modelling of thin-film silicon solar cells," *Solar Energy Materials and Solar Cells*, 2013.

[50] M. Sever, B. Lipovšek, J. Krč, A. Čampa, G. Sánchez Plaza, F.-J. Haug, M. Duchamp, W. Soppe, and M. Topič, "Combined model of non-conformal layer growth for accurate optical simulation of thin-film silicon solar cells," *Solar Energy Materials and Solar Cells*, 2013.

[51] L. Li, "Use of fourier series in the analysis of discontinuous periodic structures," *Journal of the Optical Society of America A*, vol. 13, no. 9, pp. 1870–1876, 1996.

[52] R. H. Morf, "Exponentially convergent and numerically efficient solution of maxwell's equations for lamellar gratings," *Journal of the Optical Society of America A*, vol. 12, no. 5, pp. 1043–1056, 1995.

[53] G. Granet, "Reformulation of the lamellar grating problem through the concept of adaptive spatial resolution," *Journal of the Optical Society of America A*, vol. 16, no. 10, pp. 2510–2516, 1999.

[54] R. Dewan, M. Marinkovic, R. Noriega, S. Phadke, A. Salleo, and D. Knipp, "Light trapping in thin-film silicon solar cells with submicron surface texture," *Optics Express*, vol. 17, no. 25, pp. 23058–23065, 2009.

[55] Y. S. Barash and V. L. Ginzburg, "Expressions for the energy density and evolved heat in the electrodynamics of a dispersive and absorptive medium," *Soviet Physics Uspekhi*, vol. 19, no. 3, p. 263, 1976.

[56] K. J. Webb and Shivanand, "Electromagnetic field energy in dispersive materials," *Journal of the Optical Society of America B*, vol. 27, no. 6, pp. 1215–1220, 2010.

[57] J. Chilwell and I. Hodgkinson, "Thin-films field-transfer matrix theory of planar multilayer waveguides and reflection from prism-loaded waveguides," *Jouranl of the Optical Society of America A*, vol. 1, no. 7, pp. 742–753, 1984.

[58] L. Walpita, "Solutions for planar optical waveguide equations by selecting zero elements in a characteristic matrix," *Jouranl of the Optical Society of America A*, vol. 2, no. 4, pp. 595–602, 1985.

[59] A. Ghatak, K. Thyagarajan, and M. Shenoy, "Numerical analysis of planar optical waveguides using matrix approach," *Journal of Lightwave Technology*, vol. 5, no. 5, pp. 660–667, 1987.

[60] K. Ramm, P. Lusse, and H.-G. Unger, "Multigrid eigenvalue solver for mode calculation of planar optical waveguides," *IEEE Photonics Technology Letters*, vol. 9, no. 7, pp. 967–969, 1997.

[61] E. Anemogiannis, E. N. Glytsis, and T. K. Gaylord, "Determination of guided and leaky modes in lossless and lossy planar multilayer optical waveguides: Reflection pole method and wavevector density method," *Journal of Lightwave Technology*, vol. 17, no. 5, p. 929, 1999.

[62] S. Shakir and A. Turner, "Method of poles for multilayer thin-film waveguides," *Applied Physics A*, vol. 29, no. 3, pp. 151–155, 1982.

[63] K. Sakoda, *Optical properties of photonic crystals*, vol. 80. Springer, 2005.

[64] O. Toeplitz, "Zur theorie der quadratischen und bilinearen formen von unendlichvielen veränderlichen," *Mathematische Annalen*, vol. 70, no. 3, pp. 351–376, 1911.

[65] N. Chateau and J.-P. Hugonin, "Algorithm for the rigorous coupled-wave analysis of grating diffraction," *Journal of the Optical Society of America A*, vol. 11, no. 4, pp. 1321–1331, 1994.

[66] L. Li, "Formulation and comparison of two recursive matrix algorithms for modeling layered diffraction gratings," *Journal of the Optical Society of America A*, vol. 13, no. 5, pp. 1024–1035, 1996.

[67] P. Lalanne and G. M. Morris, "Highly improved convergence of the coupled-wave method for TM polarization," *Journal of the Optical Society of America A*, vol. 13, no. 4, pp. 779–784, 1996.

[68] T. Vallius and M. Honkanen, "Reformulation of the Fourier modal method with adaptive spatial resolution: application to multilevel profiles," *Optics Express*, vol. 10, no. 1, pp. 24–34, 2002.

[69] A. Khavasi and K. Mehrany, "Adaptive spatial resolution in fast, efficient, and stable analysis of metallic lamellar gratings at microwave frequencies," *IEEE Transactions on Antennas and Propagation*, vol. 57, no. 4, pp. 1115–1121, 2009.

[70] V. E. Ferry, M. A. Verschuuren, H. B. Li, R. E. Schropp, H. A. Atwater, and A. Polman, "Improved red-response in thin film a-Si:H solar cells with soft-imprinted plasmonic back reflectors," *Applied Physics Letters*, vol. 95, no. 18, pp. 183503–183503, 2009.

[71] S. Solntsev and M. Zeman, "Optical modeling of thin-film silicon solar cells with submicron periodic gratings and nonconformal layers," *Energy Procedia*, vol. 10, pp. 308–312, 2011.

[72] F. Zheng and Z. Chen, "Numerical dispersion analysis of the unconditionally stable 3-d adi-fdtd method," *IEEE Transactions on Microwave Theory and Techniques*, vol. 49, no. 5, pp. 1006–1009, 2001.

[73] A. C. Cangellaris, "Numerical stability and numerical dispersion of a compact 2-d/fdtd method used for the dispersion analysis of waveguides," *IEEE Microwave and Guided Wave Letters*, vol. 3, no. 1, pp. 3–5, 1993.

[74] J. S. Juntunen and T. D. Tsiboukis, "Reduction of numerical dispersion in fdtd method through artificial anisotropy," *IEEE Transactions on Microwave Theory and Techniques*, vol. 48, no. 4, pp. 582–588, 2000.

[75] M. Hammerschmidt, D. Lockau, S. Burger, F. Schmidt, C. Schwanke, S. Kirner, S. Calnan, B. Stannowski, and B. Rech, "3d optical modeling of thin-film a-si/μc-si tandem solar cells with random textured interfaces using fem," in *Optical Instrumentation for Energy and Environmental Applications*, Optical Society of America, 2012.

[76] O. Isabella, S. Solntsev, D. Caratelli, and M. Zeman, "3-d optical modeling of single and multi-junction thin-film silicon solar cells on gratings," in *Material Research Society Proceedings*, vol. 1426, pp. 149–154, Cambridge Univ Press, 2012.

[77] O. Isabella, H. Sai, M. Kondo, and M. Zeman, "Full-wave optoelectrical modeling of optimized flattened light-scattering substrate for high efficiency thin-film silicon solar cells," *Progress in Photovoltaics: Research and Applications*, 2012.

[78] A. Čampa, J. Krč, and M. Topič, "Analysis and optimisation of microcrystalline silicon solar cells with periodic sinusoidal textured interfaces by two-dimensional optical simulations," *Journal of Applied Physics*, vol. 105, p. 083107, 2009.

[79] P. Lalanne and J.-P. Hugonin, "Numerical performance of finite-difference modal methods for the electromagnetic analysis of one-dimensional lamellar gratings," *Journal of the Optical Society of America A*, vol. 17, no. 6, pp. 1033–1042, 2000.

[80] G. Granet, L. B. Andriamanampisoa, K. Raniriharinosy, A. M. Armeanu, and K. Edee, "Modal analysis of lamellar gratings using the moment method with subsectional basis and adaptive spatial resolution," *Journal of the Optical Society of America A*, vol. 27, no. 6, pp. 1303–1310, 2010.

[81] Y.-P. Chiou, W.-L. Yeh, and N.-Y. Shih, "Analysis of highly conducting lamellar gratings with multidomain pseudospectral method," *Journal of Lightwave Technology*, vol. 27, no. 22, pp. 5151–5159, 2009.

[82] A. Naqavi, F.-J. Haug, C. Battaglia, H. P. Herzig, and C. Ballif, "Light trapping in solar cells at the extreme coupling limit," *Jouranl of the Optical Society of America B*, vol. 30, no. 1, pp. 13–20, 2013.

[83] A. Naqavi, F.-J. Haug, K. Söderström, C. Battaglia, V. Paeder, T. Scharf, H. P. Herzig, and C. Ballif, "Angular behavior of the absorption limit in thin film silicon solar cells," *Progress in Photovoltaics: Research and Applications*, 2013.

[84] A. Naqavi, F.-J. Haug, C. Ballif, T. Scharf, and H. Herzig, "Limit of light coupling strength in solar cells," *Applied Physics Letters*, vol. 102, no. 13, p. 131113, 2013.

[85] M. Boccard, C. Battaglia, F.-J. Haug, M. Despeisse, and C. Ballif, "Light trapping in solar cells: Analytical modeling," *Applied Physics Letters*, vol. 101, no. 15, pp. 151105–151105, 2012.

[86] C. Battaglia, M. Boccard, F.-J. Haug, and C. Ballif, "Light trapping in solar cells: When does a Lambertian scatterer scatter Lambertianly?," *Journal of Applied Physics*, vol. 112, p. 094504, 2012.

[87] M. A. Green, "Lambertian light trapping in textured solar cells and light-emitting diodes: analytical solutions," *Progress in Photovoltaics: Research and Applications*, vol. 10, no. 4, pp. 235–241, 2002.

[88] Z. Yu, A. Raman, and S. Fan, "Thermodynamic upper bound on broadband light coupling with photonic structures," *Physical Review Letters*, vol. 109, no. 17, p. 173901, 2012.

[89] L. D. Landau, E. M. Lifšic, J. B. Sykes, J. S. Bell, M. Kearsley, and L. P. Pitaevskii, *Electrodynamics of continuous media*, vol. 364. Oxford: Pergamon press, 1960.

[90] A. Yariv, "Coupled-mode theory for guided-wave optics," vol. 9, no. 9, pp. 919–933, 1973.

[91] A. W. Snyder, "Coupled-mode theory for optical fibers," *Journal of the Optical Society of America Am.*, vol. 62, no. 11, pp. 1267–1277, 1972.

[92] D. Marcuse, *Theory of dielectric optical waveguides*, vol. -1. New York: academic, 1974.

[93] A. Hardy and W. Streifer, "Coupled mode theory of parallel waveguides," *Journal of Lightwave Technology*, vol. 3, no. 5, pp. 1135–1146, 1985.

[94] E. Marcatili, "Improved coupled-mode equations for dielectric guides," *IEEE Journal of Quantum Electronics*, vol. 22, no. 6, pp. 988–993, 1986.

[95] S.-L. Chuang, "A coupled mode formulation by reciprocity and a variational principle," *Journal of Lightwave Technology*, vol. 5, no. 1, pp. 5–15, 1987.

[96] H. Haus and W.-P. Huang, "Coupled-mode theory," vol. 79, no. 10, pp. 1505–1518, 1991.

[97] W.-P. Huang, "Coupled-mode theory for optical waveguides: an overview," *Journal of the Optical Society of America A*, vol. 11, no. 3, pp. 963–983, 1994.

[98] S. G. Johnson, P. Bienstman, M. A. Skorobogatiy, M. Ibanescu, E. Lidorikis, and J. D. Joannopoulos, "Adiabatic theorem and continuous coupled-mode theory for efficient taper transitions in photonic crystals," *Physical Review E*, vol. 66, no. 6, p. 066608, 2002.

[99] L. Verslegers, Z. Yu, Z. Ruan, P. B. Catrysse, and S. Fan, "From electromagnetically induced transparency to superscattering with a single structure: A coupled-mode theory for doubly resonant structures," *Physical Review Letters*, vol. 108, no. 8, p. 083902, 2012.

[100] M. Koshiba, K. Saitoh, K. Takenaga, and S. Matsuo, "Multi-core fiber design and analysis: coupled-mode theory and coupled-power theory," *Optics Express*, vol. 19, no. 26, p. B102, 2011.

[101] A. Kurs, A. Karalis, R. Moffatt, J. D. Joannopoulos, P. Fisher, and M. Soljačić, "Wireless power transfer via strongly coupled magnetic resonances," *Science*, vol. 317, no. 5834, pp. 83–86, 2007.

[102] S. Fan, W. Suh, and J. D. Joannopoulos, "Temporal coupled-mode theory for the Fano resonance in optical resonators," *Journal of the Optical Society of America A*, vol. 20, no. 3, pp. 569–572, 2003.

[103] W. Suh, Z. Wang, and S. Fan, "Temporal coupled-mode theory and the presence of non-orthogonal modes in lossless multimode cavities," *IEEE Journal of Quantum Electronics*, vol. 40, no. 10, pp. 1511–1518, 2004.

[104] C. Manolatou, M. Khan, S. Fan, P. R. Villeneuve, H. Haus, and J. Joannopoulos, "Coupling of modes analysis of resonant channel add-drop filters," *IEEE Journal of Quantum Electronics*, vol. 35, no. 9, pp. 1322–1331, 1999.

[105] Z. Ruan and S. Fan, "Temporal coupled-mode theory for fano resonance in light scattering by a single obstacle†," *The Journal of Physical Chemistry C*, vol. 114, no. 16, pp. 7324–7329, 2010.

[106] M. Yanik, S. Fan, and M. Soljačić, "High-contrast all-optical bistable switching in photonic crystal microcavities," *Applied Physics Letters*, vol. 83, no. 14, pp. 2739–2741, 2003.

[107] T. Tamir and R. Alferness, *Guided-wave optoelectronics*, vol. 354052780. Berlin: Springer-Verlag, 1990.

[108] H. Sai, K. Saito, and M. Kondo, "Investigation of textured back reflectors with periodic honeycomb patterns in thin-film silicon solar cells for improved photovoltaic performance," *IEEE Journal of Photovoltaics*, 2013.

[109] F. J. Haug, K. Söderström, A. Naqavi, and C. Ballif, "Resonances and absorption enhancement in thin film silicon solar cells with periodic interface texture," *Journal of Applied Physic*, vol. 109, no. 8, pp. 084516–084516–8, 2011.

[110] J. Springer, A. Poruba, L. Mullerova, M. Vanecek, O. Kluth, and B. Rech, "Absorption loss at nanorough silver back reflector of thin-film silicon solar cells," *Journal of Applied Physics*, vol. 95, no. 3, pp. 1427–1429, 2004.

[111] J. Krč, F. Smole, and M. Topič, "Potential of light trapping in microcrystalline silicon solar cells with textured substrates," *Progress in Photovoltaics: Research and Applications*, vol. 11, no. 7, pp. 429–436, 2003.

[112] C. Haase and H. Stiebig, "Thin-film silicon solar cells with efficient periodic light trapping texture," *Applied physics letters*, vol. 91, no. 6, pp. 061116–061116, 2007.

[113] C. Battaglia, J. Escarré, K. Söderström, M. Charrière, M. Despeisse, F.-J. Haug, and C. Ballif, "Nanomoulding of transparent zinc oxide electrodes for efficient light trapping in solar cells," *Nature Photonics*, vol. 5, no. 9, pp. 535–538, 2011.

[114] E. Moulin, U. W. Paetzold, J. Kirchhoff, A. Bauer, and R. Carius, "Study of detached back reflector designs for thin-film silicon solar cells," *physica status solidi (RRL)-Rapid Research Letters*, vol. 6, no. 2, pp. 65–67, 2012.

[115] S. Mokkapati and K. Catchpole, "Nanophotonic light trapping in solar cells," *Journal of Applied Physics*, vol. 112, p. 101101, 2012.

[116] T. Lanz, L. Fang, S. Baik, K. Lim, and B. Ruhstaller, "Photocurrent increase in amorphous si solar cells by increased reflectivity of lif/al electrodes," *Solar Energy Materials and Solar Cells*, vol. 107, pp. 259–262, 2012.

[117] V. E. Ferry, L. A. Sweatlock, D. Pacifici, and H. A. Atwater, "Plasmonic nanostructure design for efficient light coupling into solar cells," *Nano letters*, vol. 8, no. 12, pp. 4391–4397, 2008.

[118] O. Isabella, F. Moll, J. Krč, and M. Zeman, "Modulated surface textures using zinc-oxide films for solar cells applications," *physica status solidi (a)*, vol. 207, no. 3, pp. 642–646, 2010.

[119] H. A. Atwater and A. Polman, "Plasmonics for improved photovoltaic devices," *Nature Materials*, vol. 9, no. 3, pp. 205–213, 2010.

[120] J. N. Munday, D. M. Callahan, and H. A. Atwater, "Light trapping beyond the $4n^2$ limit in thin waveguides," *Applied Physics Letters*, vol. 100, no. 12, p. 121121, 2012.

[121] C. Rockstuhl, S. Fahr, and F. Lederer, "Surface plasmon polaritons in metallic nanostructures: Fundamentals and their application to thin-film solar cells," in *Next Generation of Photovoltaics*, pp. 131–155, Springer, 2012.

[122] Y. A. Akimov, W. Koh, S. Y. Sian, and S. Ren, "Nanoparticle-enhanced thin film solar cells: Metallic or dielectric nanoparticles?," *Applied Physics Letters*, vol. 96, no. 7, p. 073111, 2010.

[123] P. Bermel, C. Luo, L. Zeng, L. C. Kimerling, and J. D. Joannopoulos, "Improving thin-film crystalline silicon solar cell efficiencies with photonic crystals," *Optics Express*, vol. 15, no. 25, pp. 16986–17000, 2007.

[124] J. G. Mutitu, S. Shi, C. Chen, T. Creazzo, A. Barnett, C. Honsberg, and D. W. Prather, "Thin film solar cell design based on photonic crystal and diffractive grating structures," *Optics Express*, vol. 16, no. 19, pp. 15238–15248, 2008.

[125] J. Zhao, A. Wang, M. A. Green, and F. Ferrazza, "19.8% efficient "honeycomb" textured multicrystalline and 24.4% monocrystalline silicon solar cells," *Applied Physics Letters*, vol. 73, no. 14, pp. 1991–1993, 1998.

[126] O. Kluth, B. Rech, L. Houben, S. Wieder, G. Schöpe, C. Beneking, H. Wagner, A. Löffl, and H. Schock, "Texture etched ZnO:Al coated glass substrates for silicon based thin film solar cells," *Thin Solid Films*, vol. 351, no. 1–2, pp. 247–253, 1999.

[127] C. Haase and H. Stiebig, "Thin-film silicon solar cells with efficient periodic light trapping texture," *Applied Physics Letters*, vol. 91, no. 6, p. 061116, 2007.

[128] P. Papet, O. Nichiporuk, A. Kaminski, Y. Rozier, J. Kraiem, J.-F. Lelievre, A. Chaumartin, A. Fave, and M. Lemiti, "Pyramidal texturing of silicon solar cell with TMAH chemical anisotropic etching," *Solar Energy Materials and Solar Cells*, vol. 90, no. 15, pp. 2319–2328, 2006.

[129] M. Berginski, J. Hupkes, M. Schulte, G. Schope, H. Stiebig, B. Rech, and M. Wuttig, "The effect of front ZnO:Al surface texture and optical transparency on efficient light trapping in silicon thin-film solar cells," *Journal of Applied Physics*, vol. 101, no. 7, pp. 074903–074903–11, 2007.

[130] H. A. Atwater, "The promise of plasmonics," *Scientific American*, vol. 296, no. 4, pp. 56–62, 2007.

[131] M. A. Green and S. Pillai, "Harnessing plasmonics for solar cells," *Nature Photonics*, vol. 6, no. 3, pp. 130–132, 2012.

[132] Z. Yu, A. Raman, and S. Fan, "Fundamental limit of light trapping in grating structures," *Optics Express*, vol. 18, no. S3, pp. A366–A380, 2010.

[133] C. Heine and R. H. Morf, "Submicrometer gratings for solar energy applications," *Applied Optics*, vol. 34, no. 14, pp. 2476–2482, 1995.

[134] A. Campa, O. Isabella, R. Van Erven, P. Peeters, H. Borg, J. Krc, M. Topic, and M. Zeman, "Optimal design of periodic surface texture for thin-film a-si: H solar cells," *Progress in Photovoltaics: Research and Applications*, vol. 18, no. 3, p. 160, 2010.

[135] S. Koynov, M. S. Brandt, and M. Stutzmann, "Black nonreflecting silicon surfaces for solar cells," *Applied Physics Letters*, vol. 88, no. 20, pp. 203107–203107, 2006.

[136] C. Rockstuhl, S. Fahr, K. Bittkau, T. Beckers, R. Carius, F.-J. Haug, T. Söderström, C. Ballif, and F. Lederer, "Comparison and optimization of randomly textured surfaces in thin-film solar cells," *Optics express*, vol. 18, no. 103, pp. A335–A341, 2010.

[137] F.-J. Haug, K. Söderström, A. Naqavi, J. Li, and C. Ballif, "Super-Lambertian photocurrent-generation in solar cells with periodically textured interfaces," *Accepted in Applied Physics Letters*, 2013.

[138] http://www.ansys.com.

[139] A. Polman and H. A. Atwater, "Photonic design principles for ultrahigh-efficiency photovoltaics," *Nature Materials*, vol. 11, no. 3, pp. 174–177, 2012.

[140] J. E. Harvey and A. Krywonos, "A global view of diffraction: Revisited," in *Robert Shannon and Roland Shack: Legends in Applied Optics* (J. E. Harvey and R. B. Hooker, eds.), Bellingham, Washington: SPIE Press, 2005.

[141] J. E. Harvey, C. L. Vernold, A. Krywonos, and P. L. Thompson, "Diffracted radiance: a fundamental quantity in nonparaxial scalar diffraction theory," *Applied optics*, vol. 38, no. 31, pp. 6469–6481, 1999.

[142] J. E. Harvey, A. Krywonos, and C. L. Vernold, "Modified Beckmann-Kirchhoff scattering model for rough surfaces with large incident and scattering angles," *Optical Engineering*, vol. 46, no. 7, pp. 078002–078002, 2007.

Ali Naqavi

CONTACT INFORMATION

Photonics Doctoral School
École Polytechnique Fédérale de Lausanne
2 A.-L. Breguet
2000 Neuchâtel Switzerland

Tel: +41-327-183-338
E-mail: ali.naqavi@epfl.ch
web: people.epfl.ch/ali.naqavi

RESEARCH INTERESTS

Photovoltaics esp thin film solar cells, silicon photonics, plasmonics, periodic structures, computational electromagnetics, nonlinear optics, quantum optics

EDUCATION

École Polytechnique Fédérale de Lausanne, Lausanne, Switzerland

Ph.D., Photonics, October 2009 to present

- Thesis Topic: *Absorption enhancement in thin-film silicon solar cells*
- Adviser: Prof. Hans Peter Herzig and Dr. Franz Josef Haug
- Area of Study: Photonics and photovoltaics

Sharif University of Technology, Tehran, Iran

M.Sc., Electrical Engineering, December 2008

- Thesis Topic: *Analysis of plasmonic and nanophotonic structures*
- Adviser: Prof. Sina Khorasani and Prof. Khashayar Mehrany
- Area of Study: Optical and microwave communications

B.Sc., Electrical Engineering, September 2006

- Thesis Topic: *Finding and tracking techniques in free space optical communications*
- Adviser: Prof. Amir Ahmad Shishegar
- Area of Study: Electronics

SCIENTIFIC CONTRIBUTIONS

I have contributed to the developement of theoretical foundataions for light absorption enhancement in solar cells. I have established an approach to obtain the limits of light absorption in thin-film solar cells. As an expert in numerical electromagnetics, I have developed several codes for simulation of photonic structures including thin-film solar cells. I am the reviewers of several high impact scientific journals. A list of my publications can be found here: https://sites.google.com/site/photonflow/RS.

SKILLS

- Optical simulation softwares/methods: Rigorous Coupled-Wave Analysis (RCWA), Finite Element Method (HFSS), Finite Difference Time Domain method (Meep), Beam Propagation Method, Multiple Multi-Pole method (OpenMax), CST Microwave Studio, ZEMAX
- Programming: Matlab, C/C++, Python
- Softwares: LabView, Igor, Origin, MS Office, Latex, PovRay
- Analog and digital circuit design: PSpice, Protel, Assembler

LANGUAGE SKILLS Persian (native), English (fluent), French (fluent), Arabic (basic).

List of Publications

Journal Publications

F.-J. Haug, K. Söderström, A. Naqavi, J. Li, and C. Ballif, Super-Lambertian generation of photocurrent in solar cells with periodically textured interfaces, Accepted for publication in Appl. Phy. Lett., 2013.

C. Pahud, O. Isabella, A. Naqavi, F.-J. Haug, M. Zeman, H. P. Herzig, and C. Ballif, Plasmonic silicon solar cells: impact of material quality and geometry, Opt. Express 21, A786-A797, 2013. doi:10.1364/OE.21.00A786

A. Naqavi, F.-J. Haug, C. Ballif, T. Scharf, and H. P. Herzig, Limit of light coupling strength in solar cells, Appl. Phys. Lett. 102, 131113, 2013. doi:10.1063/1.4801311

A. Naqavi, F.-J. Haug, C. Battaglia, H. P. Herzig, and C. Ballif, Angular behavior of the absorption limit in thin film silicon solar cells, Prog. Photovoltaics Res. Appl., 2013. doi:10.1002/pip.2371

A. Naqavi, F.-J. Haug, C. Battaglia, H. P. Herzig, and C. Ballif, Light trapping in solar cells at the extreme coupling limit, J. Opt. Soc. Am. B. 30, 13-20, 2013. doi:10.1364/JOSAB.30.000013

F.-J. Haug, A. Naqavi, and C. Ballif, Diffraction and absorption enhancement from textured back reflectors of thin film solar cells, J. Appl. Phys. 112, 024516, 2012. doi:10.1063/1.4737606

F.-J. Haug, K. Söderström, A. Naqavi, and C. Ballif, Resonances and absorption enhancement in thin film silicon solar cells with periodic interface texture, J. Appl. Phys. 109, 084516, 2011. doi:10.1063/1.3569689

A. Naqavi, K. Söderström, F.-J. Haug, V. Paeder, T. Scharf, H. P. Herzig, and C. Ballif, Understanding of photocurrent enhancement in real thin film solar cells: towards optimal one-dimensional gratings, Opt. Express, vol. 19, no. 1, pp. 128-140, 2011. doi:10.1364/OE.19.000128

Conference Contributions

A. Naqavi, K. Söderström, F.-J. Haug, O. Isabella, H. P. Herzig and C. Ballif, Geomtrical impact on absorption enhancement by guided modes in thin film solar cells, OSA Renewable Energy and the Environment 2012.

A. Naqavi, F.-J. Haug, H. P. Herzig and C. Ballif, Light trapping limit revis- ited: how guided modes enhance light absorption in solar cells, OSA Renewable Energy and the Environment 2012.

A. Naqavi, F.-J. Haug, H. P. Herzig and C. Ballif, Limit of absorption enhance- ment in solar cells with guided modes, EOS annual meeting 2012.

G. D. Osowiecki, A. Cosentino, Q. Tan, A. Naqavi, V. Paeder, M. Roussey, and H. P. Herzig, Excitation of Metallic Nano-Cavities by a Silicon Waveguide for Localized Sensing Applications, EOS annual meeting 2012.

C. Battaglia, M. Boccard, A. Naqavi, C.-M. Hsu, J. Escarré, K. Söderström, M. Charrire, G. Bugnon, D. Alexander, M. Cantoni, F.-J. Haug, M. Despeisse, Y. Cui, and C. Ballif, Pushing light trapping towards the Yablonovitch limit in thin-film silicon solar cells, MRS spring meeting 2012.

F.-J. Haug, K. Söderström, A. Naqavi, C. Battaglia, and C. Ballif, Plasmon and guided-mode resonances in periodically textured thin film silicon solar cells, invited talk, MRS Fall Meeting, Boston 2011.

F.-J. Haug, K. Söderström, A. Naqavi, C. Ballif, Excitation of guided-mode resonances in thin film silicon solar cells, MRS Spring Meeting, San Francisco, 2011.

A. Naqavi, K. Söderström, F.-J. Haug, V. Paeder, T. Scharf, H. P. Herzig and C. Ballif, Enhanced light trapping in realistic thin film solar cells using one-dimensional gratings, Proc. SPIE 8065, 80650A, 2011. doi:10.1117/12.883186

A. Naqavi, V. Paeder, T. Scharf, K. Söderström, F. J. Haug, C. Ballif and H. P. Herzig, An RCWA analysis of solar cell back reflectors: comparison between modelling and experiment, Optical Nanostructures for Photovoltaics, OSA Technical Digest (CD) (Optical Society of America, paper PTuC3, 2010. **(Top 5 Download PV Meeting Paper)**

Workshop presentations

A. Naqavi, F.-J. Haug, K. Söderström, V. Paeder, H. P. Herzig, C. Ballif, Light management in ultrathin photovoltaics, 8th Workshop on Numerical Methods for Optical Nano Structures, ETH Zurich (2012).

A. Naqavi, H. Hainan, V. Paeder, K. Söderström, F.-J. Haug, T. Scharf, H. P. Herzig, C. Ballif, Modeling of thin film silicon solar cells based on one- and two dimensional gratings, International Simulation Workshop (ISW11), Winterthur (2011).

A. Naqavi, V. Paeder, K. Söderström, F.-J. Haug, T. Scharf, H. P. Herzig, C. Ballif, Rigorous Coupled Wave Analysis of thin film solar cells based on gratings, 7th Workshop on Numerical Methods for Optical Nano Structures, ETH Zurich (2011).